

Objective of this thesis is the mapping and structural analysis of the H2 quadrangle, "Victoria", and a reconnaissance study of the geometry and kinematics of lobate scarps on Mercury. To this end, I produced a 1:3,000,000 geologic map of the area using the images provided by the NASA spacecraft MESSENGER, which has been orbiting the planet since March 2011. The structural analysis was supplemented by an innovative method to calculate fault slip data using craters cross-cut by lobate scarps. This method permits to fully constrain remotely-sensed fault kinematics, and it was applied on 16 craters found across 30% of Mercury covered by stereo-DTM data. Inversion of fault slip data gathered within the quadrangle thus allowed the estimation of the orientation of the stress field pertaining to the mapped lobate scarp systems.

Tutor:

Prof. Luigi Ferranti

Co-Tutors:

Prof. Pasquale Palumbo

Università degli Studi di Napoli "Parthenope"

Dipartimento di Scienze e Tecnologie

Dr. Gaetano Di Achille

INAF, Osservatorio Astronomico di Teramo

Coordinator of PhD Theses:

Prof. Maria Boni



STRUCTURAL ANALYSIS OF THE VICTORIA QUADRANGLE (H2)
OF MERCURY BASED ON NASA MESSENGER DATA

V. Galluzzi



PhD
Thesis

Università degli Studi di Napoli "Federico II"
Dipartimento di Scienze della Terra, dell'Ambiente e delle Risorse
Scuola di Dottorato in Scienze della Terra - XXVII Ciclo



STRUCTURAL ANALYSIS OF THE VICTORIA QUADRANGLE (H2) OF MERCURY BASED ON NASA MESSENGER DATA

Valentina Galluzzi





UNIVERSITÀ DEGLI STUDI DI NAPOLI "FEDERICO II"

DIPARTIMENTO DI SCIENZE DELLA TERRA, DELL'AMBIENTE E DELLE RISORSE

SCUOLA DI DOTTORATO IN SCIENZE DELLA TERRA – XXVII CICLO

STRUCTURAL ANALYSIS OF THE VICTORIA QUADRANGLE (H2) OF MERCURY BASED ON NASA MESSENGER DATA

PhD Thesis by

Valentina Galluzzi

Tutor:

Prof. Luigi Ferranti

Co-Tutors:

Prof. Pasquale Palumbo

Dipartimento di Scienze e Tecnologie,
Università degli studi di Napoli "Parthenope"

Coordinator:

Prof Maria Boni

Dr. Gaetano Di Achille

INAF, Osservatorio Astronomico di Teramo

Εἰς Ἑρμῆν

*Ἑρμῆν ὕμνει, Μοῦσα, Διὸς καὶ Μαιάδος νιόν,
Κυλλήνης μεδέοντα καὶ Ἀρκαδίας πολυμήλου,
ἄγγελον ἀθανάτων ἐριούνιον.*

To Hermes

*Muse, sing of Hermes, the son of Zeus and Maia,
lord of Cyllene and Arcadia rich in flocks,
the luck-bringing messenger of the immortals.
[Homeric Hymn]*

Abstract

Objective of this thesis is the mapping and structural analysis of the H2 quadrangle, “Victoria”, and a reconnaissance study of the geometry and kinematics of lobate scarps on Mercury. To this end, I produced a 1:3,000,000 geologic map of the area using the images provided by the NASA spacecraft MESSENGER, which has been orbiting the planet since March, 2011. The geologic map shows the distribution of smooth plains, intermediate plains, intercrater plains units and a classification of crater materials based on an empirical distinction among three stages of degradation. Structural mapping shows that the H2 quadrangle is dominated by N-S faults (here grouped into the Victoria system) to the east and NE-SW faults (Larrocha system) to the west, with the secondary existence of NW-SE-trending faults (Carnegie system) in the north-western area of the quadrangle. A systematic analysis of these systems has led to the following results. 1) The Victoria system is characterized by a main array of faults located along Victoria Rupes – Endeavour Rupes – Antoniadi Dorsum. The segmentation of this array into three different sectors changes from north to south and is spatially linked to the presence of three volcanic vents located at the boundaries between each sector and at the northern end of the Victoria Rupes sector, suggesting that volcanism and faulting are interrelated. 2) The main array of Carnegie system is kinematically linked and antithetical to the Victoria system. Both systems have arguably controlled the growth of a longitudinal, fault-free, crustal and gravimetric bulge in the central area of the Victoria quadrangle, which is interpreted as a regional contractional pop-up. 3) The Larrocha system is interrupted against the central bulge and thus is probably older than the Victoria and Carnegie systems. Buffered crater counting performed on the Victoria system confirms the young relative age of its fault segments with respect to the map units. The faults of the Victoria system post-date the smooth plains, even though the morphological evidence suggests a probable syndepositional fault activity. The structural analysis was supplemented by an innovative method to calculate fault slip data using craters cross-cut by lobate scarps. This method permits to fully constrain remotely-sensed fault kinematics, and it was applied on 16 craters found across 30% of Mercury, covered by stereo-DTM data. Six of the faulted craters are located within the H2 quadrangle and reveal that the

Carnegie system and the Victoria – Endeavour array have near-dip-slip kinematics. The former dips 30° eastward, the latter dips 15°-20° westward. Inversion of fault slip data allows estimation of the orientation of the stress field pertaining to the Victoria-Carnegie-systems, whose σ_1 trends 71° N. At a global scale, the application of the method developed to constrain fault kinematics documented that Mercurian faults have a wider range of dips (7° to 57°) than that predicted by mechanical models. Moreover, this analysis revealed that lobate scarps on Mercury have rakes ranging from 40° to 141° demonstrating the presence of oblique-slip kinematics, differently from what is assumed by the global contraction model that allows only pure or near dip-slip kinematics. Fault slip data were plotted on dip-rake, strike-rake, dip-latitude and strike-latitude diagrams. When more data will be available, these diagrams will help in evaluating the different tectonic models proposed for Mercury and individuating the probable reactivation of ancient tidal despinning structures. However, analysing these diagrams with the available data suggests that neither global contraction nor tidal despinning can satisfactorily explain the oblique-slip kinematics recorded by some faulted craters. Thus the contribution of additional models, such as mantle convection, should be incorporated in a global explanation of Mercurian tectonics.

Table of Contents

Abstract	iii
Table of Contents	v
Preface	vii
1. Introduction	10
1.1. Exploration of Mercury	11
1.2. Physical properties of Mercury	15
1.3. Geology of Mercury	17
1.3.1. Surface cratering and chronostratigraphy	17
1.3.2. Geologic provinces	18
1.3.3. Tectonics	24
1.4. Victoria quadrangle (H2)	28
2. Data	31
2.1. MESSENGER Datasets	32
2.2. Spatial reference	33
2.3. Raster layers	34
2.3.1. Basemaps	34
2.3.2. MDIS single-frames and mosaics	50
2.3.3. Topography	52
3. Methods	56
3.1. H2 geologic mapping	56
3.1.1. GIS workflow	56
3.1.2. Crater material classification	65
3.2. Kinematic analysis	69
3.2.1. Fault parameters	70
3.2.2. Faulted craters as kinematic indicators	72
3.2.3. Measuring fault slip components	74
3.2.4. Estimating slip geometry and fault kinematics	77
3.3. Dating methods	78
3.3.1. Relative age determination	79
3.3.2. Buffered crater counting	80

4. Results	82
4.1. H2 geologic map	82
4.1.1. Surface and linear features	82
4.1.2. Map units	85
4.1.3. Structural framework	90
4.1.4. Relative age of map elements	101
4.2. Kinematic analysis results	106
4.2.1. Mercurian faulted craters	106
4.2.2. H2 faulted craters	111
5. Discussion	118
5.1. Structural analysis of H2 quadrangle	118
5.1.1. Fault system interaction and fault segmentation analysis	119
5.1.2. The Victoria tectonic bulge	123
5.1.3. Timing of fault activity	126
5.2. Structural analysis at semi-global scale	128
5.2.1. Relation between fault geometric and kinematic parameters	128
6. Summary and conclusions	135
6.1. Tectonics of Victoria quadrangle	135
6.2. Fault slip analysis	136
6.3. Open issues and future work	138
Appendix A	139
A.1. ISIS3 processing techniques	139
A.1.1. MDIS single frames and mosaics	139
A.1.2. MDIS BDR mosaics	144
References	147
Acknowledgments	157

Preface

This thesis is focused on the structural geology of Victoria quadrangle H2 (Hermes-2, 22.5°N-65°N; 270°E-360°E) of Mercury, with the aim of building a regional model of its structural framework. Deciphering the geologic setting of this quadrangle offers important insights for understanding the tectonic evolution of the whole planet.

The main questions that motivated this study arose from the varied but consistent trend of the morphostructural features in the eastern and western portion of the quadrangle. Why are Victoria Rupes, Endeavour Rupes and Antoniadi Dorsum aligned in a North-South trend? Why is the West portion of the quadrangle dominated by NE-SW structures? Is there any linkage between these two main structural systems?

Answering these questions and thus improving our knowledge of Mercury will permit better focus on the future targeting choices of the ESA (European Space Agency) BepiColombo mission and in particular of its on-board High Resolution Imaging Channel (HRIC), which is part of the SIMBIOSYS (Spectrometer and Imagers for the MPO BepiColombo Integrated Observatory SYStem) instrument consortium.

The periodical release of images acquired by the NASA (National Aeronautics and Space Administration) MESSENGER (MErcury Surface, Space ENvironment, GEOchemistry and Ranging) spacecraft (Solomon *et al.*, 2007) was fundamental for the realization of the geologic analysis presented here. Further important information came from data acquired in the 70's by the Mariner 10 mission to Mercury (*e.g.* Vilas *et al.*, 1988), which formed the basis for a critical study and review of past work.

During the development of my PhD program a 1:3,000,000 geologic map of the Victoria quadrangle was produced based on NASA MESSENGER images. The map is presented in the attached plate and discussed in Chapters 3.1 and 4.1. It represents the first complete geologic map of this quadrangle, and follows the past 1:5,000,000 partial geologic map of McGill & King (1983).

The structural analysis of quadrangle H-02 has led to the development of an innovative method for calculating planetary fault geometry and kinematics, discussed in Chapters

3.2, 4.2 and 4.3. This method along with partial results from the Victoria quadrangle and spot data from other quadrangles has been published (Galluzzi *et al.*, 2015: “Faulted craters as indicators for thrust motions on Mercury”) in the Geological Society of London Special Publication “Volcanism and Tectonism across the Inner Solar System” (vol. 401), edited by Thomas Platz, Matteo Massironi, Paul K. Byrne and Harald Hiesinger. In the same volume, the same technique is used by Massironi *et al.*, in the work, co-authored by myself, “Lateral ramps and strike-slip kinematics on Mercury”, to assess faults horizontal component of displacement.

As a corollary to the scientific results provided by this research, crater analysis led to the fascinating opportunity of naming one of them – Duccio (*i.e.* /'duɬtʃo/, 58.19°N; - 52.4°W, Fig. A), whose name was officially accepted by IAU (International Astronomical Union) on June 14th, 2013 and became part of the Gazetteer of Planetary Nomenclature soon after (<http://planetarynames.wr.usgs.gov/Feature/15137>). Duccio di Buoninsegna, father of the Sienese painting school of the XIV century, was famous for its paintings on wood panels covered with gold leaves. Duccio was a gothic reformer, but he was also heir of the byzantine tradition, which was characterized by a stylization of the conventional landscape that absolutely does not want to imitate the natural landscape, but rather constitutes a minimal “lunar” landscape. The details of one of Duccio’s paintings (*i.e.* “The Transfiguration”, Fig. A) almost reminded me of familiar features found on Mercury, *lobate scarps*. Duccio crater is indeed cut by one of these features, Carnegie Rupes, and I found interesting dedicating this place to him and our city, Siena, who made me an “adorer of the good science of rock-breaking” (cit. Charles Darwin in a letter to Charles Lyell).

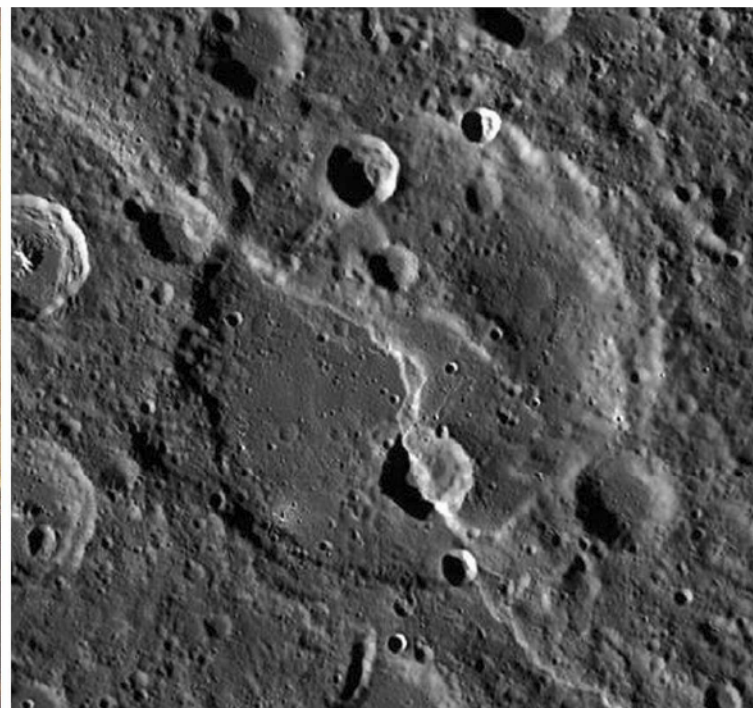


Figure A. Left: "The Transfiguration" painted by Duccio di Buoninsegna, once part of the back side of the altarpiece "Maestà" in the cathedral of Siena, now held by the National Gallery, London. Right: Duccio crater, 58.19°N – -52.4°W, cross-cut by the lobate scarp Carnegie Rupes.

1. Introduction

To better frame the geology of Victoria quadrangle in the evolution of Mercury, I present here an overview of the planet, what we know about it now and what was done in the past. Mercury was already known by ancient civilizations that observed and studied the planet motion with the naked eye. The first systematic campaign of Mercury's observations was made by Giovanni Virginio Schiaparelli (1835-1910), who drew the very first map of the planet surface features. Following the Italian astronomer, other scientists drew maps of Mercury (*e.g.* Fig. 1.1), until a *giant leap* in knowledge was made during the hub of the so called "golden age of space exploration".

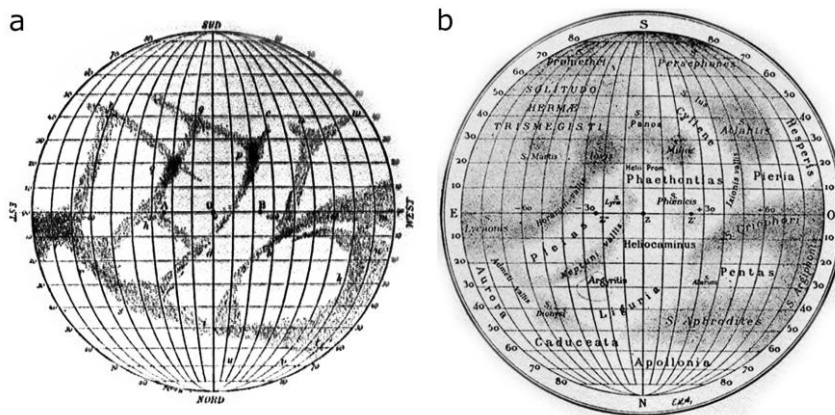


Figure 1.1. Examples of planispheres drawn from telescopic observations of Mercury. a) Drawing by Giovanni Virginio Schiaparelli (1882-1889, Brera, Milano); b) Drawing by Eugène Michel Antoniadi (1934).

"Many clues to the physical nature of Mercury await only systematic visual and photographic observing programs by well-equipped and favourably located observers on Earth. But final answers to these intriguing questions may not come until a space vehicle flies by that planet."

Cruikshank & Chapman, 1967

1.1. Exploration of Mercury

The exploration of Mercury began in 1974, when NASA Mariner 10 (M10) spacecraft (Fig. 1.2) performed the first planet flyby on March 24th after a gravity assist from Venus on February 5th, 1974. This event was then followed by two other flybys on September 21st, 1974 and March 16th, 1975. Thanks to the first two flybys, over 2000 useful pictures were produced and 45% of Mercury's surface was photographed by the M10 Television Experiment (Murray *et al.*, 1975) at a resolution better than 2 km, up to 100 m (Murray *et al.*, 1975; Danielson *et al.*, 1975; Davies *et al.*, 1978; Vilas *et al.*, 1988). M10 third encounter also provided some high resolution pictures (~100 m), although they were received only as quarter frames because of ground communication problems (Davies *et al.*, 1978).

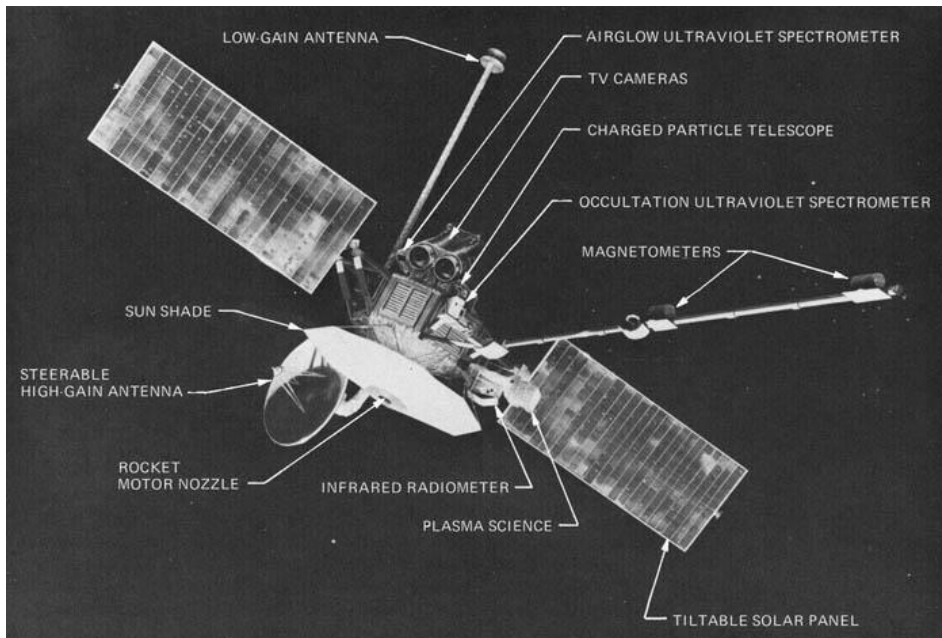


Figure 1.2. Labelled diagram of Mariner 10 spacecraft, launched by NASA on November 3rd, 1973 (courtesy of NASA).

"[...] Mariner 10 has placed Mercury in a photographic status similar to that of the Moon in the early 1960's, before space exploration began, [...]"

Murray *et al.*, 1975

The acquired frames were mosaicked together to produce a 40% view of the planet, thus showing the 75% of the sunlit portion of Mercury during M10 flybys (Fig. 1.3).

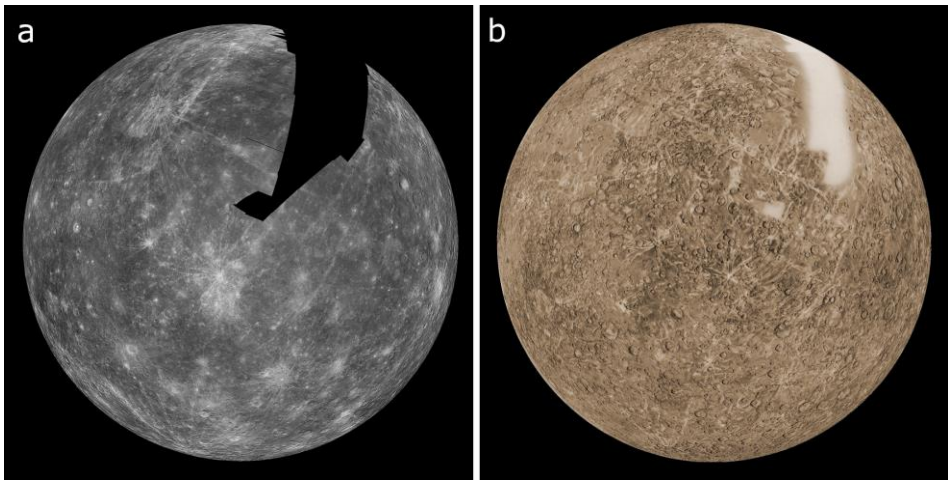


Figure 1.3. Orthographic projection of Mercury centered at lat. 0°N and lon. 100°W: a) photomosaic of Mariner 10 images (courtesy of NASA); b) shaded relief map drawn by the USGS cartographer Patricia M. Bridges (courtesy of NASA/USGS).

Thirty years later NASA planned a new mission to Mercury – MESSENGER, launched on April 4th, 2004 (Fig 1.4). After three flybys (January 14th, 2008; October 6th, 2008; September 29th, 2009) MESSENGER entered its orbit about Mercury on March 18th, 2011, thus being the first spacecraft to orbit this planet. MESSENGER datasets improved existing data and provided important information to study the previously unframed dark side of Mercury.

The on-board Mercury Dual Imaging System (MDIS) is composed of a Wide Angle Camera (WAC) that can observe Mercury through 11 different filters and monochrome across the wavelength range 395 to 1,040 nanometres (visible through near-infrared light) with a 10.5° wide view, and a Narrow Angle Camera (NAC) that can take monochrome images at high resolution thanks to a 1.5° wide view. The Mercury Laser Altimeter (MLA) can derive surface heights thanks to an infrared laser transmitter and a receiver. Besides the useful information on topography, MLA experiment can also study Mercury's gravitational field and internal structure when combined with ground radar observations. At the time of this writing, MESSENGER has provided more than

255,000 images, a global coverage of the whole planet and topography of the northern hemisphere, which constituted the base data of the present thesis (see Chapter 2).



Figure 1.4. Artist's impression of MESSENGER spacecraft at Mercury, launched by NASA on April 4th, 2004 (courtesy of NASA/JHUAPL/CIW).

Further information on the planet's characteristics and geology will be provided by next mission to Mercury, BepiColombo (Benkhoff *et al.*, 2010; Fig. 1.5), planned by ESA in cooperation with JAXA (Japan Aerospace eXploration Agency) that will be launched on mid-July, 2016. BepiColombo is Europe's first mission to Mercury and it will start orbiting the planet in 2024. It comprises two spacecraft: the ESA Mercury Planetary Orbiter (MPO) and the JAXA Mercury Magnetospheric Orbiter (MMO). Among its 11 instruments, BepiColombo MPO will host the SIMBIOSYS instrument suite, an Italian project that consists of a High Resolution Imaging Channel (HRIC), a STereo imaging Channel (STC) and a Visual and Infrared Hyperspectral Imager (VIHI) channel (Fig. 1.6). The planning content of BepiColombo imaging instruments will strongly depend on choices based on the updated science knowledge of Mercury's surface, and this occurrence motivated the present research project.

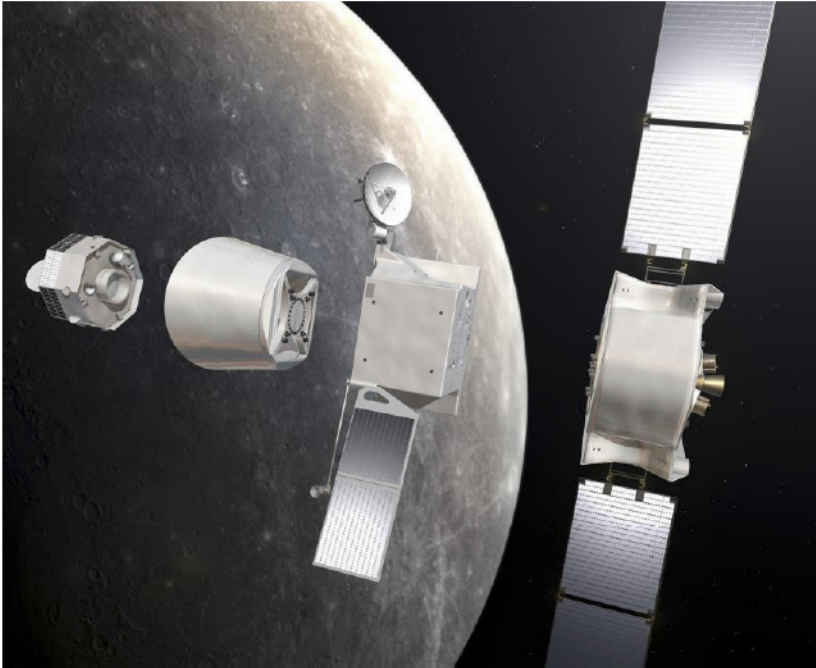


Figure 1.5. Artist's impression of BepiColombo spacecraft cruise modules. From left to right: Mercury Magnetospheric Orbiter, Sun Shield, Mercury Planetary Orbiter, Transfer Module (courtesy of ESA/AOES Medialab).

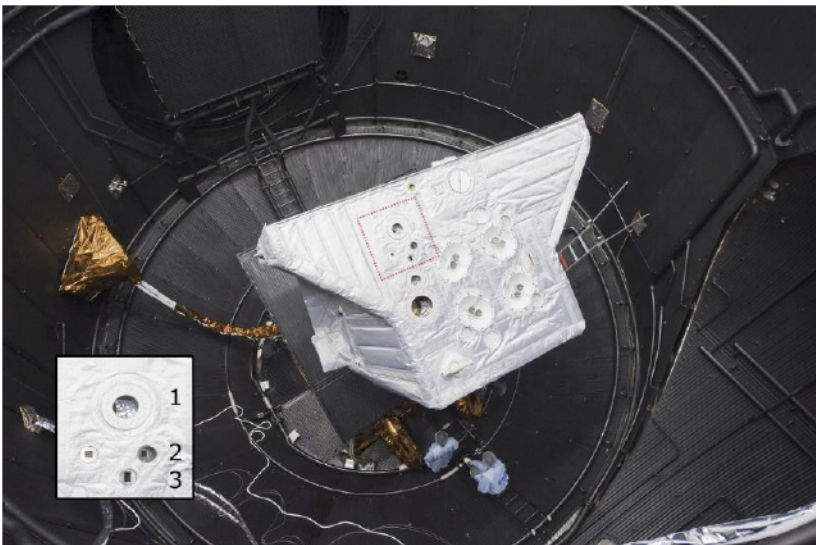


Figure 1.6. BepiColombo MPO Structural and Thermal Model (STM) inside the Large Space Simulator (LSS) at ESTEC Test Centre (courtesy of ESA). The red square indicates the location of SIMBIOSYS suite, also shown in the inset: 1) HRIC; 2) STC (both central holes); 3) VIHI.

1.2. Physical properties of Mercury

All the information gathered with the past and present missions to Mercury confirm that this planet is an end-member case in our Solar System. Mercury is the innermost planet, the smallest, the fastest to complete its orbit about the Sun, it has a highly elliptic orbit the highest surface temperature range. Despite its small size (*i.e.* diameter is 4880 km), Mercury's density is one of its most striking peculiarities. It is slightly smaller than that of the Earth (5.43 g/cm^3 against 5.52 g/cm^3 , respectively), but it is larger if we consider the uncompressed density (*i.e.* density without the gravitational compression factor), which is 5.30 g/cm^3 against 4.40 g/cm^3 of the Earth. The high bulk density of Mercury is caused by the presence of a large iron core in its interior (*e.g.* Siegfried & Solomon, 1974). M10 mission also discovered that Mercury has a weak magnetic field (roughly 1% that of the Earth, Ness *et al.*, 1974). The differentiated internal structure of Mercury thus became a puzzling topic. Even though the presence of a magnetic field is not necessarily attributable to a dynamo mechanism in a molten core (Stephenson, 1976; Aharonson *et al.*, 2004), recent studies on the planet's longitude libration have confirmed that Mercury's core is indeed partially liquid (Margot *et al.*, 2007). Figure 1.7 shows that the interior structure of Mercury might be even more differentiated than that of the Earth. Stated that Mercury has a $\sim 2440 \text{ km}$ radius, Smith *et al.* (2012) divide it into a $\sim 410 \text{ km}$ solid outer shell (with a crustal thickness of 20 to 80 km) and a 2030 km radius molten iron core upper limit, while the radius of the central solidified part of the core is unknown. The authors also suggest the presence of a solid FeS layer at the base of the mantle that “*could be a few tens of kilometres to as much as $\sim 200 \text{ km}$ in thickness*”, which would justify the high density of the solid outer shell ($\sim 3.65 \text{ g/cm}^3$), given that Mercury's surface (and probably also the mantle, Smith *et al.*, 2012) has a very low iron abundance ($\sim 4 \text{ w\%}$, Nittler *et al.*, 2011).

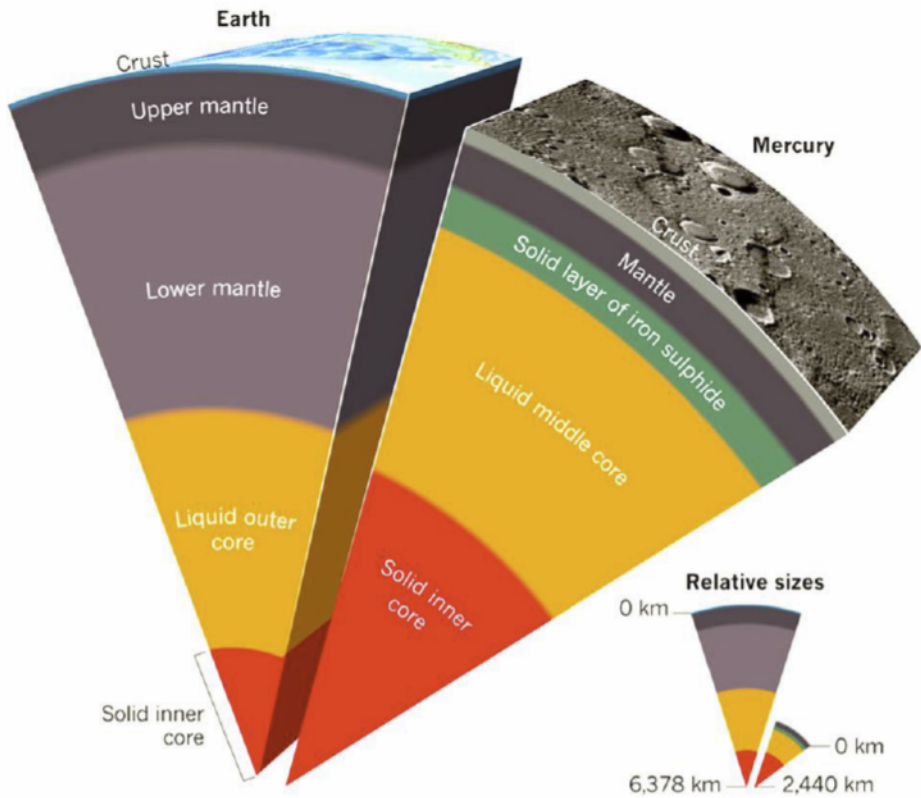


Figure 1.7. Mercury's interior structure compared to that of the Earth (from Stevenson *et al.*, 2012).

1.3. Geology of Mercury

"Paradoxically, Mercury has a Moon-like exterior and an Earth-like interior."

Davies *et al.*, 1978

1.3.1. Surface cratering and chronostratigraphy

Mercury's surface resembles that of the Moon: densely cratered terrains and no signs of eolian, fluvial or glacial resurfacing processes. These characteristics, which recall two essentially primitive bodies with unchanged records of their early formation, are mainly due to the almost total absence of an atmosphere (Mercury has a weak exosphere), which is usually the principal cause of the surface modification (due to erosion and material transport) of planets. Although the cratered terrains on Mercury might seem similar to those of the Moon, it soon seemed apparent that they are not so densely cratered as those of the Moon (*e.g.* Spudis & Guest, 1988). Fassett *et al.* (2011), state that crater density on Mercury is similar to that of the Moon only for craters in the range of 128 km to 512 km, but the density of craters between 20 and 128 km is much lower on Mercury than on the Moon (1:2 ratio in their most densely cratered regions).

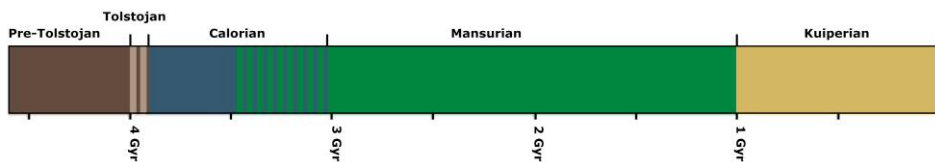


Figure 1.8. Mercury's chronology (modified from van Gasselt & Neukum, 2011).

Mercury's resemblance with the Moon led to the development of a chronostratigraphic classification similar to that of the Earth's satellite (Shoemaker & Hackman, 1962). The chronostratigraphy of Mercury is in fact based on impact events that determine the bases of each Mercurian system (McCauley *et al.*, 1981; Spudis, 1985; Spudis & Guest, 1988). Unlike the Earth's chronostratigraphy, where the term "system" spans periods of tens of millions of years, Mercurian systems have variable period lengths, ranging from a hundred millions of years to billions of years. In some cases they are more properly similar to Earth eonothems, but considering their variability, "system" and "period" are widely accepted as a general terminology to address Mercurian chronostratigraphy and

geochronology, respectively (e.g. Spudis & Guest, 1988; Neukum *et al.*, 2001a). The geochronology of Mercury was established based on a comparison with Lunar chronology and is therefore divided in five periods (Fig. 1.8, Spudis & Guest, 1988; see also Neukum *et al.*, 2001a). The *Pre-Tolstojan period* encompasses units older than 3.97 Ga (Neukum *et al.*, 2001a) or 4.06 Ga (Strom & Neukum, 1988).

The *Tolstojan period* follows the Pre-Tolstojan and its base is defined by the Tolstoj basin deposits. Tolstojan period ends at 3.77 Ga (Neukum *et al.* 2001a) or 3.85 Ga (Strom & Neukum, 1988), which is the base of the following *Calorian period*, defined by the Caloris basin deposits (the youngest on Mercury). The *Mansurian period* base is defined by Mansur crater deposits, whose estimated age is 3-3.5 Ga (Spudis & Guest, 1988; Strom & Neukum, 1988; Neukum *et al.* 2001a). Finally the *Kuiperian period* is the most recent period on Mercury and its base is established at ~1 Ga, which is the age of the young Kuiper crater materials (Spudis & Guest, 1988; Strom & Neukum, 1988; Neukum *et al.* 2001a).

1.3.2. Geologic provinces

When dealing with the geology of a planet like Mercury, it is preferable to speak about *photogeology*. The classical geologic concept of *lithostratigraphic unit* is not applicable on remote sensed images. The lack of real samples and rock absolute ages is the main issue that led planetary geologists to introduce the concept of *terrain units* on Mercury (Trask & Guest, 1975; Spudis & Guest, 1988). In their first geologic map of Mercury (Fig. 1.9) derived mainly from M10 first encounter, Trask & Guest (1975) assess that “[...] on Mercury, surface morphology reflects the age, composition, lithology, and mode of formation of the underlying rock unit”. Terrain units of Mercury were then revisited during a geologic mapping campaign of Mercury at 1:5.000.000 based on M10 images (Schaber & McCauley, 1980; De Hon *et al.*, 1981; Guest & Greeley, 1983; McGill & King, 1983; Grolier & Boyce, 1984; Spudis & Prosser, 1984; Trask & Dzuring, 1984; King & Scott, 1990; Strom *et al.*, 1990) and termed *geologic provinces* by Spudis & Guest (1988), who adopted this term after McCauley & Wilhelms (1971).

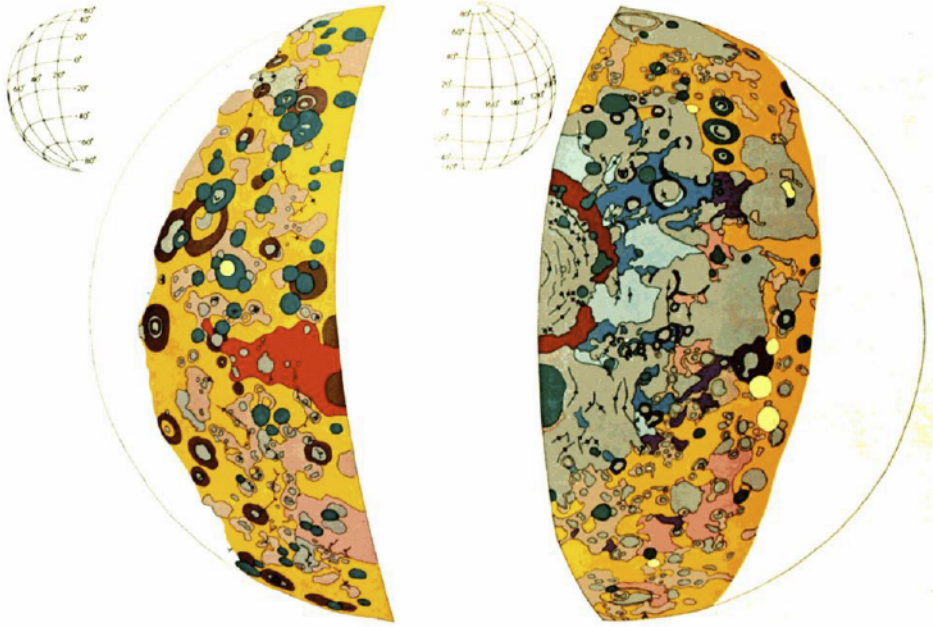


Figure 1.9. Mercury's preliminary geologic map drawn by Trask & Guest (1975) on Mariner 10 first encounter images.

Intercrater plains

Trask & Guest (1975) defined the intercrater plains (ICP) as the *level to gently rolling ground between and around large craters and basins*. This kind of terrain is the most widespread unit on Mercury. Whitten *et al.* (2014), accurately reclassified intercrater plains on the basis of MESSENGER data, stating that intercrater plains show a level topography at a local scale, whereas at a regional scale show an undulating surface. Globally, the heights of intercrater plains may vary by ~ 5 km and are characterised by a high density of craters < 10 km (Whitten *et al.*, 2014). Intercrater plains are thought to be the remnants of volcanic flows by most authors (Murray *et al.*, 1974, 1975; Strom, 1977; Kiefer & Murray, 1987; Trask & Guest, 1975; Spudis & Guest, 1988; Whitten *et al.*, 2014). However some authors put forth the notion that intercrater plains were emplaced as fluidized ejecta from large crater impacts (Wilhelms, 1976; Oberbeck *et al.*, 1977). Intercrater plains (Fig. 1.10) show a high variety of textures, they are composed mostly of low reflectance materials (LRM) and there are no clear textural changes when they merge with high-reflectance red plains (HRP) (Whitten *et al.*, 2014).

However some authors prefer to address the high albedo regions of intercrater plains as “bright intercrater plains” (BIP), which seem to occur at higher topographic elevation with a more intense cratering record (Mancinelli *et al.*, 2015). The emplacement of ICP predates the period of the Late Heavy Bombardment (LHB) (*e.g.* Trask & Guest, 1975) of the Inner Solar System, thus these materials are Tolstojan to pre-Tolstojan (Whitten *et al.*, 2014) and represent the oldest surface on Mercury.

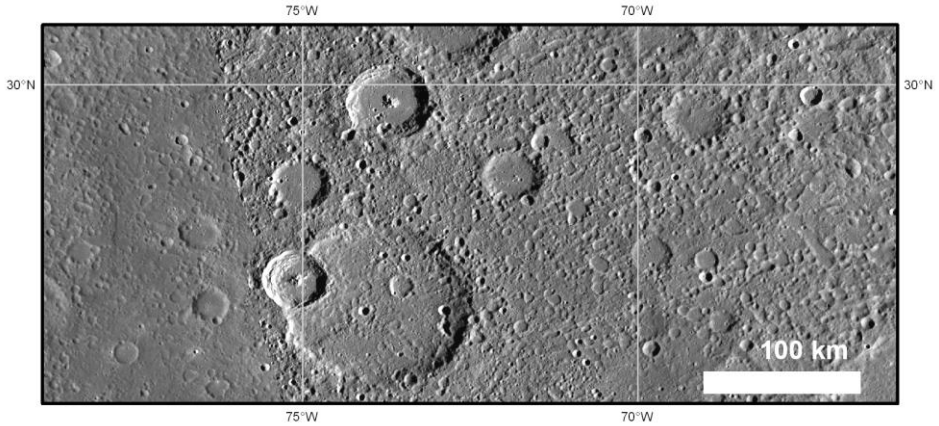


Figure 1.10. MESSENGER MDIS basemap image (250 mpp) of intercrater plains on Mercury. Equirectangular projection.

Intermediate plains

Intermediate plains (IP) were introduced during the M10 mapping campaign (Schaber & McCauley, 1980; Guest & Greeley, 1983; McGill & King, 1983; Grolier & Boyce, 1984; Spudis & Prosser, 1984; Trask & Dzurisin, 1984; King & Scott, 1990; Strom *et al.*, 1990) and lately reconsidered after the analysis of MESSENGER data (Denevi *et al.*, 2013; Whitten *et al.*, 2014). Most of the M10 cartographers noticed that these terrains form “planar to undulating surfaces that have higher crater density than smooth plains material, but are less heavily cratered than intercrater plains material” (Spudis & Prosser, 1984, Fig. 1.11). However recent works conclude that there is no clear contrast between intermediate plains, which seem to have a “patchy” distribution, and the adjacent terrains (Denevi *et al.*, 2013; Whitten *et al.*, 2014). For this reason, some patches of intermediate plains were reclassified either as intercrater plains (Whitten *et al.*, 2014) or as smooth plains materials (Denevi *et al.*, 2013). Intercrater-like patches

also show similar ages to ICP of Tolstojan and Pre-Tolstojan period (Whitten *et al.*, 2014).

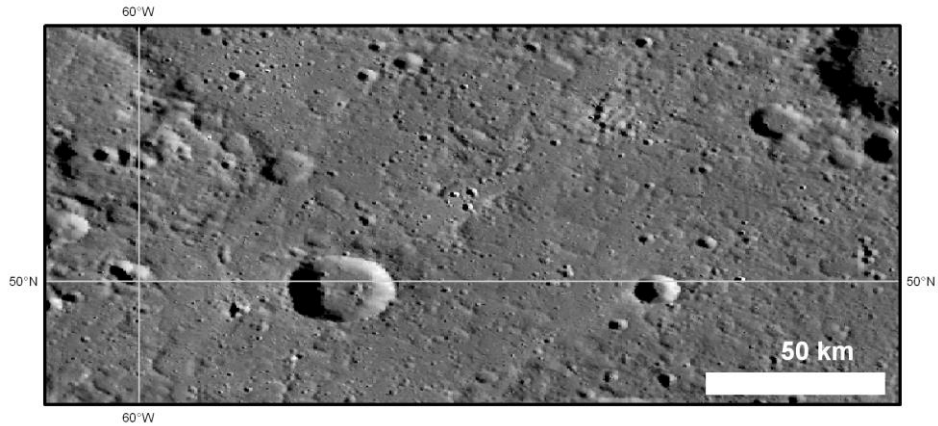


Figure 1.11. MESSENGER MDIS basemap image (250 mpp) of intermediate plains on Mercury. Equirectangular projection.

Smooth plains

Smooth plains (SP) were defined for their morphological characteristics as “relatively flat, sparsely cratered material” (Trask & Guest, 1975; Strom *et al.*, 1975; Spudis & Guest, 1988) “that displays sharp boundaries with adjacent regions and is level to gently sloped over a baseline of ~100-200 km” (Denevi *et al.*, 2013, Fig. 1.12). In early studies SP morphologies were interpreted as being originated from 1) effusive volcanism (Murray *et al.* 1974; Strom *et al.*, 1975; Trask & Guest, 1975; Trask & Strom, 1976; Spudis & Guest, 1988) or 2) fluidized impact ejecta (Wilhelms, 1976). Recent studies seem to confirm their volcanic nature due to evidences of flow and neat colour contrasts with the nearby materials (Denevi *et al.*, 2013). Smooth plains cover 27% of Mercury’s surface (Denevi *et al.*, 2013) and they are supposed to belong to the period soon after the LHB (Strom *et al.*, 1975, 2008; Trask & Guest, 1975; Spudis & Guest, 1988; Head *et al.*, 2011; Denevi *et al.*, 2013). Several authors estimated an age of 3.7 – 3.9 Ga based on crater density distribution (Strom *et al.*, 2008, 2011; Fassett *et al.*, 2009; Head *et al.*, 2011; Ostrach *et al.*, 2011; Denevi *et al.*, 2013), implying that the SP belong to the Calorian period.

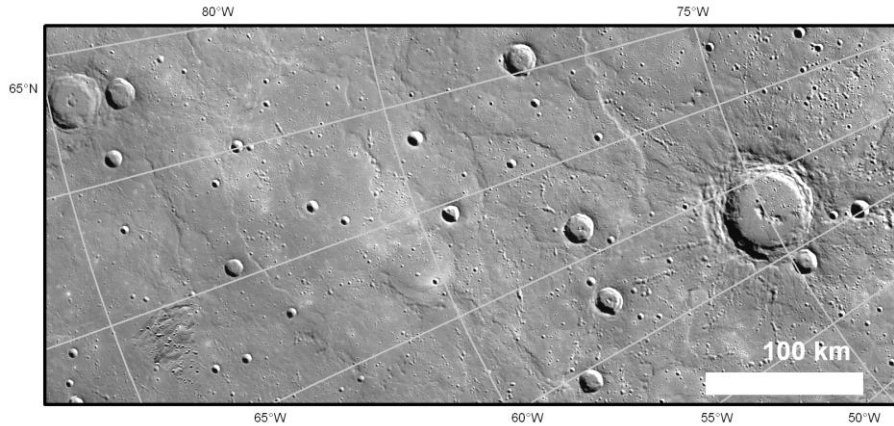


Figure 1.12. MESSENGER MDIS basemap image (250 mpp) of smooth plains on Mercury. Stereographic north pole projection.

Following the Calorian period, apart from impact cratering and explosive volcanism (see Thomas *et al.*, 2014), no major depositional event occurred (*e.g.* extensive volcanic flows), thus smooth plains represent the youngest geologic province on Mercury.

Crater materials

Since craters are progressively degraded by the superposition of newer impacts, many authors tried to use morphological evidence to classify crater degradation and assess their relative ages (*e.g.* Arthur *et al.*, 1963; Pohn & Offield, 1970; Cintala *et al.*, 1976; Wood *et al.*, 1977; Wood & Anderson, 1978; Wood, 1979; McCauley *et al.*, 1981; Leake *et al.*, 1982; Spudis & Guest, 1988). Two main classification systems were developed to classify craters: 1) the Lunar and Planetary Laboratory (LPL) system (*e.g.* Arthur *et al.*, 1963); 2) the United States Geological Survey (USGS) system (*e.g.* McCauley *et al.*, 1981).

The LPL system distinguishes five crater classes (LPL-C₁-C₅) being LPL-C₁ the freshest and LPL-C₅ the most degraded. The distinction among the several LPL crater classes is based mainly on rim sharpness and was developed on Lunar craters (Arthur *et al.*, 1963). Later on, Wood *et al.* (1977) used the LPL system to classify Mercurian craters.

The USGS system uses five classes as the LPL system does, but with inverse numbering (USGS-C₁/-C₅). USGS-C₁ craters are the oldest and most degraded craters, while USGS-C₅ craters are the least degraded craters: the ascending class order from subdued to crisp craters was chosen to reflect a normal stratigraphic order. The USGS system focuses more on crater features and internal structures such as central peaks and floor features, rather than crater rim sharpness. It was developed on Mercurian craters by Newell Trask (see McCauley *et al.*, 1981) on the basis of the Lunar craters morphologic age introduced by Pohn & Offield (1970).

When the first 1:5.000.000 geologic maps of Mercury based on M10 data were published by the USGS, some issues arose from the photo-interpretation of degraded Mercurian craters. Some of the mapped craters presented morphological evidence that seemed inconsistent with their relative stratigraphic order; this topic will be further analysed in chapter 3.1.2.

1.3.3. Tectonics

The Moon shares several surface characteristics with Mercury, but this is not the case of faults. Unlike the Moon, the innermost planet is covered with widespread tectonic landforms, which are dominantly contractional structures (Strom *et al.*, 1975). Extension on Mercury is recorded only inside the largest basins (*e.g.* Caloris basin, Fig. 1.13), with narrow grabens striking radially or concentrically from the basin centre (Strom *et al.*, 1975; Dzurisin, 1978; Murchie *et al.*, 2008; Watters *et al.*, 2009). Caloris grabens crosscut contractional features (*i.e.* wrinkle ridges), and are interpreted as the youngest, but spatially limited, structures on the planet (Strom *et al.*, 1975; Dzurisin, 1978; Murchie *et al.*, 2008; Watters *et al.*, 2009).

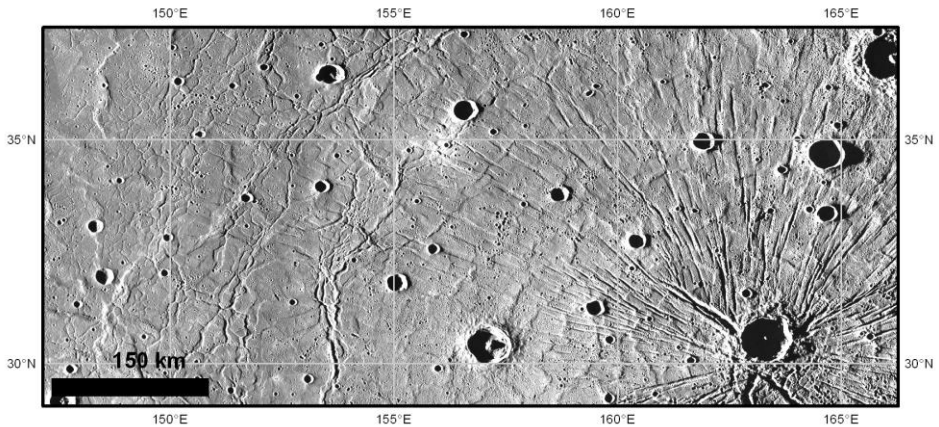


Figure 1.13. MESSENGER MDIS basemap image (250 mpp) of radial and concentric graben structures inside Caloris basin. Equirectangular projection.

On the other hand, contractional faults are widespread (Strom *et al.*, 1975). The latest global structural mapping by Byrne *et al.* (2014) revealed almost 6000 contractional structures on Mercury (Fig. 1.14).

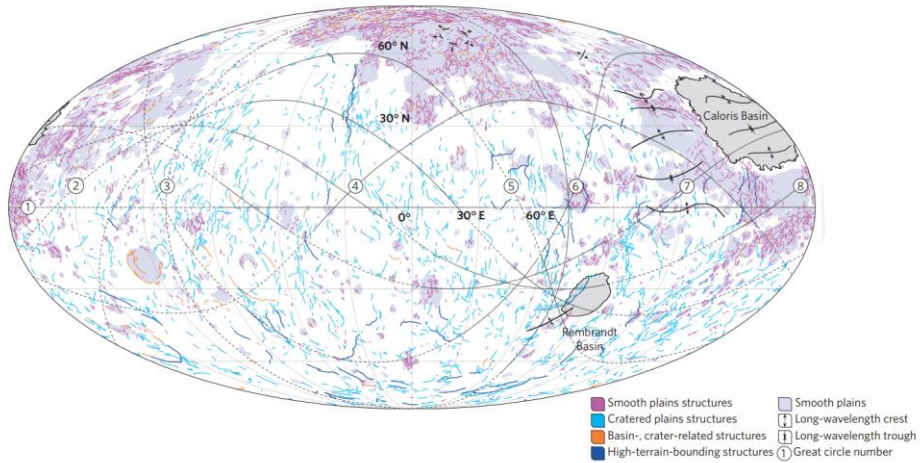


Figure 1.14. Mercury's global structural mapping of contractional structures in Mollweide projection by Byrne *et al.*, 2014. The mapped smooth plains are from Denevi *et al.* (2013).

These structures are usually divided into three main families: 1) wrinkle ridges; 2) lobate scarps; 3) high-relief ridges (*e.g.* Fig. 1.15). Wrinkle ridges are often found on smooth plains and are also found on the Moon (*e.g.* Plescia & Golombek, 1986). They are “typically broad, low-relief arches often superposed by a narrow ridge” (Byrne *et al.*, 2014, Fig. 1.15a). The strict relationship between wrinkle ridges and extensive lava flows may lead to think that they have a common origin, nevertheless they are thought to be the expression of fault-propagation folding or fault bend folding (Plescia & Golombek, 1986). Lobate scarps are steep scarps characterized by “a gently sloping back limb” (Byrne *et al.*, 2014, Fig. 1.15b) and are asymmetrical in cross-section (see Watters & Nimmo, 2010). They were described for the first time by Strom *et al.* (1975) and interpreted as surface breaking thrusts. Considering the large size of these structures, they surely accommodated more shortening than wrinkle ridges (Byrne *et al.*, 2014). These scarps (called *rupes/rupēs* in IAU nomenclature) often cut large craters and also Calorian units, therefore their activity continued after the emplacement of these young terrains (*e.g.* Watters *et al.*, 2004). The third category of contractional structures, the high-relief ridges (Fig. 1.15c), was described for the first time by Dzurisin (1978). These ridges (called *dorsum/dorsa* in IAU nomenclature) are symmetrical in cross-section and are less common on Mercury. They often intermingle with lobate scarps and probably share a similar origin and age with them (Watters & Nimmo, 2010).

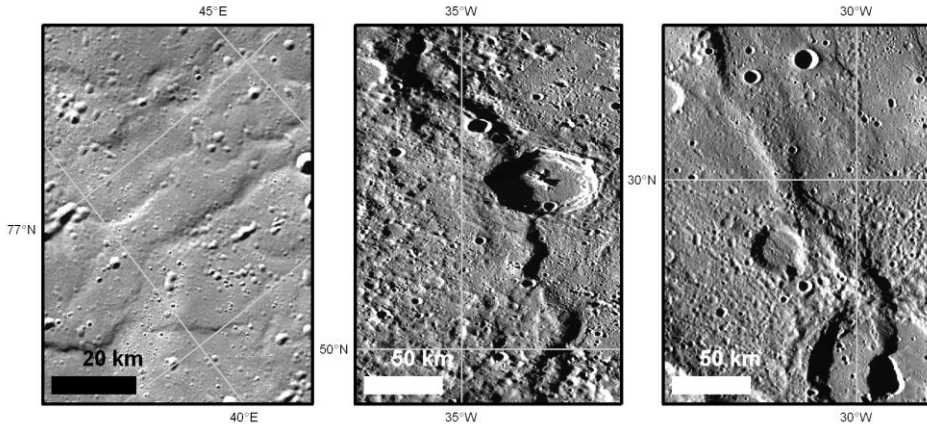


Figure 1.15. Examples of the three main contractional structures on Mercury: a) wrinkle ridges on the northern smooth plains (stereographic north pole projection); b) Victoria Rupes, a lobate scarp (equirectangular projection); c) Antoniadi Dorsum, a high relief ridge (equirectangular projection). All the images are taken from the 250 mpp MESSENGER MDIS basemap.

Three main tectonic models have been proposed to explain the tectonic evolution of Mercury (Fig. 1.16): 1) global contraction (*e.g.* Strom *et al.*, 1975); 2) tidal despinning (*e.g.* Melosh & Dzurisin, 1978); 3) mantle convection (King, 2008). Global contraction (Strom *et al.*, 1975, Fig. 1.16a) is thought to be generated by secular cooling of the planet's interior (Solomon, 1976; Hauck *et al.*, 2004); by calculating the displacement–length ratio (Cowie & Scholz, 1992) of thrusts it was possible to estimate the radial shortening of Mercury (*e.g.* Watters & Nimmo, 2010; Byrne *et al.*, 2014). The latest estimates of radial shortening show that Mercury contracted by ~ 7 km (Byrne *et al.*, 2014). MESSENGER mission confirmed the predominant contractional character of Mercury's tectonics (Watters *et al.*, 2009; Watters & Nimmo, 2010), thus global contraction is the most reliable theory proposed so far. Tidal despinning theory (Fig. 1.16b) does not exclude global contraction forces (Melosh & Dzurisin, 1978; Pechmann & Melosh, 1979; Matsuyama & Nimmo, 2009), however it strongly relies on the gravitational forces exerted by the sun on the small planet. Melosh (1977) argued that on a despun planet we should find north–south oriented thrusts at low latitudes, NW–SE and NE–SW strike-slip faults at mid-latitudes and E–W normal faults at high latitudes. The tidal despinning model was refined for Mercury by Pechmann & Melosh (1979) and subsequently by Matsuyama & Nimmo (2009), who proposed a wider distribution

of N-S thrusts even at higher latitudes. Klimczak *et al.* (2015) assess that a pure tidal despinning model would result in a global set of joints in the upper lithosphere, while tidal despinning acting together with global contraction would cause N–S trending thrust faults towards the equator. This latter scenario is also in accordance with the Matsuyama & Nimmo (2009) model. Dombard & Hauck (2008) hypothesized that tidal despinning forces ceased just before the LHB period since there is a lack of latitudinal pattern in the distribution of lobate scarps, but post-LHB global contraction may have reactivated old despinning structures, inheriting their orientation. As for the tidal despinning models of Matsuyama & Nimmo (2009) or Klimczak *et al.* (2015), the mantle convection model for Mercury advanced by King (2008, Fig. 16c), also considers the contribution of global contraction and predicts a pattern of sheet-like upwelling regions consistent with the distribution of lobate scarps from Watters *et al.* (2004). King (2008) states that mantle convection could be still active today. Other authors support the mantle convection theory, although there is still not enough evidence to confirm its activity at present (e.g. Michel *et al.*, 2013; Massironi *et al.*, 2015).

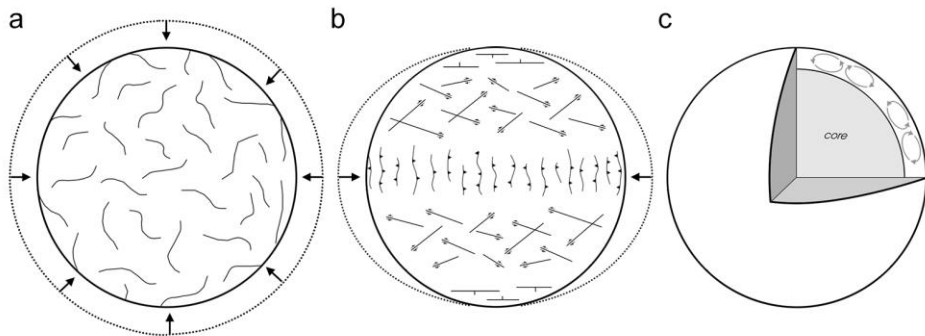


Figure 1.16. Scheme of the three proposed tectonic models for Mercury: a) global contraction due to core solidification; b) tidal despinning; c) mantle convection. Image from Massironi *et al.* (2015).

1.4. Victoria quadrangle (H2)

During the M10 geologic mapping campaign, Mercury was officially divided into 15 quadrangles (see Davies *et al.*, 1978) named after albedo features and also after prominent topographic features where M10 coverage was available (Fig. 1.17). As soon as MESSENGER mission completed the global coverage of Mercury, quadrangle boundaries were slightly changed and the missing quadrangle topographic feature names were assigned (Fig. 1.18).

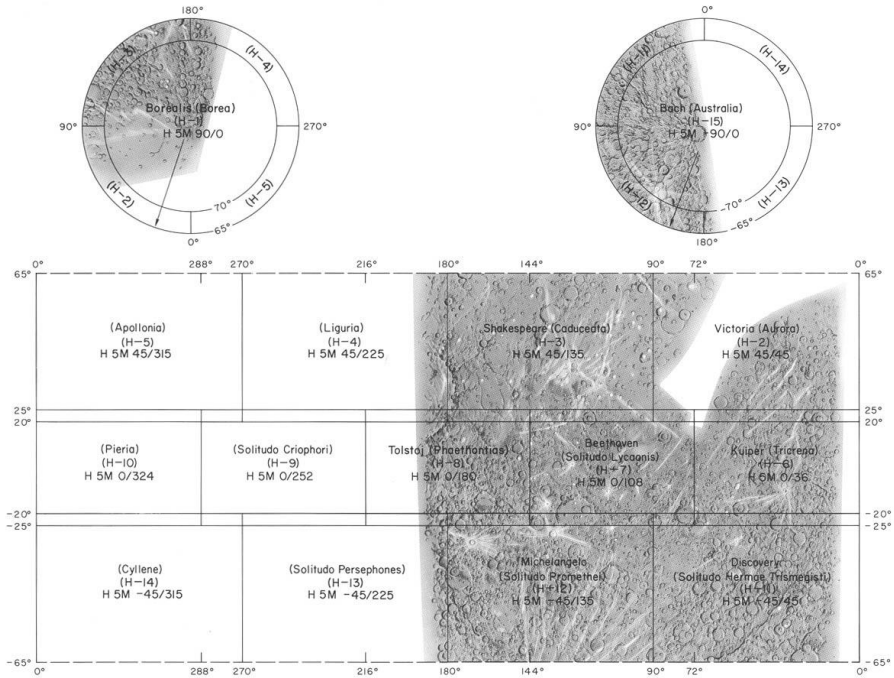


Figure 1.17. Subdivision of Mercury in 15 quadrangles from Davies *et al.* (1978) in equirectangular projection (positive West). Names on quadrangles covered by the shaded relief map are taken from prominent feature names. Names between parentheses are derived from albedo features of telescopic observations.

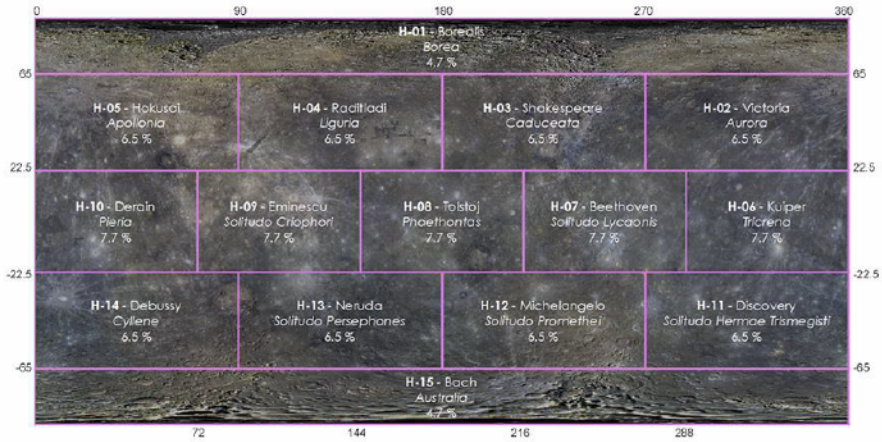


Figure 1.18. Mercury's new quadrangle boundaries as decided by MESSENGER team on MDIS 8-color basemap (665 mpp) in equirectangular projection (positive East) centered at 180° E. On each quadrangle the following information is indicated: quadrangle code in bold (e.g. H-01), quadrangle feature-derived name (italic) and quadrangle coverage percentage.

Victoria quadrangle (270°E-360°E; 22.5°N-65°N) was formerly named Aurora after the corresponding albedo region (see Fig. 1.17a). The name Victoria comes from the lobate scarp at long. ~340°E (Fig. 1.19). This structure is indeed the most prominent feature in the area, since it is aligned with Endeavour Rupes and Antoniadi Dorsum creating a N–S striking fault system ~900 km long.

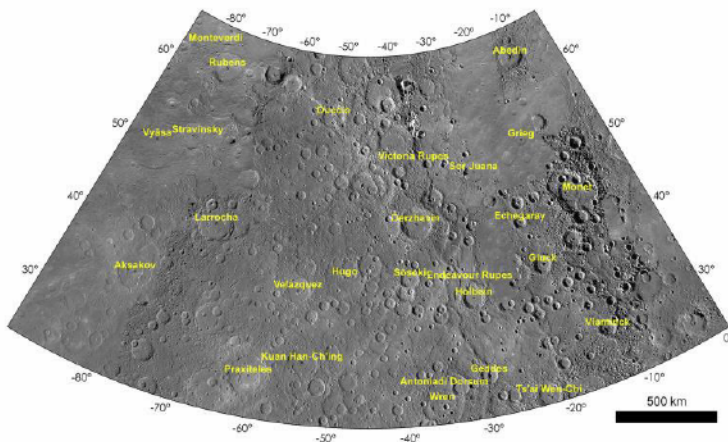


Figure 1.19. MESSENGER MDIS 250 mpp basemap of Victoria quadrangle (new boundaries in Fig.18) in Lambert conformal conic projection (standard parallels: 30° N, 58° N) with official IAU nomenclature labels.

After the first geologic map made by McGill & King (1983, Fig. 1.20) more than 60% of Victoria quadrangle still remained unmapped because of the lack of M10 basemap images, since in that region, M10 coverage was characterised by an unfamed stripe (see Fig. 1.3). In their map, McGill & King (1983) use five classes of craters following the USGS system discussed in Chapter 1.3.2, making a distinction between proximal rim materials and distant radial textured materials for each crater when visible. In this region they were able to map all the unit terrains known on Mercury: intercrater plains, intermediate plains and smooth plains. Main structures were mapped as *ridge crests* since the available basemap did not provide much resolution or lighting variability.

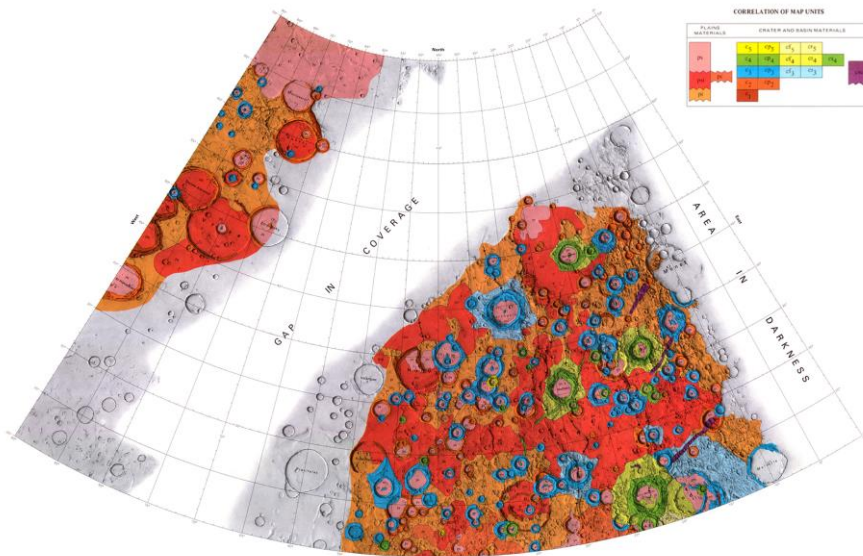


Figure 1.20. Geologic map of Victoria quadrangle H2 (old boundaries in Fig 1.17) as mapped by McGill & King (1983) in Lambert conformal conic projection (standard parallels: 30° N, 60° N).

Today, the Victoria quadrangle still lacks a complete geologic map. Considering the relevance of the structures located in this quadrangle, a geologic map and related structural analysis of H2 were selected as a primary goal of the present project to gain insights into the tectonics of the whole planet.

2. Data

The realisation of a planetary geologic map requires remote sensed imagery and topographic data that constitute the basis for a photogeologic interpretation. The most up to date data for Mercury are acquired by MESSENGER spacecraft (see Chapter 1.1) and released for public use every six months (Tab. 2.1).

Table 2.1. MESSENGER past and scheduled data releases.

Release #	Data Acquisition	Release to Public	Main events
15	Aug. 3, 2004 – Mar. 17, 2015	Mar. 4, 2016	
14	Aug. 3, 2004 – Mar. 17, 2015	Sep. 4, 2015	
13	Aug. 3, 2004 – Sep. 17, 2014	Mar. 6, 2015	
12	Aug. 3, 2004 – Mar. 17, 2014	Sep. 5, 2014	
11	Aug. 3, 2004 – Sep. 17, 2013	Mar. 7, 2014	
10	Sep. 18, 2012 – Mar. 17, 2013	Sep. 6, 2013	End of extended mission 1
9	Mar. 26, 2012 – Sep. 17, 2012	Mar. 8, 2013	
8	Sep. 18, 2011 – Mar. 25, 2012	Sep. 7, 2012	End of primary mission
7	May 19, 2011 – Sep. 17, 2011	Mar. 8, 2012	
6	Sep. 30, 2009 – May 18, 2011	Sep. 8, 2011	Mercury orbit insertion
5	Oct. 21, 2008 – Sep. 29, 2009	Mar. 15, 2010	
4	Jan. 15, 2008 – Oct. 20, 2008	Apr. 15, 2009	3 rd Mercury flyby
3	Jun. 6, 2007 – Jan. 14, 2008	Jul. 15, 2008	2 nd Mercury flyby
2	Aug. 3, 2004 – Jun. 5, 2007	Dec. 15, 2007	1 st Mercury flyby
1	Ground calibration data	On request	Earth and Venus flybys

Table from NASA PDS Geosciences Node, Washington University in St. Louis.

As of this writing, 12 releases are available to the public (see Tab. 2.1), but only releases 3 to 11 were taken into consideration for this thesis. MESSENGER releases contain a large variety of data divided into specific datasets for each instrument. Imagery coming from MDIS WAC and NAC were released as Experiment Data Record (EDR), Calibrated Data Record (CDR), Derived Data Record (DDR), and Reduced Data

Record (RDR). Understanding of these datasets is fundamental for dealing with their derived final products, such as single projected images, basemaps and mosaics, which represented the basis for the photointerpretation of Victoria H2 quadrangle.

2.1. MESSENGER Datasets

The main source of data used in this work is the MDIS instrument (Hawkins *et al.*, 2007) on-board MESSENGER spacecraft. The following information has been gathered through the MDIS EDR Software Interface Specification (SIS) and the MDIS CDR/RDR SIS available at the Planetary Data System (PDS) Imaging Node (NASA/USGS/JPL).

EDR data consist of single-frame almost-raw images. These are the primary data coming from the spacecraft with information attached on a PDS label associated with each image. PDS labels contain fundamental information on the spacecraft position at the time of the frame shot (*e.g.* time, celestial coordinates, incidence angle, emission angle, etc.).

CDR data are a subset of EDR data; they consist in single-frame images calibrated in units of radiance (RA), photometrically corrected reflectance (RE) or radiance factor (I/F, IF), the ratio between measured radiance and a calculated radiance, which would be measured from an ideal diffusely reflecting surface (Lambertian surface). CDRs do not consist of geometrically corrected images.

DDR data contain geometrical information, such as latitude, longitude, incidence angle (*i*, the angle between the sun and the surface), emission angle (*e*, the angle between the spacecraft and the surface) and phase angle (*g*, the angle between the incident and reflected light). They are fundamental for the geometrical correction of CDR frames and production of RDR data.

RDR data consist in two different products: map projected Basemap RDR (BDR) and map projected Multispectral RDR (MDR). BDR products are the result of the global monochrome basemap campaign held during MESSENGER Primary Mission. In this basemap MDIS NAC and WAC-G (*G* = WAC filter corresponding to 750 nm bandpass, very similar to the NAC filter), each image is photometrically normalized to $i=30^\circ$, $e=0^\circ$

and a resolution of 256 pixels per degree (ppd). The use of both WAC and NAC images depended on the highly elliptical orbit of MESSENGER around Mercury: WAC images were taken preferentially at the periapse where the spacecraft reached its minimum altitude of 200 km, while NAC images were taken preferentially at apoapse where MESSENGER reached 13100 km of altitude during the primary mission. MDR products are photometrically corrected like BDRs, but with a resolution of 64 ppd. MDRs use 8 of the 11 WAC filters to obtain coloured basemaps. Another version of the MDR acquired during MESSENGER Extended Mission (started April 2012), the MD3, is compiled at 128 ppd and uses 3 of the 11 WAC filters. BDRs and MDRs are divided into 56 tiles (54 equatorial and 2 polar), corresponding to the NW, NE, SW and SE quarters of the 15 quadrangles in figure 1.19.

2.2. Spatial reference

Before examining the mosaics used for mapping H2 quadrangle, a spatial reference must be defined in order to minimize distortions inside the mapped area.

Datum

Mercury can be approximated to a sphere of 2439.7 km radius (*i.e. datum* "Mercury 2000", IAU approved). However the MESSENGER team slightly changed this parameter and it was approximated to 2440.0 km, often unofficially referred to as "Mercury 2010" *datum*. In the past Mariner 10 mosaics the used *datum* was of 2439.0 km radius. Although these values are very similar, it is important to define a common value for all raster images and features when importing the data into the Geographical Information System (GIS) software. In the present work, I used the "Mercury 2010" value of 2440.0 km as the reference *datum*, thus a geographic transformation was applied when using older Mercury 2000 and Mariner 10 *data*.

Projections

Victoria quadrangle is located at mid latitudes (*i.e.* 22.5°N; 65°N) and in this range the use of a Lambert Conformal Conic (LCC) projection is preferable (see Davies *et al.*, 1978). The LCC projection uses two standard parallels that represent the secants between the sphere and the cone of projection. This means that the scale of features is

true along the secants, a bit smaller between them and a bit larger beyond them. A common rule is to fix the standard parallels to a distance of 1/6 and 5/6 of the latitudinal range (Deetz & Adams, 1934). When H2 quadrangle was defined for the first time, its latitudinal range was 20°N – 70°N and the standard parallels were fixed at 30°N and 60°N latitude. Considering the newly defined boundaries, I decided to change the second standard parallel to 58°N. Therefore the geographic projection used for the basemaps is:

Lambert Conformal Conic H2	
First Standard Parallel:	30
Second Standard Parallel:	58
Latitude of Origin:	0
Central Meridian:	315
Longitude Domain:	Positive East

However, when single features were analysed in detail (*e.g.* Chapter 3.2), a stereographic projection centred on the object was preferred to minimize shape distortions (see also Kneissl *et al.*, 2011).

2.3. Raster layers

2.3.1. Basemaps

Due to the large variety of data available and the gradual release of datasets, several basemaps were taken into consideration during the realization of the H2 geologic map. A schematic summary of the used basemaps is shown in table 2.2, the listing somewhat reflects an importance order from top to bottom.

Table 2.2. List of basemaps used for Victoria quadrangle.

H2 Trim	Original basemap	Resolution	Source
H2-Bm-0	MDIS_BDR_256PPD_Hxxdd ^a	166 mpp	PDS
H2-Bm-1	20130514_complete_mono_basem	250 mpp	NASA/JHUAPL/CIW ^b
H2-Bm-2	MDIS_v8_750nm_250mpp	250 mpp	NASA/JHUAPL/CIW ^b
H2-Bm-3	MDIS_v7_mono_250mpp	250 mpp	NASA/JHUAPL/CIW ^b
H2-Bm-4	MDIS_v6_mono_250mpp	250 mpp	NASA/JHUAPL/CIW ^b
H2-Bm-5	M1_M2_M3_M10Filt	500 mpp	USGS ^c
H2-Bm-6	MESSENGER_color_mono	200 mpp	USGS ^d
H2-Bm-7	usgs_20110913_albedo	200 mpp	USGS ^d
H2-Bm-8	MDIS_v0_3color	332 mpp	NASA/JHUAPL/CIW ^b
H2-Bm-9	MDIS_v5_8color	665 mpp	NASA/JHUAPL/CIW ^b
H2-Bm-10	M10 Mercury Mosaic (Calibrated)	1000 mpp	ASU ^e
H2-Bm-11	M10 Mercury Shaded Relief	1330 mpp	USGS/ASU ^e

^axx indicates the quadrangles and dd indicates the tiles NP, NW, NE, SE, SE shown in Fig. 2.1

^bBecker et al. (2009)

^cJHUAPL, Johns Hopkins University, Applied Physics Laboratory. CIW, Carnegie Institute of Washington

^dMercuryGIS_DVD_v03 available at USGS FTP

^eArizona State University, Mariner 10 Image Archive

The newly defined boundaries for H2 quadrangle do not include any overlap with the nearby quadrangles (H1 to the North, H6 and H7 to the South, H3 to the West, H5 to the East, and H10 in the South-East corner, see Fig. 1.19). Although H2 was mapped only inside the indicated boundaries, an overlap of 5° was added to all basemaps for cartographic purposes (*e.g.* for a better interpretation of features located at map boundaries). To obtain H2-Bm-0 (see Tab. 2.2), BDR tiles of Victoria quadrangle were mosaicked together with the nearby tiles to obtain a 5° overlap. The mosaicked tiles are 13 in total (Fig. 2.1) and were processed with USGS ISIS3 (Integrated Software for Imagers and Spectrometers v3, Gaddis *et al.*, 1997; Torson & Becker, 1997; Eliason *et al.*, 1997, see Appendix A for processing techniques).

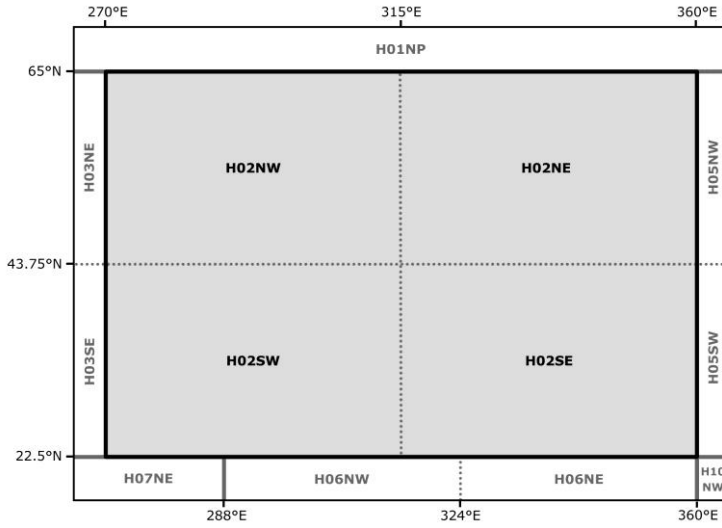


Figure 2.1. MDIS BDR tiles used to mosaic H2-Bm-0 with an overlap of 5°. Each tile is formally named Hxxdd in the PDS, where xx is the quadrangle number and dd is the tile position, NP (North Polar), NW, NE, SW or SE.

Each BDR tile used to mosaic H2 and its 5° overlap, is available in equirectangular projection centred on the tile centre, for this reason the mosaicked basemap was then re-projected in LCC projection. All the other basemaps in table 2.2 were simply trimmed to the desired overlap and re-projected with LCC.

Since there is no highly controlled base for Mercury yet (such as the Lunar Orbiter Laser Altimeter data for the Moon), all the used basemaps show some discrepancies and are not perfectly georeferenced to each other. During the gradual release of data, the basemaps with the best resolution and coverage were chosen as a reference layer. As of this writing, H2-Bm-0 is the basemap with the highest resolution (256 ppd, ~166 mpp) and as soon as it was available, it was considered as the ultimate reference basemap for the geologic mapping (Fig. 2.2).

Basemaps H2-Bm-1 to -4 were trimmed from the global mosaics that were compiled from PDS data and released gradually during MESSENGER mission in the NASA/JHUAPL/CIW website (releases 6 to 9 in Tab. 2.1). Figures 2.3 to 2.6 are presented in inverse order (*i.e.* H2-Bm-4 to -1) to show the gradual mosaic improvement in time. They are very similar to each other and also to H2-Bm-0, because they were made during the base map imaging campaign of MESSENGER primary

mission and they all use almost the same source frames. Nonetheless, they still present some areas where different mosaic tiles were used, sometimes showing different lighting conditions (*e.g.* Fig. 2.7); a different lighting direction can often make the difference avoiding common biases while drawing structures (*e.g.* Di Achille *et al.*, 2012). A fifth global mosaic called "MDIS v9" (250 mpp) was released after "MDIS v8", this version of the global mosaic was not considered since it is identical to the BDR mosaic but with a lower resolution (250 mpp instead of 166 mpp); moreover it was soon substituted by the "MDIS complete" version that added some more tiles to fill the remaining gaps. BDRs, "MDIS v9" and "MDIS Complete" were all part of PDS Release 9 (Tab. 2.1) and they all use some of the new frames coming from MESSENGER extended mission high-incidence-angle campaign, that is why they look slightly different from the past releases (*e.g.* compare H2 eastern part, $\sim 10^\circ\text{W}$, in Figs. 2.2, 2.5, and 2.6).

H2-Bm-0

source: MDIS_BDR_256PPD_H02

500 km

scale is true at lat. 30°N and 58°N

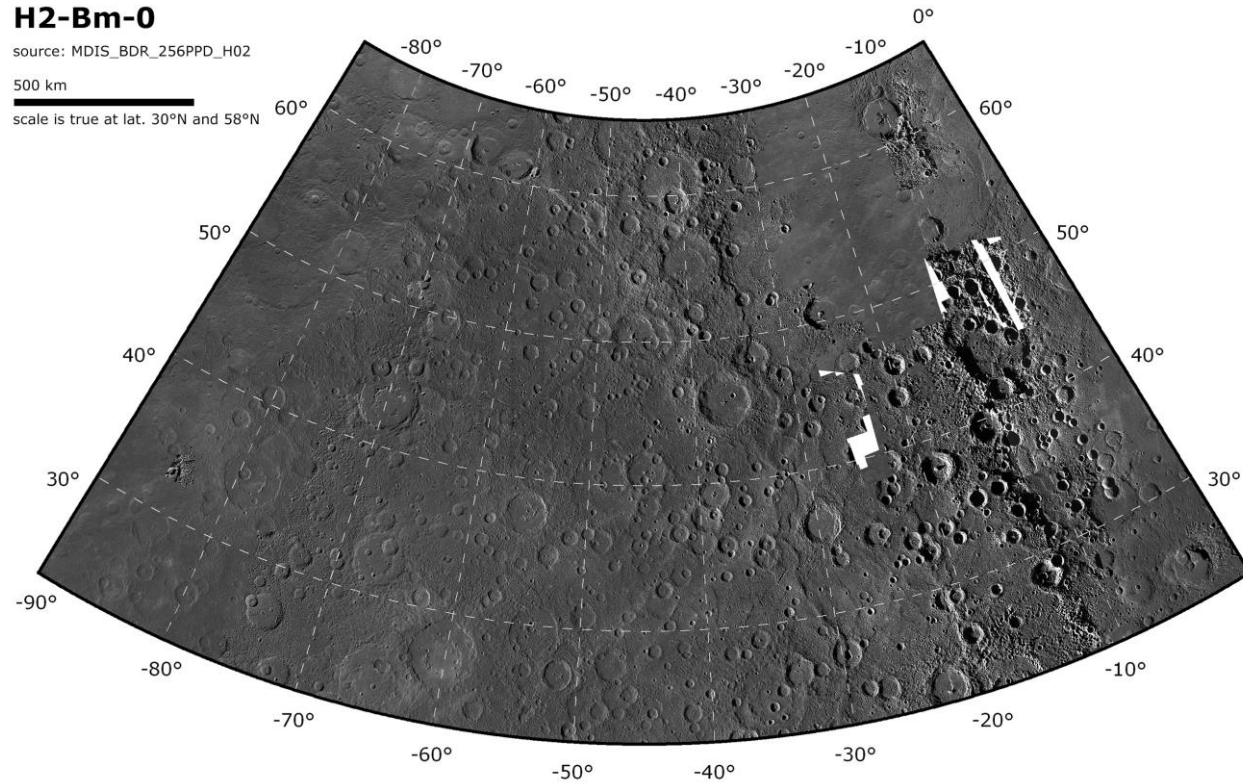


Figure 2.2. H2-Bm-0 basemap in Lambert conformal conic projection (see details in Chapter 2.2) obtained from MDIS BDR tiles (see non-overlapping H2 tiles in Fig. 2.1). Although it presents some gaps at $\sim 10^\circ\text{W}$ and $\sim 25^\circ\text{W}$ longitude, it was chosen as the reference basemap for the geologic mapping since it has the highest resolution available (256 ppd). The BDRs coverage shown in this basemap is the same as "MDIS v9" released on March 8th 2013 (PDS release 9, Tab. 2.1).

H2-Bm-4

source: MDIS_v6_mono_250mpp

500 km

scale is true at lat. 30°N and 58°N

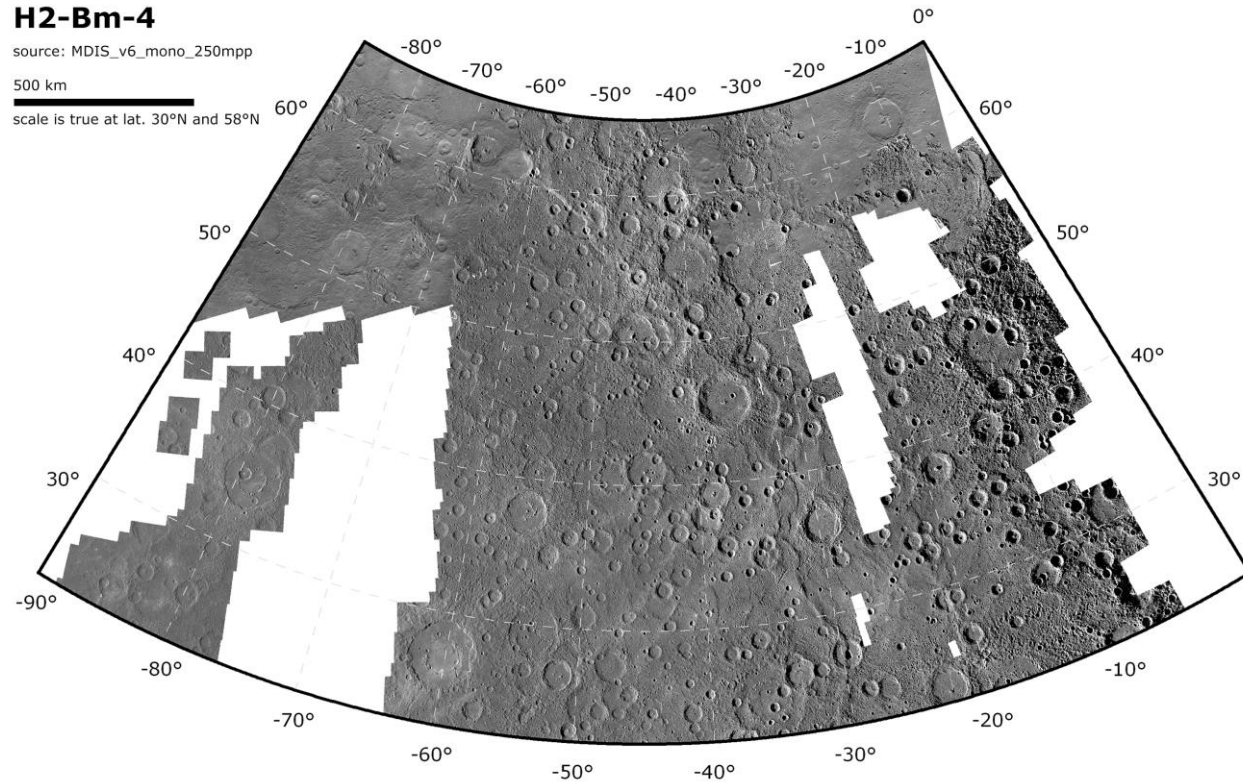


Figure 2.3. H2-Bm-4 basemap in Lambert conformal conic projection. This basemap was trimmed from "MDIS v6" mosaic of PDS images at 250 mpp, released on September 8th, 2011 (PDS release 6, Tab. 2.1). This picture shows the exact boundaries of H2 quadrangle without overlap. Courtesy of NASA/JHUAPL/CIW.

H2-Bm-3

source: MDIS_v7_mono_250mpp

500 km

scale is true at lat. 30°N and 58°N

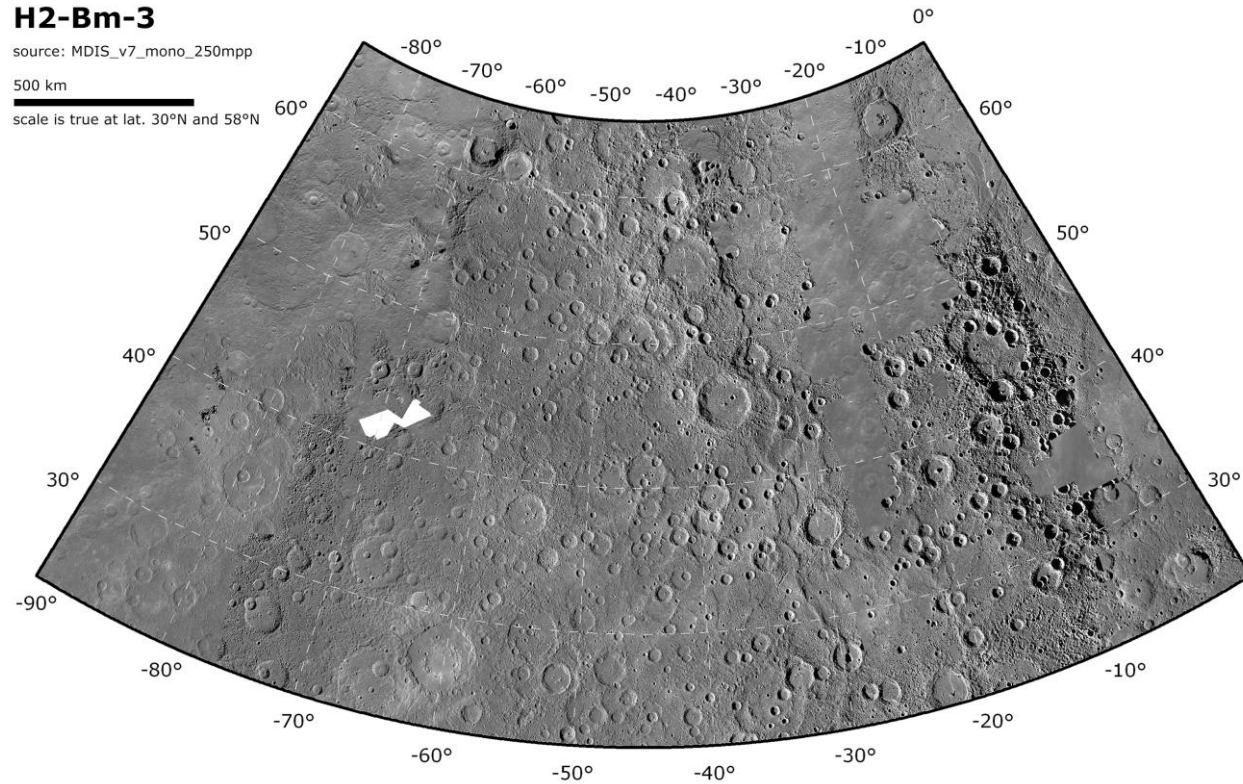


Figure 2.4. H2-Bm-3 basemap in Lambert conformal conic projection. This basemap was trimmed from "MDIS v7" mosaic of PDS images at 250 mpp, released on March 8th, 2012 (PDS release 7, Tab. 2.1). This picture shows the exact boundaries of H2 quadrangle without overlap. Courtesy of NASA/JHUAPL/CIW.

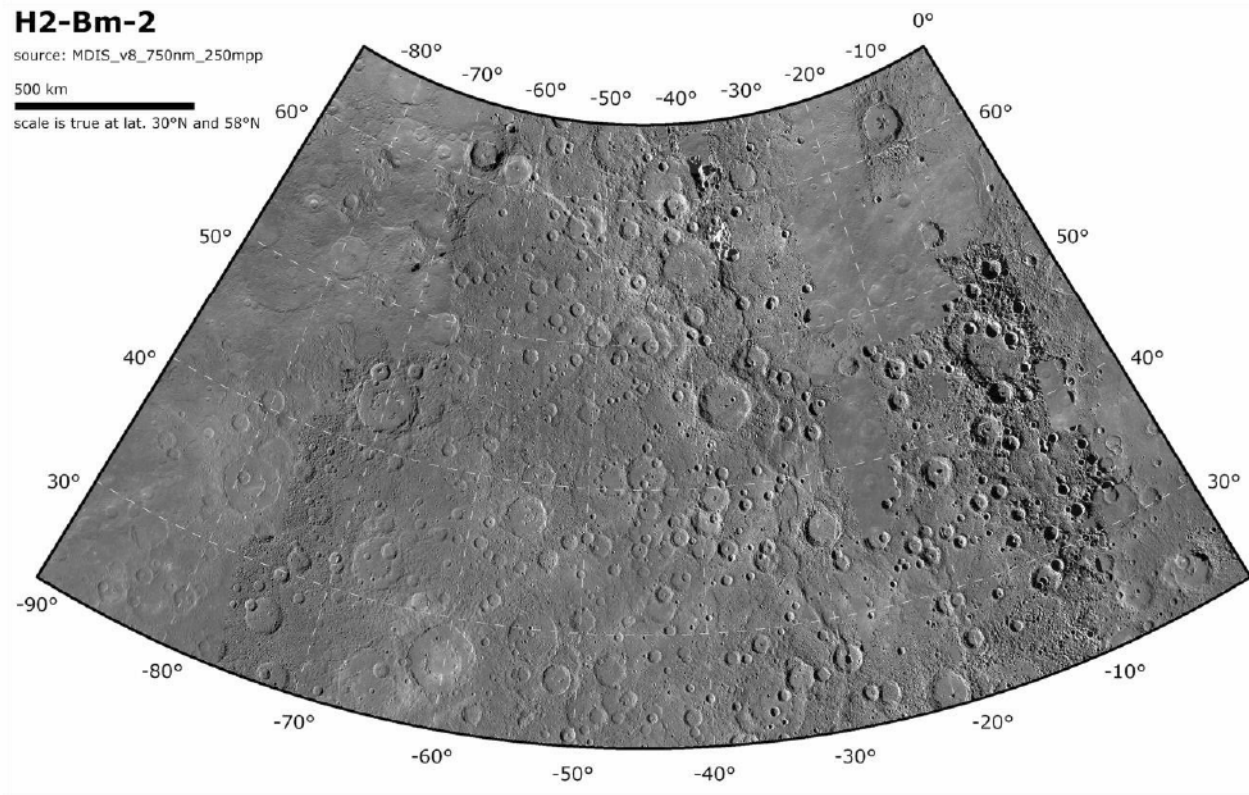


Figure 2.5. H2-Bm-2 basemap in Lambert conformal conic projection. This basemap was trimmed from "MDIS v8" mosaic of PDS images at 250 mpp, released on September 7th, 2012 (PDS release 8, Tab. 2.1). This version of the basemap already provided 100% coverage of H2 quadrangle. This picture shows the exact boundaries of H2 quadrangle without overlap. Courtesy of NASA/JHUAPL/CIW.

H2-Bm-1

source: 20130514_complete_mono_basemap

500 km

scale is true at lat. 30°N and 58°N

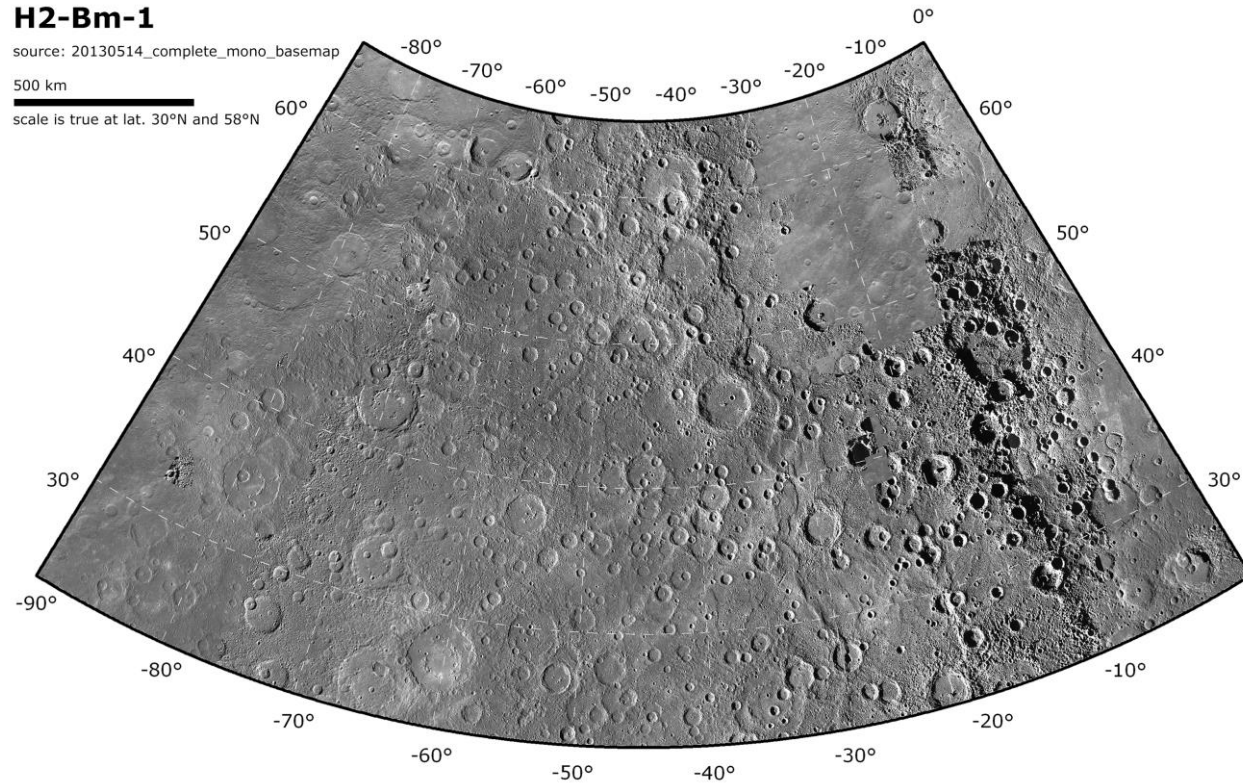


Figure 2.6. H2-Bm-1 basemap in Lambert conformal conic projection. This basemap was trimmed from "MDIS complete" mosaic of PDS images at 250 mpp, obtained from "MDIS v9" released on March 8th, 2013 (PDS release 9, Tab. 2.1) and some additional PDS tiles to fill the gaps. This picture shows the exact boundaries of H2 quadrangle without overlap. Courtesy of NASA/JHUAPL/CIW.

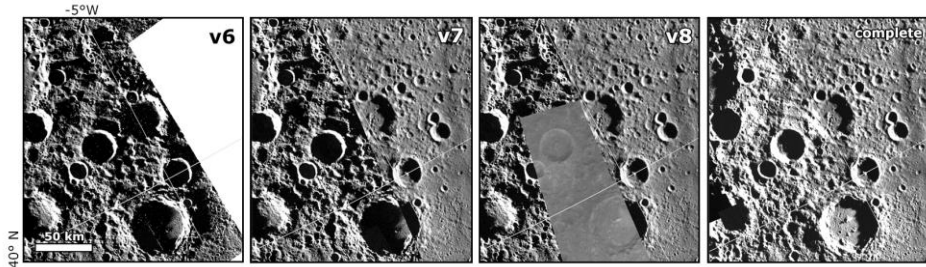


Figure 2.7. Comparison of H2-Bm-1 to -4 (datasets release 6 to 9/complete). It is clear from these images that the illumination direction is opposite between "MDIS v6" and "MDIS complete". The intermediate versions of the basemap show a patchy appearance with lighting geometries common to both "v6" and "complete". Note also the low incidence angle area inside "v8".

H2-Bm-5 in figure 2.8 was trimmed from the first global map of Mercury released by the USGS soon after the three MESSENGER flybys (*i.e.* M1, M2, M3; Becker *et al.*, 2009). The three flybys alone already covered 90.9% of Mercury's surface, and by adding the 43% coverage of Mariner 10, Becker *et al.* (2009) obtained a near global mosaic of the planet (~97%) at 500 mpp resolution. Although H2-Bm-5 is of lower resolution with respect to H2-Bm-0, it represents an important source of data because it offers higher shadow contrasts in the H2 western region (*e.g.* Fig. 2.9); this is due to the vicinity of the terminator during M2 flyby. As stated before, this difference between the two basemaps is very important to detect structures that are hidden in the low-incidence-angle western area of H2-Bm-0.

Basemap H2-Bm-6 (Fig. 2.10) was trimmed from a partial mosaics processed during Release 6 (source: MercuryGIS_DVD_v03, available in the USGS public FTP) of WAC-G-only frames as part of the colour basemap campaign of MESSENGER primary mission. Basemap H2-Bm7 (Fig. 2.11) was trimmed from an USGS mosaic of MDIS orbital images resampled to 200 mpp, released in September 2011. The above basemaps were used in the early stages of H2 geologic mapping, since they provided a better resolution than "MDIS v6" that was released in the same period. H2-Bm-6 (Fig. 2.10) was particularly useful because it offered more continuity in specific areas and also different lighting geometries (*e.g.* Fig. 2.12).

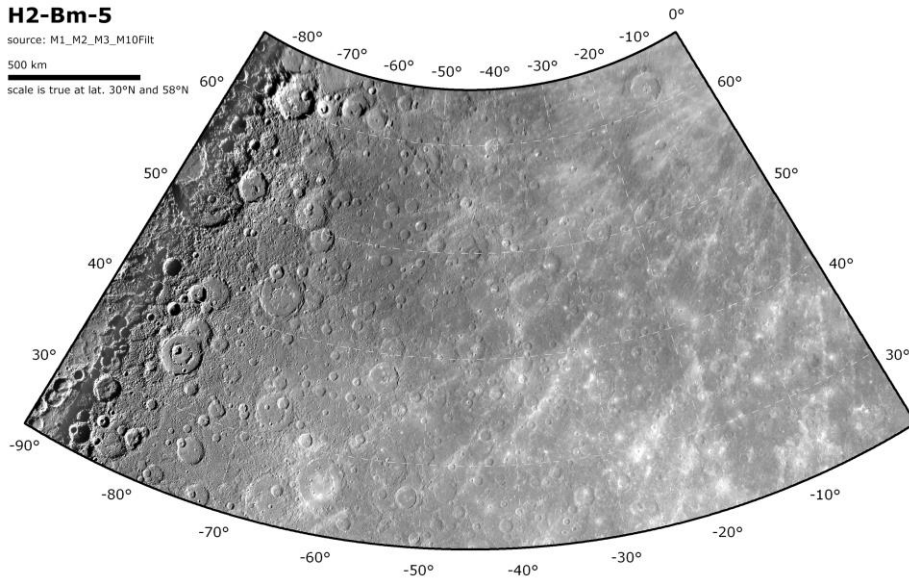


Figure 2.8. H2-Bm-5 basemap in Lambert conformal conic projection trimmed from USGS mosaic of MESSENGER M1, M2, M3 flybys plus Mariner 10 images (Becker *et al.*, 2009). MESSENGER flyby images completely substitute Mariner 10 information in this area. Note the high-incidence-angle western area where the lighting geometry abruptly changes direction. This is due to a mosaic boundary between M1 approaching spacecraft images to the extreme West and M2 departing spacecraft images to the East (Becker *et al.*, 2009). This picture shows the exact boundaries of H2 quadrangle without overlap.

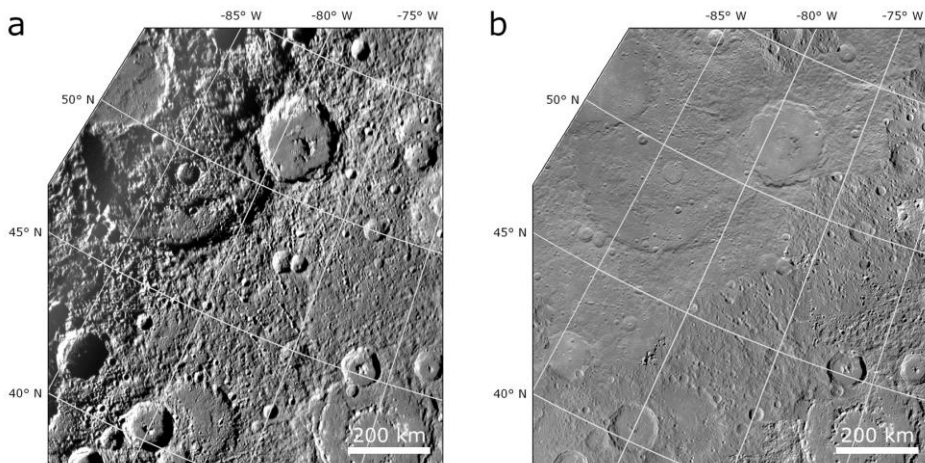


Figure 2.9. Comparison between H2-Bm-5 and H2-Bm-0 western area. a) H2-Bm-5 basemap from Becker *et al.* (2009). b) H2-Bm-0 basemap from BDR tiles, here the lighting geometry does not permit a detailed mapping. Note that the old large crater to the North-West is not clearly visible as in a).

H2-Bm-6

source: MESSENGER_color_mono

500 km

scale is true at lat. 30°N and 58°N

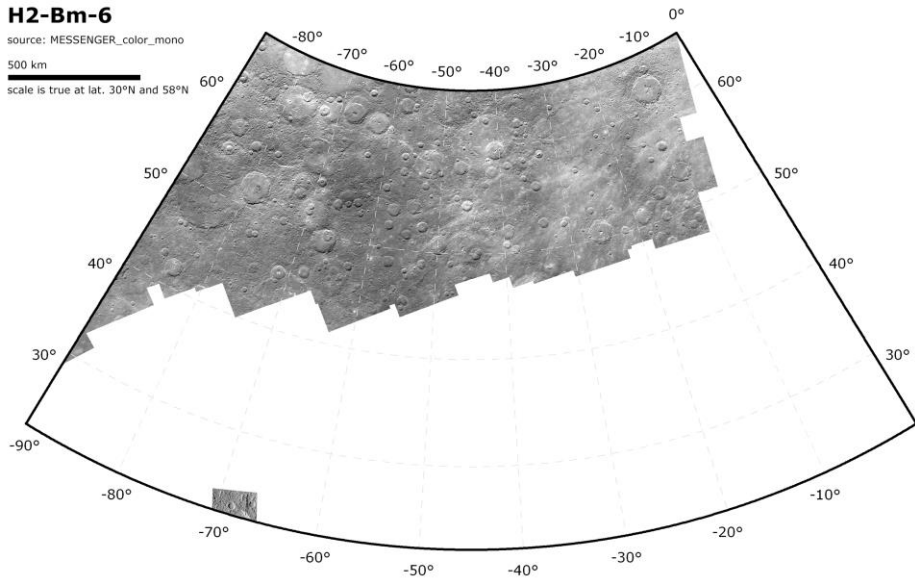


Figure 2.10. H2-Bm-6 basemap in Lambert conformal conic projection. This H2 trim was obtained from a mosaic of MDIS orbital WAC-G images at 200 mpp. This picture shows the exact boundaries of H2 quadrangle without overlap.

H2-Bm-7

source: usgs_20110913_albedo

500 km

scale is true at lat. 30°N and 58°N

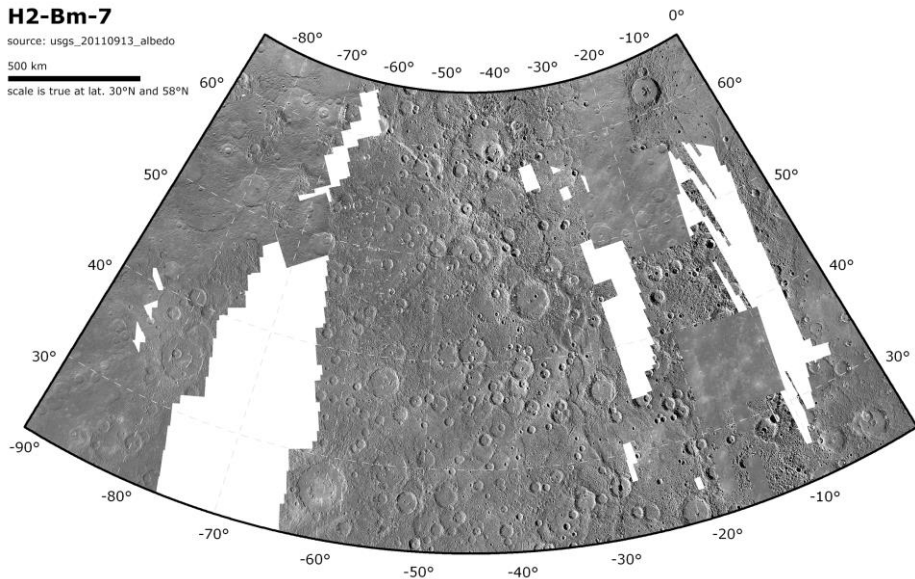


Figure 2.11. H2-Bm-7 basemap in Lambert conformal conic projection. This H2 trim was obtained from a USGS mosaic of MDIS orbital images resampled to 200 mpp (USGS). This picture shows the exact boundaries of H2 quadrangle without overlap.

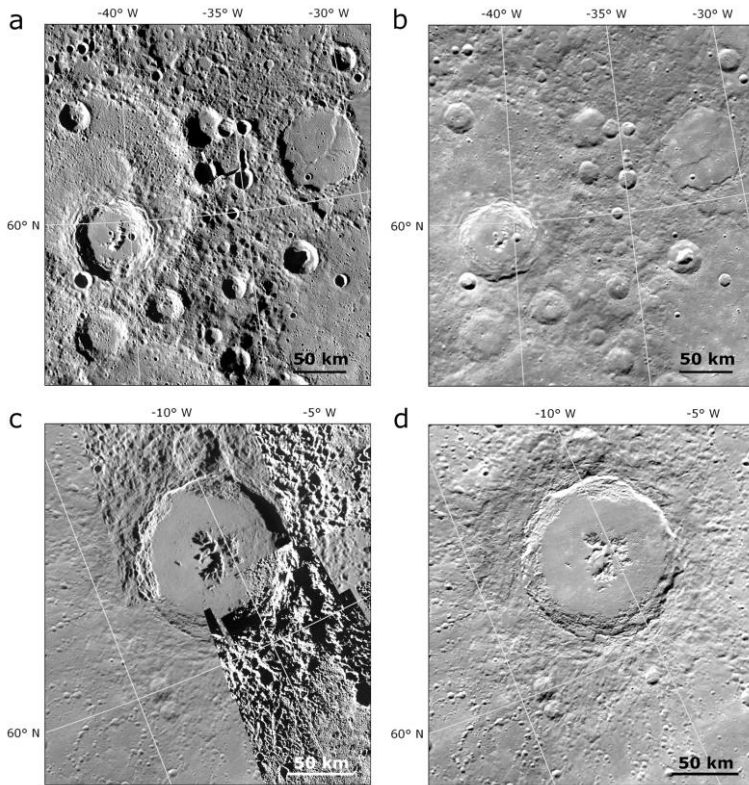


Figure 2.12. Comparison between H2-Bm-0 (~166 mpp) and H2-Bm-6 (200 mpp). a) BDR tile: the illumination direction is from West to East. b) MDIS WAC-G orbital images mosaic: the illumination direction is from South to North and the incidence angle is much lower than a). c) BDR tile: a patchy mosaic covers Abedin Crater. d) MDIS WAC-G orbital images mosaic: a continuous mosaic covers Abedin Crater, thus permitting a better mapping of the ejecta.

H2-Bm-8 and -9 (Figs. 2.13 and 2.14) were trimmed from the two coloured mosaics derived from MDR and MD3 data. Unlike the BDR case, I did not process MDR and MD3 with ISIS3 since they are already provided at their best resolution by the MESSENGER website. They do not offer a good resolution for mapping features, but are still useful within ambiguous regions where texture changes are not so evident in the monochrome basemaps, because of low-incidence-angle frames. Slight colour changes can help to locate these uncertain contacts (*e.g.* Fig. 2.15).

H2-Bm-8

source: MDIS_v0_3color

500 km

scale is true at lat. 30°N and 58°N

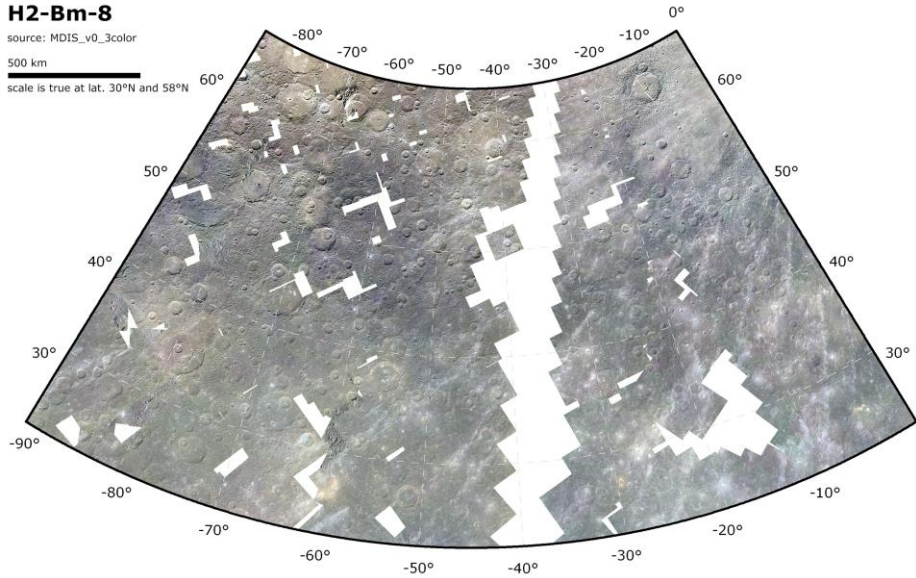


Figure 2.13. H2-Bm-8 basemap in Lambert conformal conic projection, trimmed from the 3-colour mosaic of Mercury at 332 m/pixel derived from the MD3 PDS dataset. This picture shows the exact boundaries of H2 quadrangle without overlap. Courtesy of NASA/JHUAPL/CIW.

H2-Bm-9

source: MDIS_v5_8color

500 km

scale is true at lat. 30°N and 58°N

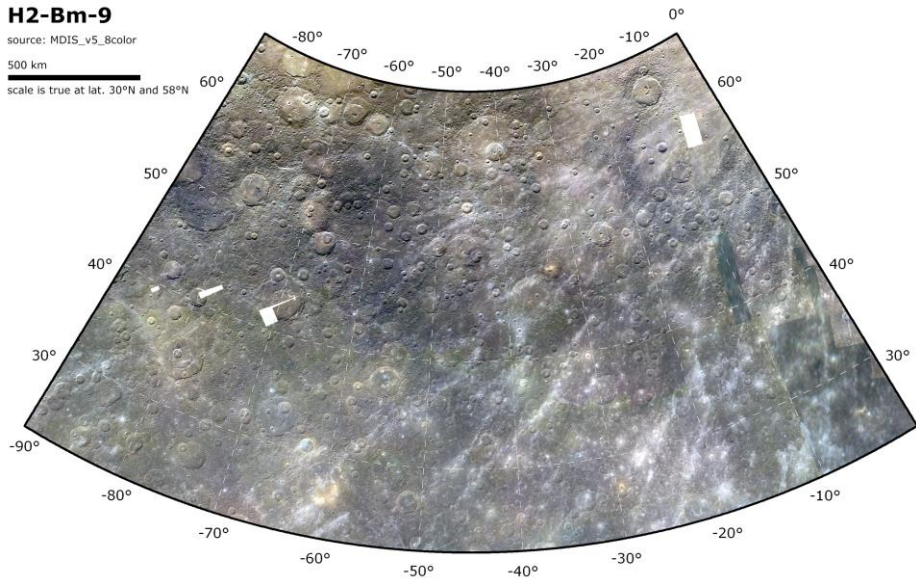


Figure 2.14. H2-Bm-9 basemap in Lambert conformal conic projection, trimmed from the 8-colour mosaic of Mercury at 665 m/pixel derived from the MDR PDS dataset. This picture shows the exact boundaries of H2 quadrangle without overlap. Courtesy of NASA/JHUAPL/CIW.

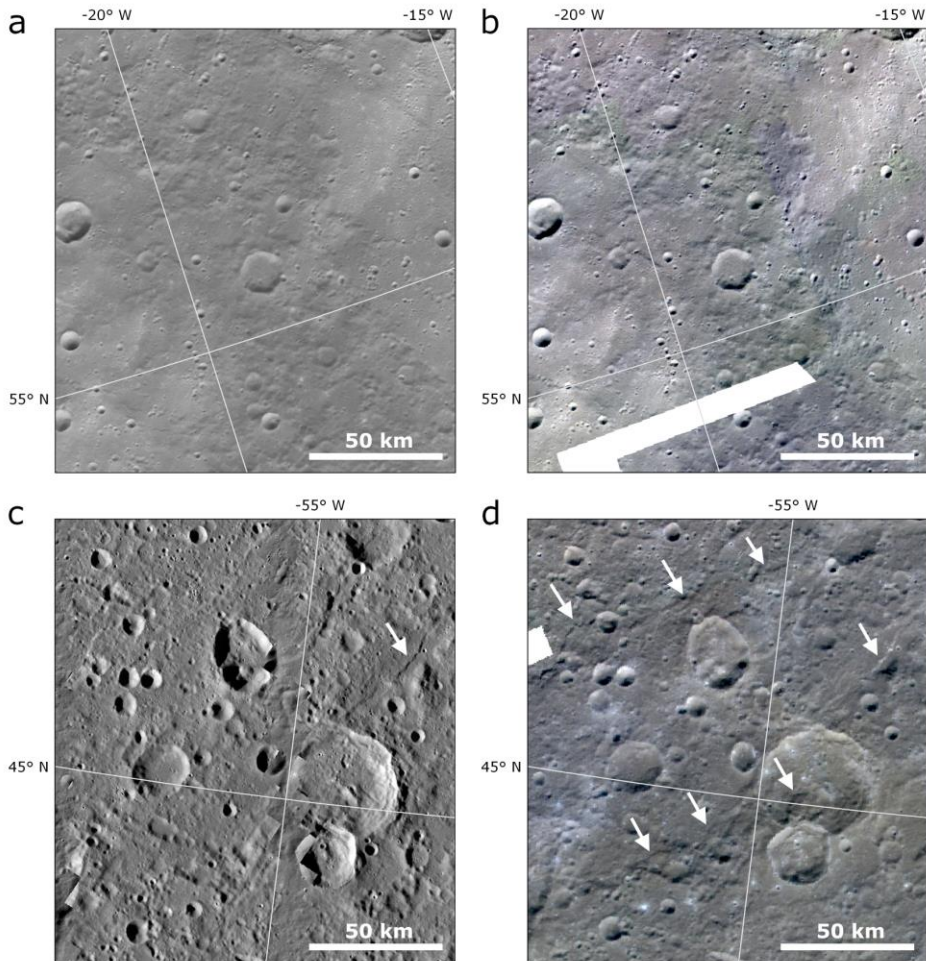


Figure 2.15. Comparison between H2-Bm-0 and H2-Bm-8. a) This BDR trim shows a portion of smooth plains cut by a rough surface, which is poorly visible because of the soft shades of grey caused by a low-incidence-angle lighting geometry. b) This MD3 trim shows the same area in a) with the same lighting geometry but with the central rough surface enhanced by darker bluish colours. c) BDR trim of a cratered terrain area; one small linear feature is visible to the NE (white arrow). d) MD3 trim of the same cratered area in c). More linear features are visible thanks to the different lighting direction (white arrows).

H2-Bm-10 and -11 (Figs. 2.16 to 2.17) were kept as an historical record of the past Mariner 10 mission. Their resolution is very low and the coverage is poor but they are useful for "comparative cartography" with the past work of McGill & King (1983).

H2-Bm-10

source: Mariner 10 calibrated mosaic

500 km

scale is true at lat. 30°N and 58°N

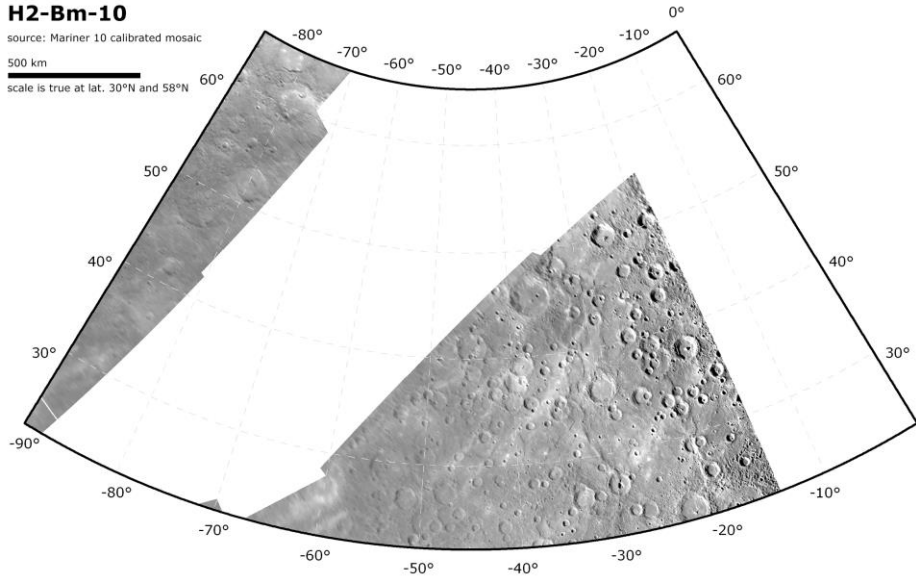


Figure 2.16. H2-Bm-10 basemap in Lambert conformal conic projection. This basemap was trimmed from a calibrated mosaic of Mariner 10 images at 1000 mpp (ASU Mariner 10 image archive). This picture shows the exact boundaries of H2 quadrangle without overlap.

H2-Bm-11

source: Mariner 10 shaded relief

500 km

scale is true at lat. 30°N and 58°N

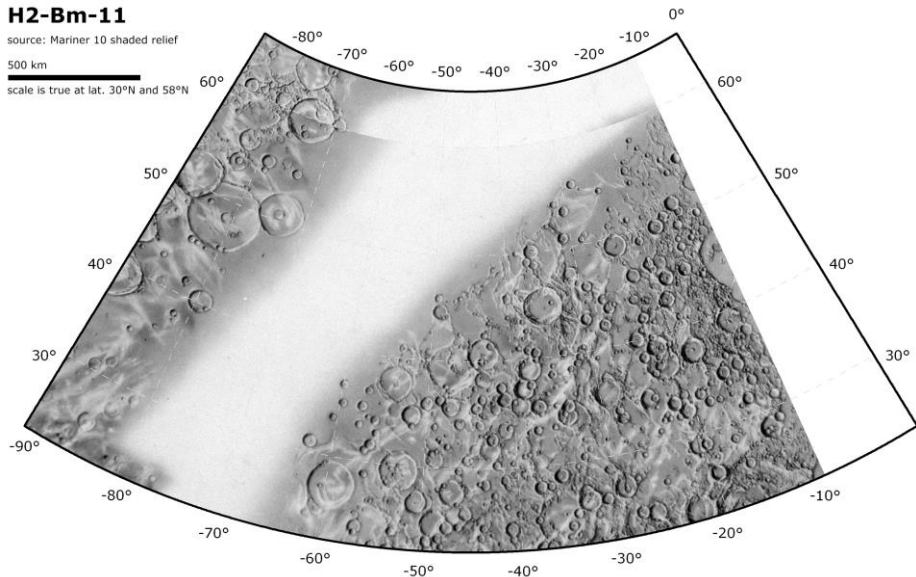


Figure 2.17. H2-Bm-11 basemap in Lambert conformal conic projection, trimmed from the Mariner 10 shaded relief map of Mercury at 1330 mpp, drawn by the USGS cartographer Patricia M. Bridges (Courtesy of NASA/USGS). This picture shows the exact boundaries of H2 quadrangle without overlap.

2.3.2. MDIS single-frames and mosaics

Although H2-Bm-0 associated with the other basemaps in table 2.2 provided enough information for mapping the whole quadrangle, several issues arose from their uneven appearance. It is clear from figure 2.2 that the reference basemap is missing some tiles, especially on its eastern part. These gaps are covered by H2-Bm-1 but with lower resolution. Another issue was represented by extremely high-incidence-angle areas, where long shadows hide or partially cover important features (*e.g.* faulted craters). In the same way, areas with extremely low incidence angles are very difficult to map, since every feature (*e.g.* faults) is apparently "levelled" by the light. These problems were partially avoided by toggling the visibility of each available basemap to compare them and lower the biases deriving from lighting conditions (*e.g.* Di Achille *et al.*, 2012). However, when it was impossible to deal with the gap in resolution among the several basemaps or with the lighting geometry, single frames and partial mosaics had to be processed separately.

As of today, the MESSENGER MDIS instrument has gathered more than 255,000 images and more than 190,000 EDR frames of Mercury are available at the PDS for public use. These frames are easily searchable through the NASA PDS Atlas (<http://pds-imaging.jpl.nasa.gov>), the Orbital Data Explorer (ODE: <http://ode.rsl.wustl.edu>), or the footprints vector layers available for download at ODE that can be consulted directly on the GIS software (Fig. 2.18). Single frames and partial mosaics were processed with ISIS3 using some common pipelines shown in Appendix A. An example of the results is shown in Fig. 2.19. These products were used occasionally, giving the priority, when possible, to the basemaps presented above.

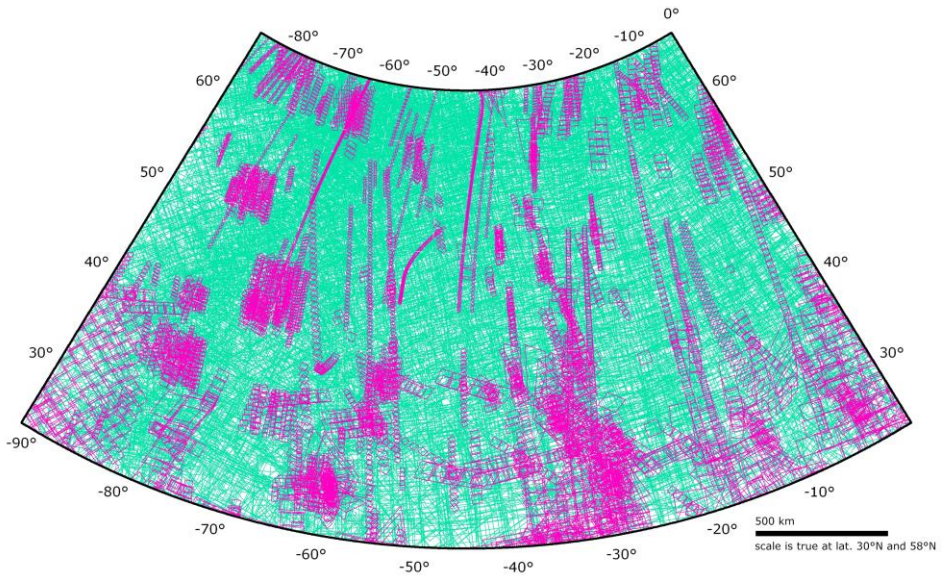


Figure 2.18. MDIS EDR NAC footprints (pink) and MDIS EDR WAC-G orbital images footprints (cyan) available for H2 quadrangle, as of release 12. Note that WAC-G footprint boundaries are not recognisable because of the intense coverage.

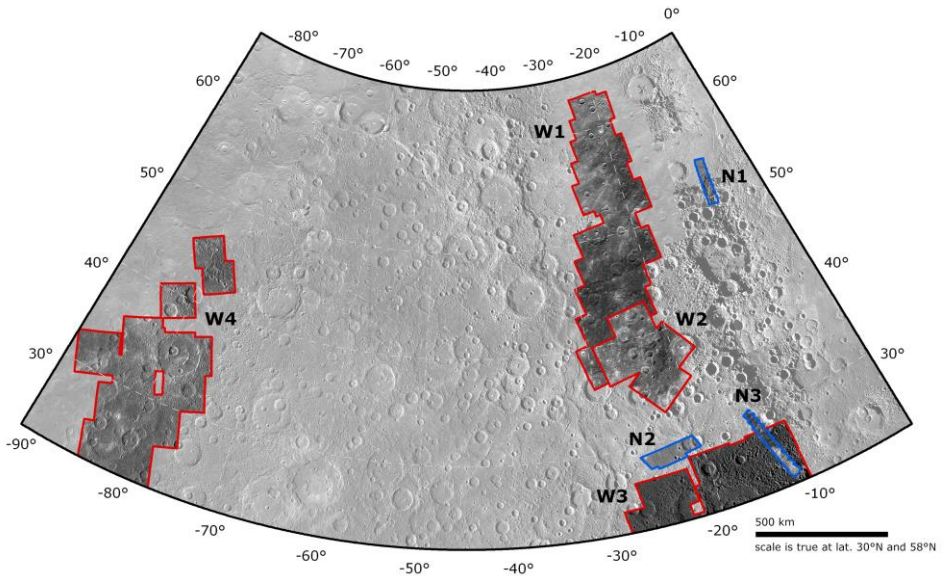


Figure 2.19. Some mosaics produced with ISIS3: red boundaries refer to WAC image mosaics, while blue boundaries refer to NAC image mosaics. W1: 166 mpp pixel mosaic of WAC-G frames. W2: 159 mpp mosaic of WAC-I frames. W3: 232 mpp mosaic of WAC-G frames. W4: 166 mpp mosaic of WAC-G frames. N1: 25 mpp mosaic of NAC frames. N2: 50 mpp mosaic of NAC frames. N3: 31 mpp mosaic of NAC frames.

2.3.3. Topography

When dealing with geologic mapping, topography is usually a mandatory element before starting any cartographic work. However, in planetary geologic mapping, topography is not always available or it has not a sufficient resolution to represent a reliable reference layer. Therefore, topography becomes part of the ancillary data useful to interpret the morphologic evidences of remote sensed images. Unlike the Moon or Mars, Mercury lacks global topographic data. Topographic information for the planet was gathered through two separate sources: 1) DLR (Deutsche Zentrum für Luft- und Raumfahrt, German Aerospace Center) stereo-mosaics (Preusker *et al.*, 2011); 2) MESSENGER MLA data.

The DLR stereo-topography is a product of MESSENGER flybys M1, M2 and M3 and cover 30% of the planet with a resolution of 1000 mpp (Preusker *et al.*, 2011). In this thesis DLR stereo-topography was used for the widespread analysis of faulted craters (Galluzzi *et al.*, 2015, see Chapter 3.2) just before MLA data became available. Victoria quadrangle however, is quite well covered by the M2 stereo-mosaic (~80%) as shown in figure 2.20.

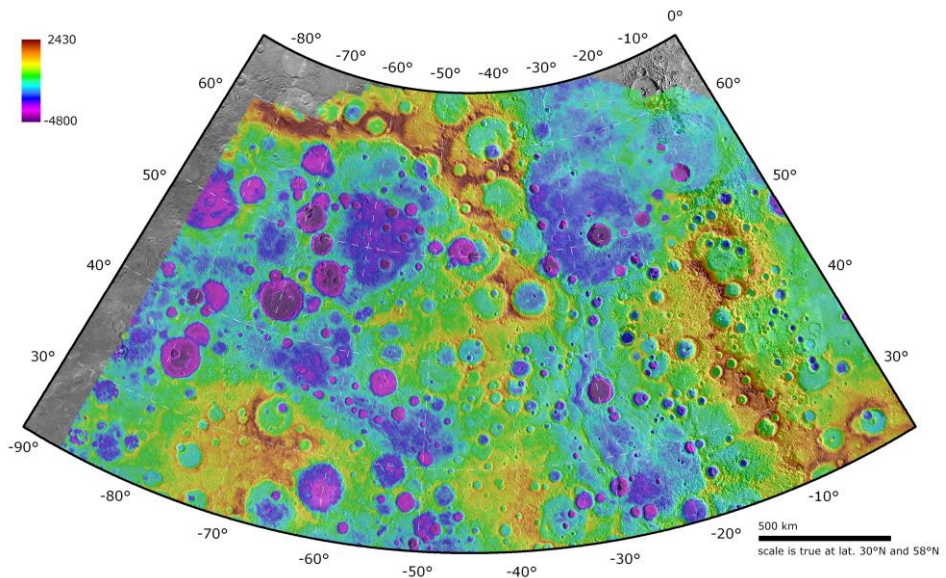


Figure 2.20. DLR M2 stereo-mosaic trimmed to H2 boundaries (Preusker *et al.*, 2011). This product has a nominal resolution of 1000 mpp.

The preliminary MESSENGER MLA datasets became available as Gridded Data Record (GDR), thus as usable raster layers, between releases 10 (resolution 1000 mpp) and 11 (resolution from 665 to 500 mpp) and added topographic information for Mercury's northern hemisphere. The lack of topography in the southern hemisphere results from the highly elliptical orbit of MESSENGER spacecraft, which is also the reason of a southward decreasing resolution. Victoria quadrangle is completely covered by a 665 mpp MLA topography (Fig. 2.21) and a 500 mpp topography is also available near the North pole (Fig. 2.22). However, the 665 mpp layer is affected by the lack of information in its southern area. This issue is evident when analysing the MLA tracks footprints in figure 2.23. The topographic information between adjacent tracks comes from the interpolation of the near MLA spots (located along the tracks), thus if these spots are too far from each other the topographic information is poor. This is why it is important to use both MLA topography and stereo-topography: the first one gathers more accurate measures on single spots and small interpolated areas, while the second one offers a more complete view of the surface features, especially inside badly interpolated areas (*e.g.* Fig. 2.24).

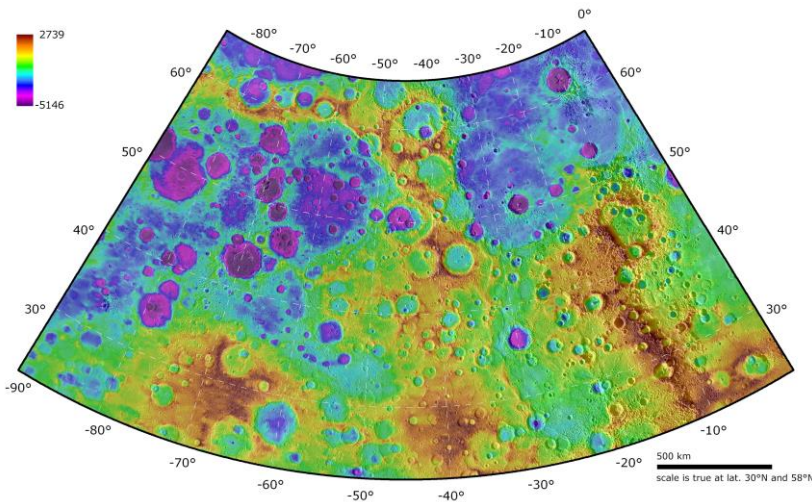


Figure 2.21. MLA topography at a nominal 665 mpp resolution, trimmed to H2 quadrangle. Note the fuzzy appearance of the southern area. See also MLA tracks in figure 2.23.

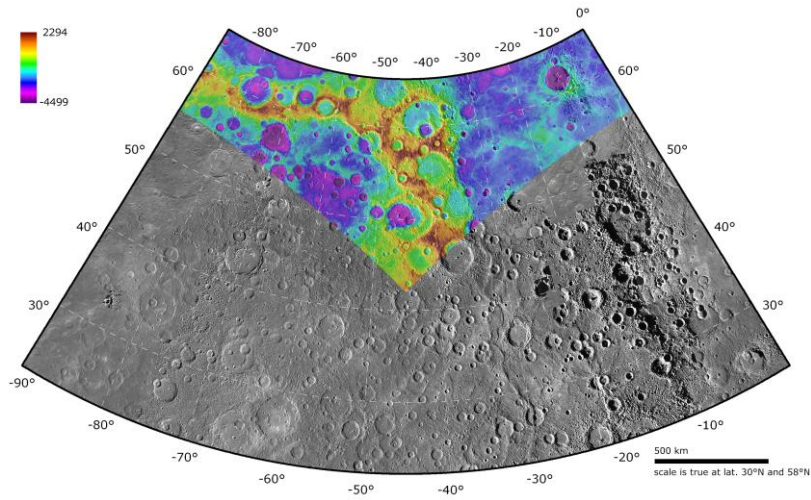


Figure 2.22. MLA topography at 500 mpp available for the North pole, trimmed to H2 quadrangle.

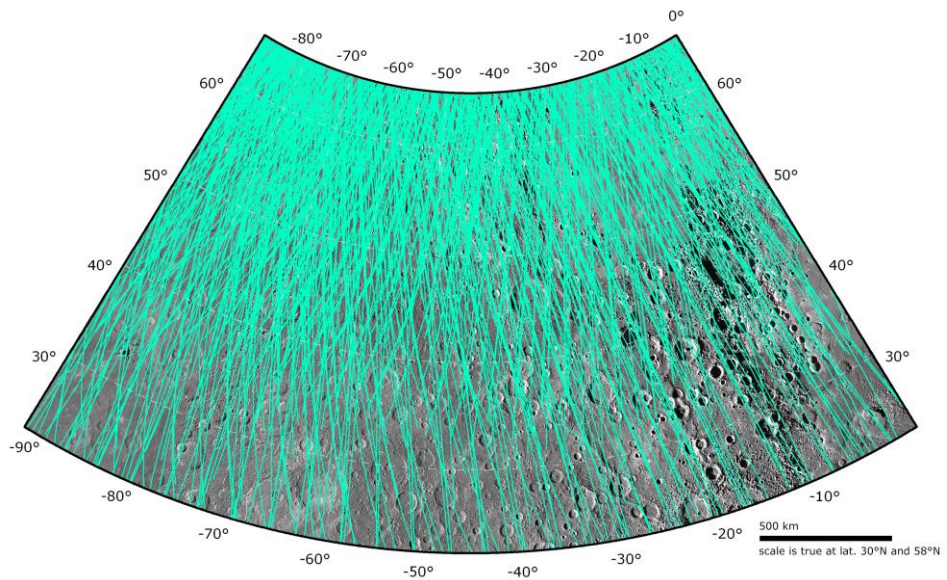


Figure 2.23. MLA track footprints on H2 quadrangle, the less dense area to the South explains the fuzzy appearance shown in figure 2.21. See an example in figure 2.24.

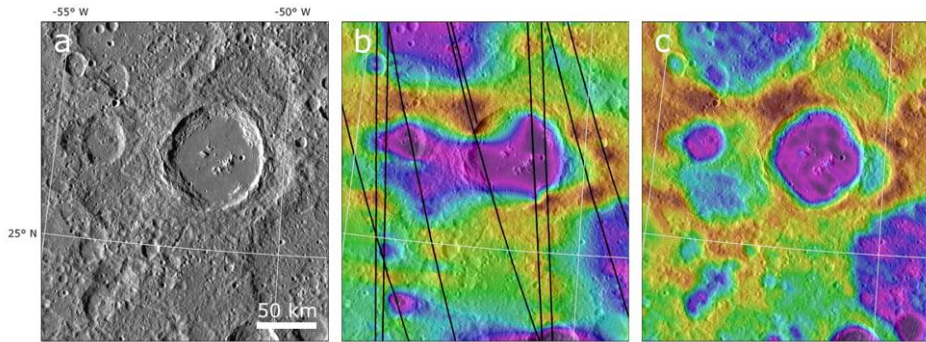


Figure 2.24. Image of the area south of Kuan Han-Ch'ing Crater (subdued crater to the north) and comparison between MLA topography and DLR stereo-topography. a) BDR basemap (166 mpp). b) MLA topography (50% transparency on BDR); the black lines represent MLA track footprints. Note the elongated E-W depression caused by the interpolation between wide-spaced MLA data. c) DLR stereo-topography of the same area (50% transparency on BDR); in this case the young crater at the center of the image is clearly visible with topography.

3. Methods

The methods used in this thesis are threefold: a) GIS mapping; b) structural analysis; c) chronology analysis. Both the structural and the chronology analyses depend on the GIS final product, thus its related methods will be analysed first.

Briefly, the following software and add-ons were used:

- 1) ESRI ArcGIS v10;
- 2) Tools for Graphics and Shapes add-on for ArcMap (Jenness, 2011);
- 3) CraterTools add-on for ArcMap (Kneissl *et al.*, 2011);
- 4) CraterStats2 software (Freie Universität Berlin, see Michael & Neukum, 2010).

While methods presented for mapping and chronology follow known rules and recommendations, the method for quantitative fault kinematic analysis presented in chapter 3.2 is new (Galluzzi *et al.*, 2015).

3.1. H2 geologic mapping

The cartographic methods used to map Victoria quadrangle must be illustrated both from a technical and a conceptual point of view. Firstly, the technical organisation of the workflow is fundamental to obtain a clean output; it includes the choice of a mapping scale, the vector layers to use and the finalisation of the whole work (*e.g.* error check, unit polygon creation). Secondly, the conceptual choice of the elements to map is also important but it is strongly affected by issues encountered during the mapping process. An example is given in chapter 3.1.2, where the crater material classification chosen for this work is explained.

3.1.1. GIS workflow

As seen in chapter 2.2, the chosen basemaps use a LCC projection on a “Mercury 2010” *datum*. This projection was used for all the layers inside the GIS project. The final map

output presented in the attached plate, has a scale of 1:3.000.000 and is the result of choices presented below.

Mapping scale

A common rule that is used for choosing the mapping scale was defined by the cartographer Waldo Tobler (Tobler, 1987):

$$S_m = R_r \times 2000 \quad (1)$$

Where S_m is the mapping scale and R_r the raster resolution. The mapping scale, S_m is the scale at which it is recommended to draw lines. As a consequence of this rule, if the mapping of H2 quadrangle was possible using the H2-Bm-0 basemap (*i.e.* BDR mosaic) alone, whose resolution is 166 mpp, the suggested mapping scale would have been 1:332.000. However, as seen in chapter 2.3, H2-Bm-o could not be used alone because of its non-uniform appearance in specific areas of the quadrangle. The resolution of the most used basemaps (see Tab. 2.2), vary between 166 mpp (*i.e.* H2-Bm-0) and 500 mpp (*i.e.* H2-Bm-5) and mapping at a scale of ~1:300,000 was often inconvenient. For this reason, I considered an intermediate resolution of 300 mpp, instead of the nominal basemaps resolution, which lead to an average mapping scale of 1:600,000, based on equation (1). On this basis, the final output scale was chosen following the USGS recommendations (Tanaka *et al.*, 2011). USGS recommends to map at a scale 2 to 5 times larger than the final print output. As a consequence, the minimum final output scale can be chosen on the basis of the map scale used for digitizing:

$$S_{o_n} = S_m \times n \quad (2)$$

Where S_{o_n} is the output scale recommended when digitizing at a scale n times larger than the output. To obtain a clean result, with round-looking lines and no visible vertex edges, I preferred to consider a scale 5 times larger than the final output scale. Thus, even though the arbitrary mapping scale chosen for digitizing this work (*i.e.* 1:600,000) permitted to obtain an output scale up to 1:1,200,000, I chose an output scale of 1:3,000,000.

Geodatabase structure and line drawing

The vector layers (*i.e. feature classes*) used for digitizing were organized into a GIS geodatabase, following most of the USGS recommendations and known structures. In particular, I used three main feature classes: 1) geologic contacts (*i.e. polyline layer*); 2) linear features (*i.e. polyline layer*); 3) surface features (*i.e. polygon layer*). A summary scheme of this structure is shown in figure 3.1.

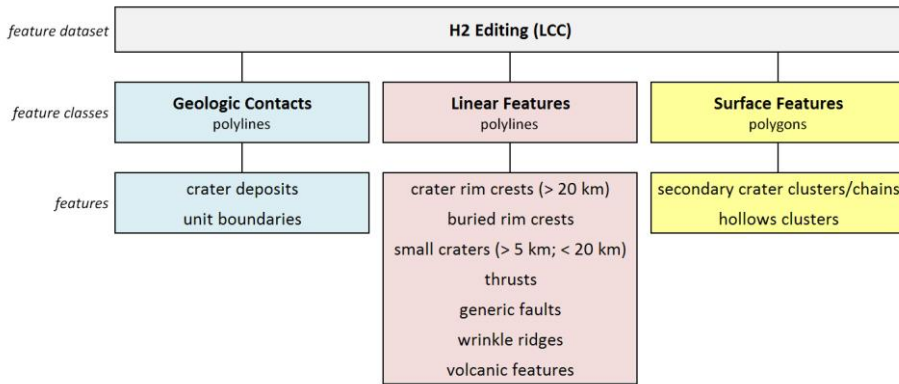


Figure 3.1. This scheme represents the overall organisation of the editing feature dataset used for mapping H2 quadrangle (see text for details).

Geologic contacts (GC) define the boundaries among the various geologic provinces and crater material classes and constitute the main digitizing layer since they have to be converted to polygons during map finalisation. USGS standards usually consider *certain*, *approximate*, *concealed* and *inferred* contacts. For this work, the digitizing scale and the non-uniformity of the basemap layers suggested the use only two kind of contacts: a) *certain*, when there is a clear and sharp contrast between different terrain textures or morphologies; b) *approximate*, when there is an uncertain, unclear or gradational transition between different terrains (Tab. 3.1 and Fig. 3.2). In the case of crater materials (*e.g.* continuous ejecta), an *approximate* contact was used even when the boundary was inferred from topography instead of the basemaps (*e.g.* Fig. 3.2c).

Table 3.1. "Geologic contacts", polyline feature class structure.

Type	Description
certain	certain boundaries
approximate	uncertain, gradational or inferred boundaries

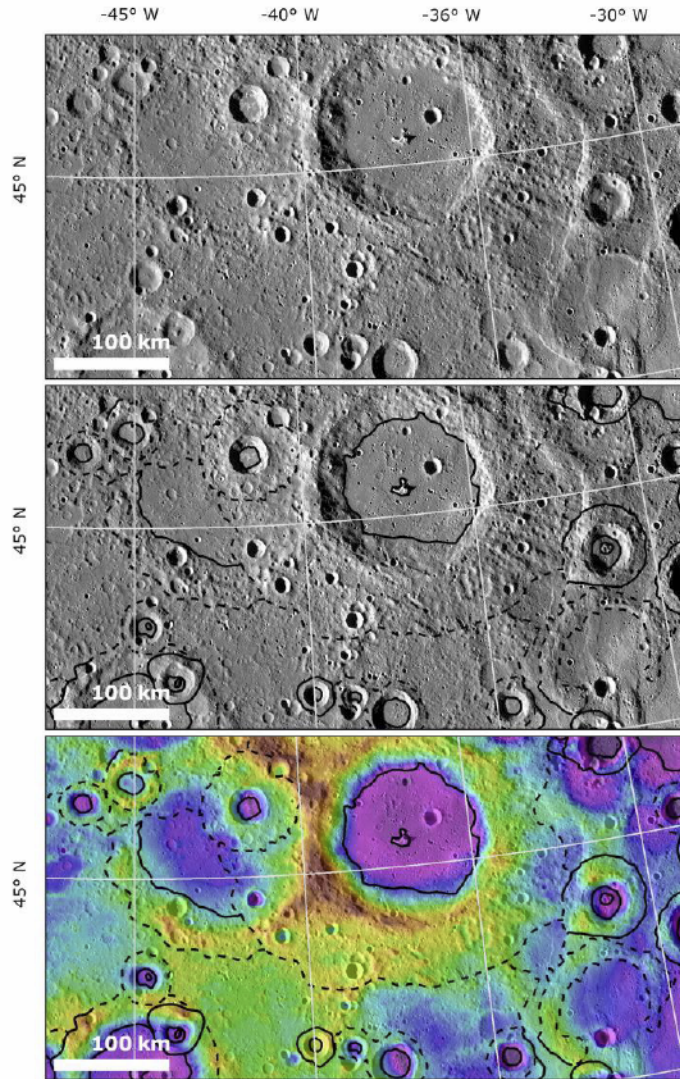


Figure 3.2. Example of a GC linework. (a) H2-Bm-0 basemap (see chapter 2.3). (b) Certain GC (solid lines) and approximate GC (dashed lines) digitized on crater material boundaries. (c) MLA topography showing that some of the approximate contacts follow topographic relief. Colour coding is scaled to the view extent, being brown and violet the highest and lowest areas, respectively.

Linear features (LF) represent morphostructural features such as faults, wrinkle ridges, crater rim crests and volcanic features. A complete list with the feature types used for this feature class is shown in table 3.2.

Table 3.2. "Linear features", polyline feature class structure.

Type	Description
crest of crater rim	rim crests of craters > 20 km
crest of buried crater	rim crests of buried craters
small crater rim	rim crests of craters > 5 km and < 20 km
thrust, certain	certain lobate scarp or high relief ridge
thrust, approximate	uncertain lobate scarp or high relief ridge
fault, certain	certain contractional fault
fault, approximate	uncertain contractional fault
wrinkle ridge	evident bend inside smooth plains
irregular pit	irregular and rimless pit

Faults have been divided into two categories: a) thrusts and b) contractional faults. Both these categories were divided into *certain* and *approximate* based on similar considerations made for the GC feature class. Common morphologies such as lobate scarps and high relief ridges were mapped as thrusts. Since Mercury abounds in contractional features (*e.g.* Byrne *et al.*, 2014), the "contractional fault" category was assigned to all those contractional structures whose morphology did not present important or evident break-in-slopes (*e.g.* Fig. 3.3).

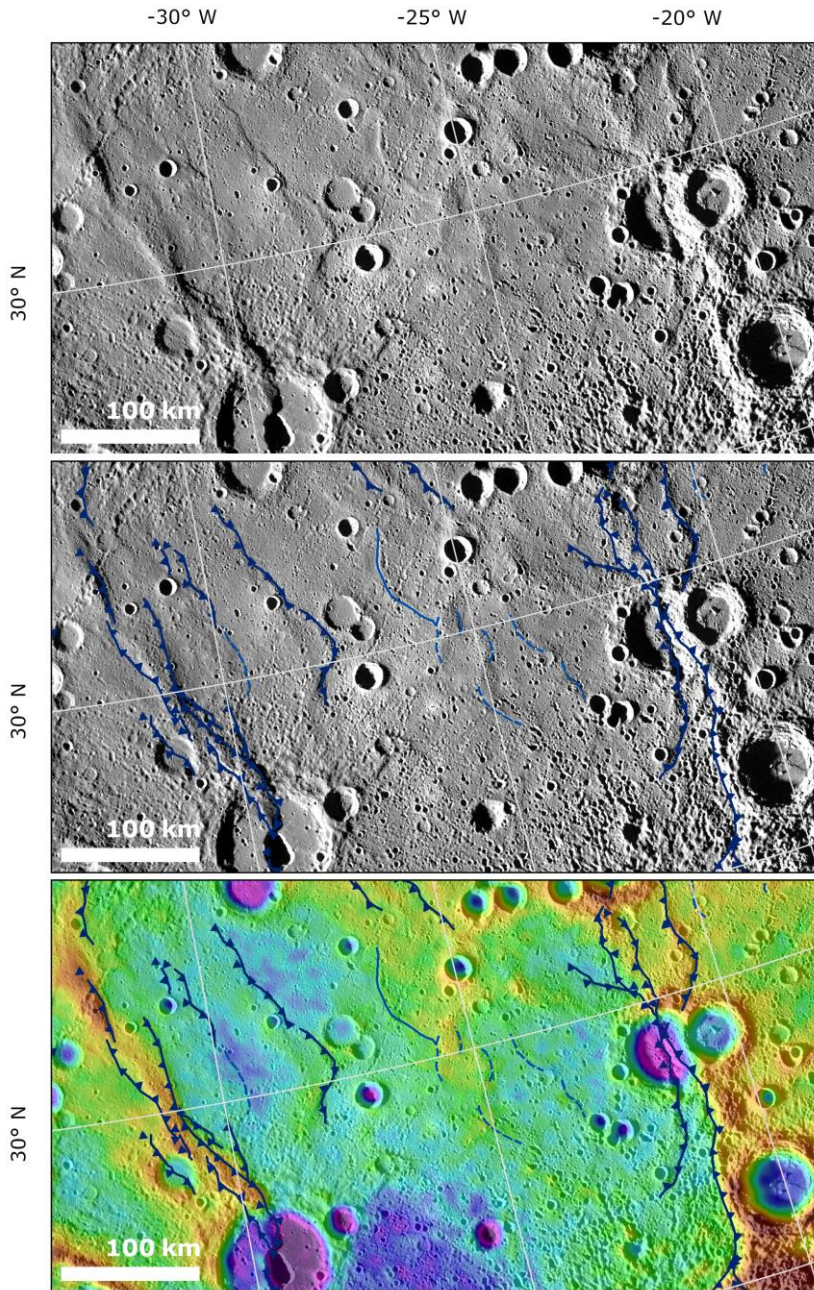


Figure 3.3. Example of a LF linework for faults in the area East of Antoniadi Dorsum. (a) H2-Bm-0 basemap (see chapter 2.3). (b) Certain thrusts (solid blue lines with triangles), certain generic contractional faults (solid light blue lines) and approximate generic faults (dashed light blue lines). (c) DLR stereo-topography (Preusker *et al.*, 2011) showing that some faults follow topographic relief. Colour coding is scaled to the view extent, being brown and violet the highest and lowest areas, respectively.

Wrinkle ridges could be considered a “contractional feature” like those described above, but they were mapped separately as they are a typical feature found inside smooth plains. Craters have different symbology depending on their size (Fig. 3.4). Craters > 20 km were mapped as standard craters, thus they are always associated with a GC defining their material boundaries (*e.g.* ejecta, central peaks). Their symbology shows ornamental ticks facing the steep inner scarp (see Fig. 3.4c). Craters ranging from 5 to 20 km were classified as “small craters”, thus they were not associated with any GC defining their deposits. The “buried crater” symbology was assigned to those craters (either in whole or in part), whose rim crest is still visible but clearly or presumably covered by other superposed crater deposits (*e.g.* Fig. 3.4c).

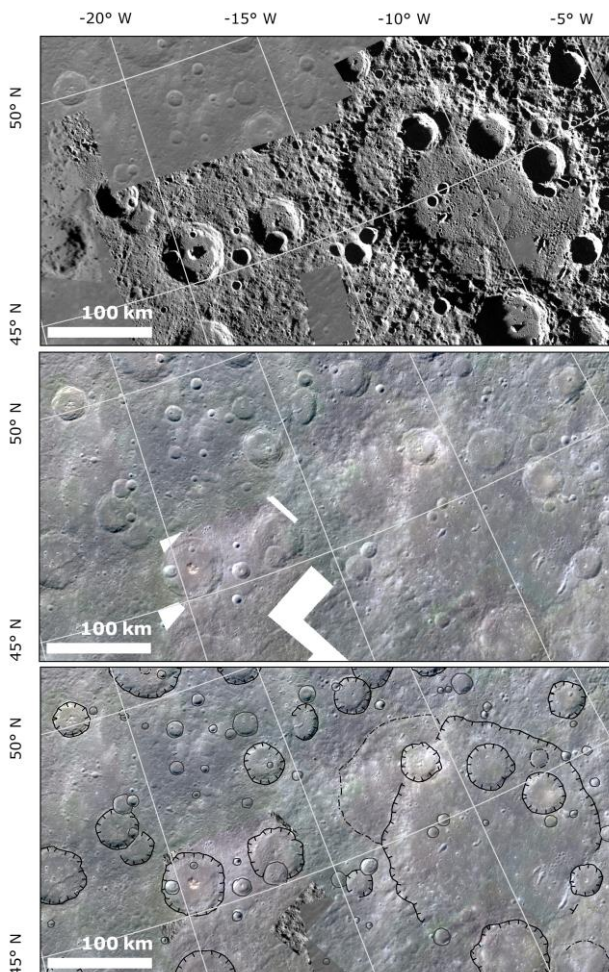


Figure 3.4. Cratered area on eastern H2. (a) H2-Bm-2 basemap (see chapter 2.3) showing high shadow contrasts that help localizing craters. (b) H2-Bm-8 basemap (see chapter 2.3) showing a lower incidence angle, some craters are not visible. (c) LF for craters > 20 km (black lines with inner ticks), > 5 km and < 20 km (grey lines) and a buried crater (black dash and dot line). H2-Bm-8 was used in the background to highlight the LF layer.

Surface features (SF) include secondary crater clusters and chains, and a limited number of clusters of hollows (see chapter 4.1 for explanation). These features were represented with textures overlaying the main units (see Tab. 3.3).

Table 3.3. "Surface features", polygon feature class structure.

Type	Description
secondary craters	secondary crater chains or clusters
hollow cluster	cluster of hollows > 6 km

As a general rule, I avoided digitizing outcrops (*e.g.* central peaks) that would have been less than 2 mm wide at the output scale (*i.e.* 6 km wide outcrops) as suggested by USGS recommendations (Tanaka *et al.*, 2011). This rule was not applied to "small craters" lower limit (*i.e.* 5 km, see Tab. 3.2), since they were useful for crater counting statistics (see chapters 3.3 and 4.3).

Map finalisation









Once the digitizing process was finished, topological rules were applied to the GC feature class, since it is the fundamental layer from which unit polygons were built. I used the three main rules explained below.

- 1) *Must not have dangles*: this is the most important rule. Before building polygons it is important that each line closes the contact against other lines (*i.e.* the final vertex of a line must stand exactly on another vertex of another line).
- 2) *Must not intersect*: this rule searches for intersecting and overlapping lines.
- 3) *Must not self-intersect*: this rule is very similar to rule 2), checking self-intersecting and self-overlapping lines.

Topology rules help finding errors, thus once they are corrected, attribute-empty polygons can be built. I associated the unit attributes shown in table 3.4 to each polygon with a point feature class. Then, I checked polygons one by one to search for discrepancies and errors that cannot be found with topology rules (*e.g.* wrong boundaries and superposition issues). This meant changing the GC feature class when necessary, re-checking topology errors and re-building corrected polygons, this time

with joined attribute points (*e.g.* using the spatial “Join” command in ArcGIS). The process of correcting and re-building polygons was repeated several times until the map was considered fully corrected and completed.

Table 3.4. Unit attribute labels and colours.

Label	Unit	Symbology
sm	Smooth Plains	
imp	Intermediate Plains	
icp	Intercrater Plains	
c3	fresh crater deposits	
c2	intermediate crater deposits	
c1	subdued crater deposits	
cfs	smooth crater floor	
cfh	hummocky crater floor	

3.1.2. Crater material classification

As shown in table 3.4, I decided to distinguish three crater classes instead of five as done in the past (McCauley *et al.*, 1981). This simplification in the classification of crater deposits was motivated by the following considerations.

The past classification was based on a study made on 40% of the planet covered by M10 frames. Even though previous cartographers used images with a lower resolution, they had the chance to make the geologic maps on a more uniform reference layer (*i.e.* the shaded relief map) that permitted them to classify craters analysing consistent images. However, the past morphological classification led to some problems as already stated in chapter 1.3.2. Spudis & Guest (1988) note that “Spudis & Prosser (1984) suggested that the stratigraphic significance of crater degradation is only approximate and that a variety of evidence, including regional geologic setting, proximity to other units, crater density, and type of post-crater modification, must be used in concert to establish the relative age of Mercurian features” and conclude that “[...] no scheme can be applied with rigorous consistency until all of Mercury is imaged at different lighting angles”. Now that MESSENGER has imaged the whole planet at a better resolution, no official updates to the past crater morphological classification have yet been made. The classification of craters requires an accurate morphometric analysis of a significant number of craters scattered through the surface of Mercury. This was not the main aim of this thesis, which, on the contrary, is centred on the structural analysis of a single quadrangle of the planet. Furthermore, the available H2 basemaps do not yet permit an homogeneous analysis of morphologic evidences.

Therefore, the three classes chosen here to identify crater deposits simply represent two end member cases (*i.e.* fresh C3 craters and subdued C₁ craters) and an intermediate case (*i.e.* C2 craters). Moreover, I avoided distinguishing between proximal rim ejecta and distant ejecta deposits as was done for some craters in McGill & King (1983), because this map focuses more on superposition relationships between the three classes of craters, rather than an internal diversification of deposits. For the same reason, crater floors were mapped following just their morphological characteristics, such as hummocky terrains or smooth infilling (*i.e.* the smooth infilling of crater floors was not mapped with the Smooth Plains unit symbology) as shown in table 3.4. The comparison

between the old classification and the classification of this work is presented in figure 3.5 and an example area showing all the three crater classes is shown in figure 3.6. A detailed description of the used crater classes is presented in chapter 4.1.2. On average, the conversion between USGS classification and the classification of this work can be summarized as follows: USGS-C5 and USGS-C4 craters were re-classified as C3 craters; USGS-C3 craters were reclassified as C2 craters; USGS-C2 craters were re-classified either as C2 or C1 craters; most of the USGS-C1 craters were left unchanged to C1 class.

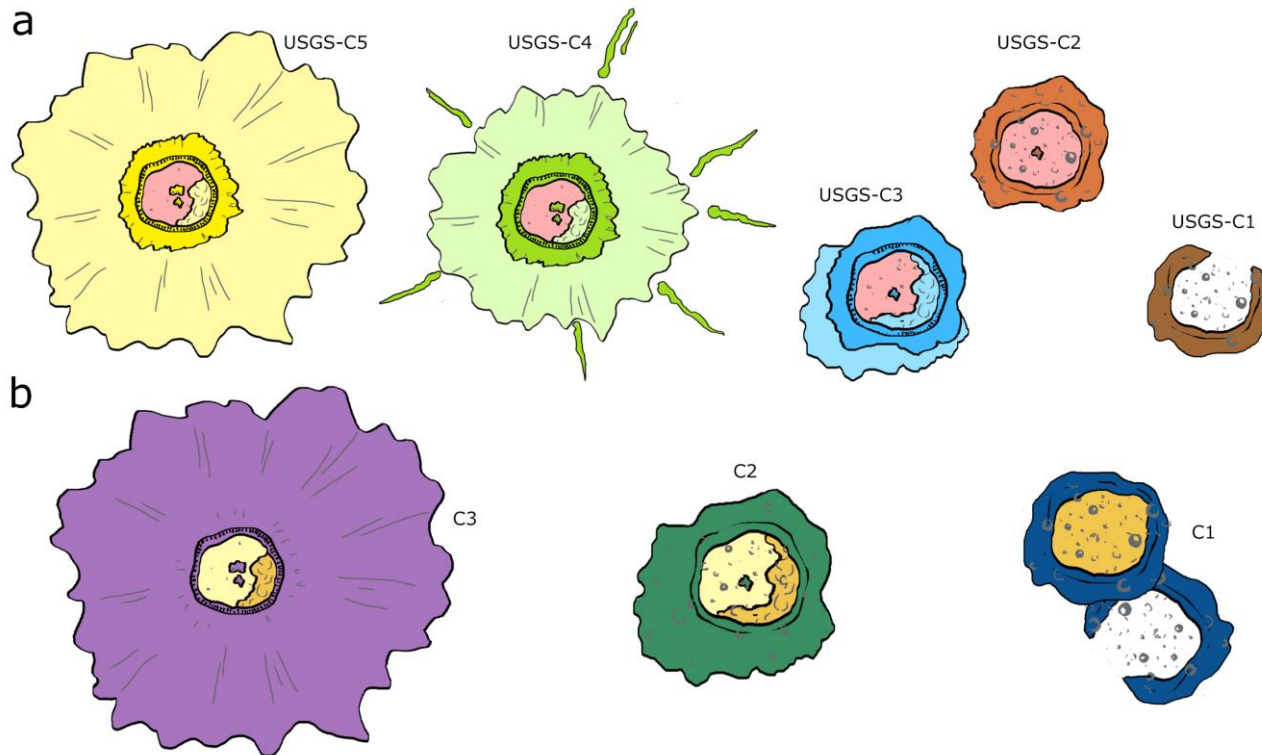


Figure 3.5. Schematic representation of crater classes, numbers decrease with increasing degradation. (a) USGS classification (see chapter 1.3.2): USGS-C5 (yellow), USGS-C4 (green), USGS-C3 (cyan), USGS-C2 (orange) and USGS-C1 (brown). Lighter hues indicate floor and radial ejecta material related to the same crater class, smooth floors are indicated by the Smooth Plains unit in pink (see McGill & King, 1983). (b) Simplified classification used in this work: C3 (violet), C2 (green), C1 (blue). Crater floors use different colours based on their morphology: hummocky crater floor (light orange), smooth crater infilling (beige). Approximately, USGS-C5 and USGS-C4 correspond to C3, USGS-C3 corresponds to C2, USGS-C2 corresponds either to C2 or C1, USGS-C1 correspond to C1.

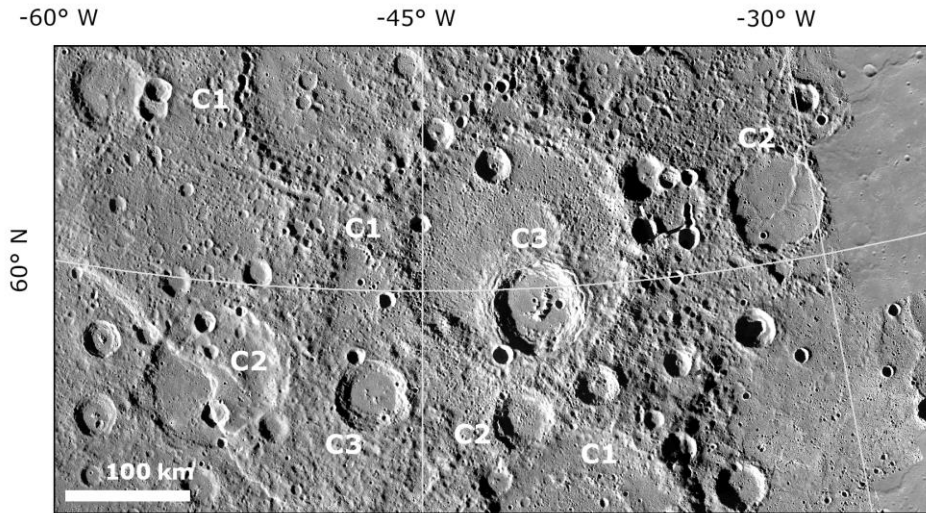


Figure 3.6. Northern H2 area showing a large variety of craters with their corresponding classification used in this work, indicated next to their rim.

The classification presented here is not intended as a new proposal for classifying craters, but rather as a simplification of the past classification to avoid most of the issues found by past authors. In this quadrangle, this simplified classification was used because it was sufficient to reach the main goal of the thesis. Each crater has an independent polygon for its deposits, thus they can be easily re-classified in the future, if an agreed updated classification scheme becomes available.

3.2. Kinematic analysis

The following paragraphs are an updated extract from the paper published during my PhD project (Galluzzi *et al.*, 2015). The described method to analyse fault kinematics was applied on the portion of Mercury covered by DLR stereo-topography (Preusker *et al.*, 2011), which was the best topography available to the public until MESSENGER Release 11, when the MLA topography of the northern hemisphere at 665 mpp and 500 mpp was released. Nonetheless, considering the MLA track coverage issues described in chapter 2.5 (see Fig. 2.24), the stereo-topography still represents a good layer to work with.

Despite the lack of direct observational data, several surface features have been positively recognized as faults on most of the terrestrial planets and satellites since the beginning of planetary exploration (*e.g.* lobate scarps, Strom *et al.*, 1975, or wrinkle ridges, Plescia & Golombek, 1986). The geometry and kinematics of these faults have hitherto been interpreted solely based on visible imagery, radar, and topographic data. On Earth, the typical constraints that can be collected in the field to characterize fault kinematics are offset markers and kinematic indicators on fault surfaces such as slickenside *striae* and steps. In the case of remotely sensed structures, like Earth's seafloor faults or faults on other planets, satellites, and minor bodies, however, markers of known pre-dislocation geometry are required to assess the fault kinematics.

Craters have been found to be an excellent deformation marker on planetary surfaces, both for kinematics and strain analysis (Strom *et al.*, 1975; Thomas & Allemand, 1993; Watters, 1993; Golombek *et al.*, 1996; Watters *et al.*, 1998; Pappalardo & Collins, 2005). Previous studies measured the change in shape of originally circular craters to estimate the strain of intensely deformed areas of Mars and Ganymede, especially in extensional provinces characterized by horst and graben systems (Thomas & Allemand, 1993; Golombek *et al.*, 1996; Pappalardo & Collins, 2005). At these locations, craters are often pervasively faulted and thus it is difficult to reconstruct their original shape. On the other hand, in some cases craters are cross-cut by single faults, and this offers an opportunity to better elucidate the fault kinematics. Previous studies analysed craters shortened by structures such as lobate scarps or high relief ridges on Mercury and Mars to characterize thrusts and reverse faults, respectively (*e.g.* Strom *et al.*, 1975; Watters,

1993; Watters *et al.*, 1998). However, these studies relied on *a priori* assumptions on fault geometry and kinematics (*i.e.* the fault true dip angle and the slip vector).

The fault dip is a basic item of information to constrain fault kinematics and it is strongly dependent on the physical properties of the rock. For example, fault dip angle is required to estimate the amount of displacement and to calculate the displacement – length ratio (γ , Cowie & Scholz, 1992) for faults on planetary surfaces (Watters *et al.*, 1998, 2000; Watters, 2003; Watters & Nimmo, 2010; Byrne *et al.*, 2014). Hitherto, fault dip angles of structures that accommodated shortening on Mars and Mercury have been always assumed to be in the range of 25–35°, based on the results of mechanical models (Schultz & Watters, 2001; Watters *et al.*, 2002). These models assume a pure dip-slip motion for thrusts and normal faults. In most real cases, however, slip may have a significant oblique component. Additionally, the slip direction may change along faults with a non-planar surface (*e.g.* Roberts, 1996), as recurrently observed on low-angle dipping faults. All these complications require an effort to constrain the fault actual slip direction and true dip angle.

3.2.1. Fault parameters

The parameters that define fault geometry and kinematics are the attitude of the fault plane and of the slip line that lies on the fault plane. The azimuth of the line defined by the intersection between the fault plane and the horizontal plane is commonly known as the fault strike, and the azimuth of the horizontal projection of the slip line is called slip trend. The fault dip is measured perpendicularly to the fault strike, and the dip of the slip line is called the slip plunge (Fig. 3.7a). In addition to azimuths and dips, the rake angle, which is the angle between the fault strike and the slip line within the fault plane, is of great importance for defining fault kinematics. The relative block motion across a fault usually lies somewhere between two end-member cases: strike-slip and dip-slip. In strike-slip motion, blocks move along the fault strike (rake is 0°), while in dip-slip motion they move along the dip direction (rake is 90°). When the motion on the fault is neither pure strike-slip nor pure dip-slip, it is generally called oblique-slip (rake is between 0° and 90°, Fig. 3.7a). Therefore, knowing these parameters, it is important to represent the fault displacement as a vector (*i.e.* slip vector, Fig. 3.7b), whose direction and dip are defined by the slip trend and plunge, respectively. Finally, the vector

magnitude can be calculated from the horizontal and vertical component of displacement, which can be estimated using reference markers, whose position prior to faulting is known (Fig. 3.7b).

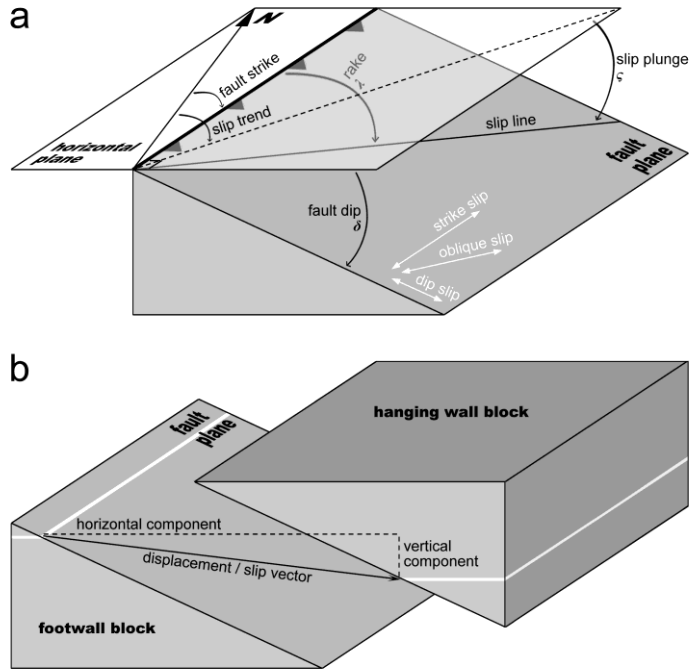


Figure 3.7. Block diagram of a generic fault plane (Galluzzi *et al.*, 2015), redrawn and modified from Allmendinger *et al.* (2011) and Twiss & Moores (2007). (a) Representation of the main angles defining a fault. On the fault plane, the three types of slip motion are represented by the white arrows near the bottom left corner. The oblique black line represents a generic slip line as an example of oblique-slip motion. On the horizontal plane, three lines are indicated as follows: the arrowed line is the North direction, from which azimuths (*i.e.* strike and trend) can be measured; the bold line is the intersection between the fault plane and the horizontal plane (*i.e.* fault strike); the dashed line is the horizontal projection of the slip line (*i.e.* slip trend). The slip plunge, ζ is measured as the tilt angle of the slip line with respect to the horizontal plane. Notice that the fault dip, δ can be measured solely at right angle to the fault strike, while the fault rake, λ can be measured only onto the fault plane. (b) Representation of the slip vector or fault displacement. The vector orientation and tilt are the slip trend and plunge respectively, already defined by the block diagram in (a). If a recognisable reference feature is present (white dislocated layer), the vector magnitude can be estimated and decomposed into its horizontal and vertical components (dashed lines).

3.2.2. Faulted craters as kinematic indicators

The method presented here uses craters as displacement markers to obtain quantitative geometric and kinematic parameters of the cross-cutting faults, such as true slip direction, horizontal and vertical components of displacement and thus the fault true dip and displacement magnitude. The parameters obtained from craters were used to estimate the fault rake and to quantitatively constrain its kinematics.

Craters can be used for measuring fault dislocation, assuming that the original outline of their rim was almost perfectly circular prior to deformation. As Kenkmann *et al.* (2014) remark in a recent overview of the geometries of impact craters, regardless of the magnitude of the gravitational field, the most probable impact angle for all planetary bodies is 45° (Gilbert, 1893; Shoemaker, 1962), but only impact angles below $10\text{--}15^\circ$ can generate a non-circular shape (Gault & Wedekind, 1978; Bottke *et al.*, 2000). This is probably the case of Sveinsdottir Crater, cross-cut by Beagle Rupes on Mercury (Fig. 3.8).

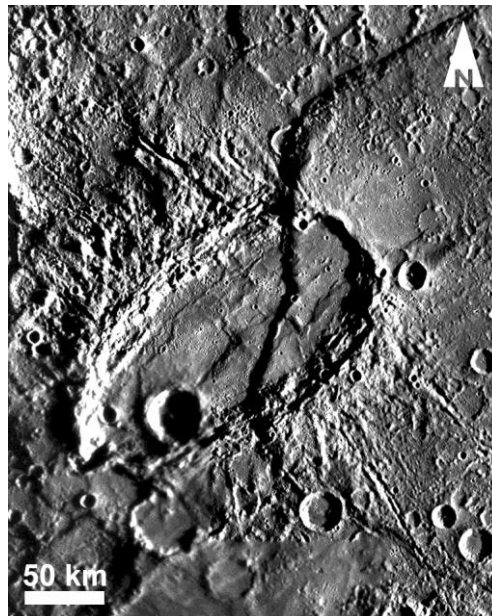


Figure 3.8. MDIS flyby 500 mpp mosaic (Becker *et al.*, 2009) showing Sveinsdottir crater cross-cut by Beagle Rupes on Mercury (100.5°E ; 2.5°S). The elongated shape of this crater is widely accepted as having been caused by an oblique impact.

Since this method aims at estimating fault geometry and kinematics, I consider only craters cross-cut by a single fault. Furthermore, I assume that a crater was rigidly deformed and its shape was extended or shortened uniquely due to faulting; erosion or different post-deformation processes are not taken into account. The choice of a suitable spatial reference frame for the basemaps is fundamental in order to analyse faulted craters. As stated in chapter 2.1, a stereographic projection centred on each analysed crater is the best compromise for evaluating the crater shape, because it does not introduce significant distortions around the projection centre (see also Kneissl *et al.*, 2010).

With the exclusion of pure strike-slip faults (lack of vertical throw component), one part of the crater will be raised and the other lowered due to faulting. Even if the nature of the fault is completely unknown, the hanging wall or footwall would be still identified based on the fault dip direction reconstructed from the analysis of the deformed crater. If the rim was rigidly displaced, one should expect to see an offset along the strike of the fault between the raised and the lowered parts of the rim (*e.g.* Figs. 3.9a and 3.9b). However, the crater rim will seldom look like a perfectly cut and displaced circle (*e.g.* Figs. 3.9c and 3.9d), thus a work-around to study the displacement effects is needed using the graphical method described below.

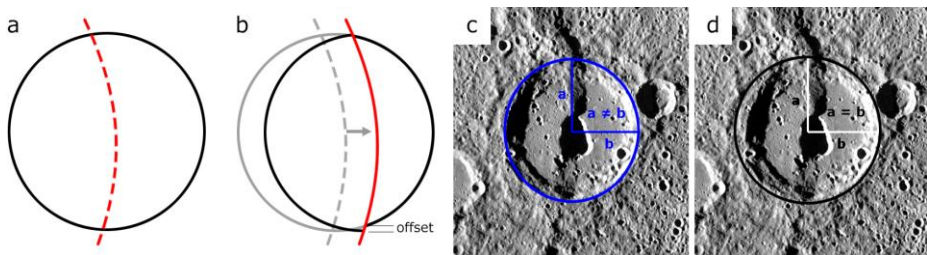


Figure 3.9. Comparison between an ideal and a real faulted crater. (a) Pristine circular shape; the red dashed line represents the developing fault. (b) Circular shape displaced by the fault (red line); the grey circle represents the pristine circular shape; the dashed grey line represents the pre-shift location of the fault shown in (a). A small offset is visible along the fault strike at the bottom of the image. (c) MDIS BDR basemap showing Geddes crater on Antoniadi Dorsum in stereographic projection centered on the crater center (-29.7°E ; 27.19°N), the crater diameter is ~ 83 km. The blue ellipse marks the crater rim shortened by the lobate scarp, but no offset is visible due to rim complex morphology and raster resolution. (d) The ideal circle that should fit the pristine crater. It fits the right (illuminated) side, but does not fit the left side (in shadow).

3.2.3. Measuring fault slip components

The first step aims at measuring the fault horizontal and vertical components of slip, Δx and Δh , respectively (Fig. 3.10). To obtain Δx , a circle is drawn as the best fit of the rim portion on one side of the faulted crater. In Figure 3.10b and 3.10c, the pink circle is assumed to represent the pre-dislocation reference shape of the originally circular crater; because of fault dislocation, it will not fit the crater rim on the opposite side of the fault (the uplifted rim). To draw the circle, I used a graphic layer then converted to a shapefile layer in stereographic projection centred on the crater. Alternatively, the “three-points” construction tool of the ArcGIS add-on “CraterTools” by Kneissl *et al.* (2011) can be used. The unfitted part of the rim will consequently be either outside or inside the circle; if outside, it can be stated that the crater was extended by a normal fault, whereas, if inside, the crater was shortened by a reverse fault (*e.g.* Figs. 3.9 and 3.10). In the case of a pure strike-slip fault, half the unfitted part of the rim will lie inside the circle and half will lie outside. These are end-member cases for pure dip- and strike-slip faults, however all the intermediate cases (*i.e.* oblique-slip faults) are possible and their analysis is based on the following steps.

The horizontal component of slip, Δx is found by shifting a copy of the previously drawn circle until it fits the rim on the opposite side of the fault (yellow circle in Fig. 3.10b and 3.10c). It is recommended to always use the same criterion while fitting the circles, for example fitting the circles either on the highest part of the rim or on the break-in-slope just next to the crater floor. After the two circles are built, the distance between their centres, Δx , corresponds to the horizontal translation caused by the fault. To minimize errors caused by the projection, I prefer to measure Δx using the spheroidal length calculator in “Tools for Graphics and Shapes” by Jenness (2011). Once Δx is measured, the rough fault kinematics parameters are already defined, since the trend of Δx segment corresponds to the slip trend (Fig. 3.10c).

To obtain the vertical component of slip, Δh , which is usually estimated using the fault scarp height (*e.g.* Watters *et al.*, 1998), the use of a DTM is required. If the crater diameter is smaller than the fault length and its rim is far from the fault tips, where a lesser amount of slip is expected (*e.g.* Kim & Sanderson, 2005), it is possible to assume that the rigid deformation caused by faulting produces an elevation difference between

the two displaced crater parts that corresponds to the fault vertical displacement. To have a better control on Δh , it is better to measure elevation at the crater floor and also at the rim. In fact, craters often present morphological irregularities at their floor like central peaks, peak rings, and topographic variations; therefore the measure of Δh on the rim sometimes offers a more accurate estimate. The measure assumes that the displaced sides of the crater rim were initially at the same elevation before faulting, a condition which is met if the regional pre-impact slope was either very low or negligible across the crater area, and if the crater was not tilted prior to tectonic deformation.

Under the latter assumptions, Δh is obtained by making a series of profiles across the crater based on the available DTM. Regardless of the direction chosen to draw the profiles, after a rigid displacement the crater would have virtually the same difference in elevation across the two faulted blocks within its perimeter. Drawing a profile perpendicular to the fault is routine in structural analysis to characterize the architecture of faulted regions; however, since this method starts measuring the components of the slip, it is preferable to draw profiles parallel to Δx direction (Fig. 3.10d), which is perpendicular to the fault trace only in the case of dip-slip motion. The value of Δh is obtained as the difference between the elevation of the raised rim and the lowered rim (Fig. 3.10e). A comparison between the values obtained at the base of the fault scarp (*i.e.* at the crater floor) and at the crater rim, when both measures are available, can help to increase accuracy in the Δh estimate.

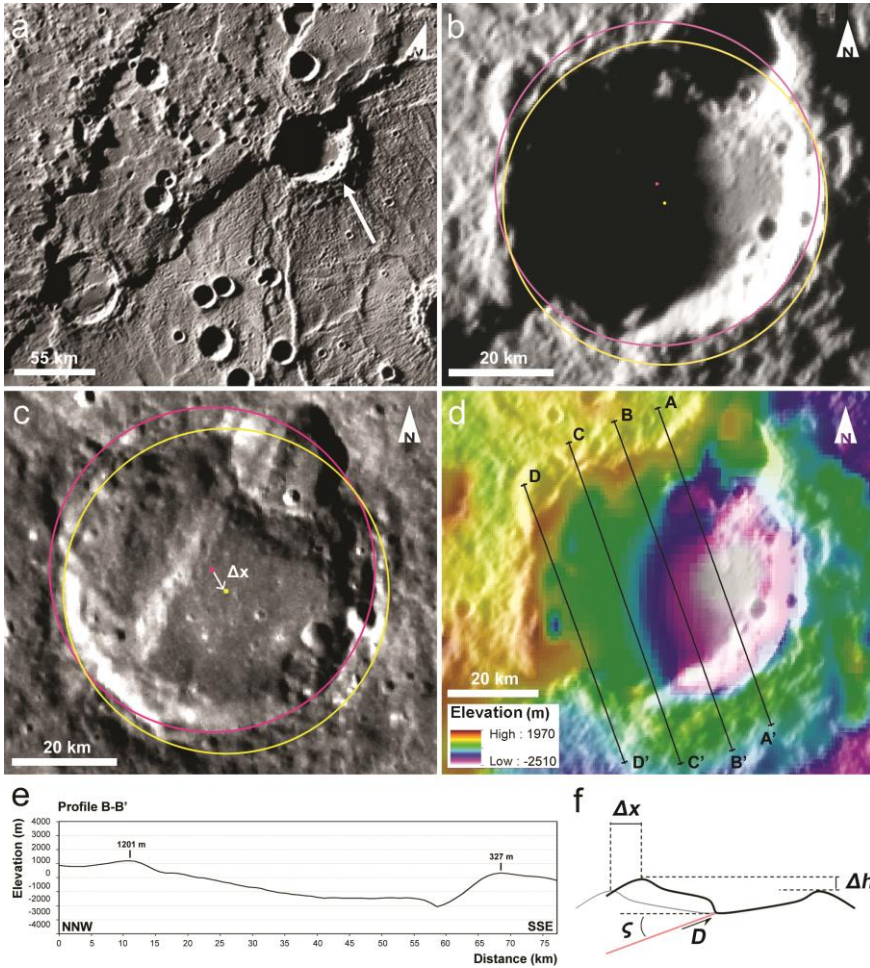


Figure 3.10. Analysis of crater 10-F (see chapter 4.2) cross-cut by Enterprise Rupes (modified from Galluzzi *et al.*, 2015). (a) MDIS flyby mosaic at 500 mpp resolution (Becker *et al.*, 2009) showing Enterprise Rupes that cross-cut the analysed crater (white arrow). (b) The same mosaic in (a) shows a long shadow that covers the fault trace but helps in drawing the circles. The yellow and pink circles fit the rim on the hanging wall and on the footwall of the thrust, respectively. The centre of each circle is represented by a dot with the same colour as the corresponding circle. (c) MDIS global mosaic at 250 mpp resolution. This specific image was chosen to show the cross-cutting fault. The white arrow connecting the two centres represents Δx and the slip trend. (d) DTM (after Preusker *et al.*, 2011) showing the vertical dislocation caused by the thrust. The black lines represent the profiles drawn parallel to the slip trend. (e) Vertically exaggerated ($\times 2$) cross-section diagram from line B-B' in (d). The elevation of the hanging wall and footwall rims is indicated. (f) 2D geometric scheme representing an example of a faulted crater along cross-section parallel to the slip direction. The reverse fault displaces the crater causing a displacement, D along the fault plane. The vertical component of the displacement, Δh is represented by the height difference between the two opposite rims. The horizontal component of the displacement, Δx is represented by the horizontal translation of the hanging wall rim from its original position. The angle between the fault and the horizontal plane is the slip plunge, ζ that is the same as the fault true dip, δ in case of dip-slip faults.

3.2.4. Estimating slip geometry and fault kinematics

Considering a planar fault surface as shown in figure 3., once both the horizontal and vertical slip components are known, the slip plunge ς and the amount of displacement D can be derived with simple plane trigonometry:

$$\varsigma = \tan^{-1}(\Delta h / \Delta x) \quad (3)$$

$$D = \Delta h / \sin \varsigma \quad (4)$$

Equation (4) was used by Watters & Nimmo (2010, and references therein) to calculate the amount of thrust displacement using an hypothesised fault dip, θ , instead of slip plunge, ς , on the assumption that all thrusts dip at 25°–30° (Schultz & Watters, 2001; Watters *et al.*, 2002). In contrast, it is possible to calculate the slip plunge, ς that, for pure dip-slip faults, matches with fault true dip, δ . As stated in the previous sections, most faults have moderate oblique-slip behaviour, for this reason angle ς will be in most cases smaller than true dip, δ (*i.e.* ς is an apparent fault dip). Despite this, the true dip of a fault, δ , can still be calculated starting from an apparent dip that is associated to a known trend, which in this case is the slip trend. Based on a commonly used relation, the true dip is:

$$\delta = \tan^{-1}(\tan \varsigma / \sin \varphi) \quad (5)$$

where φ is the angle between the fault strike and the slip trend that was measured from the Δx segment (Fig. 3.11).

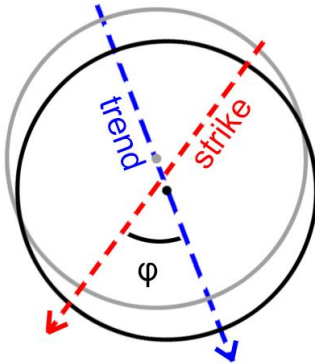


Figure 3.11. Schematic representation of the faulted crater in figure 3.10. The red dashed line represents the average fault strike (right-hand rule) within the crater area. The blue dashed line represents the slip vector trend passing by the two circle centres (black and grey dots, *i.e.* it represents the direction of the white Δx arrow in Fig. 3.10). The angle between fault strike and slip vector trend, φ , is used in equation (5) to derive fault true dip, δ .

Knowing angle φ allows also the calculation of the along-strike displacement Ds of an oblique-slip movement on a fault plane using the equation $Ds = \Delta x \cos\varphi$, as explained in Massironi *et al.* (2015). At this step the fault superficial geometry is completely known, and it is possible to proceed to investigate its kinematics. The angle between the fault strike and the slip vector measured within the fault plane is the fault rake, λ . In a three-dimensional space the angle between two lines can be calculated by resolving the dot product of the two unit vectors defined by the orientations of the lines (*e.g.* see Allmendinger *et al.*, 2011). Considering the fault strike and slip as unit vectors, the angle between them will therefore be:

$$\lambda = \cos^{-1}(f_1 s_1 + f_2 s_2 + f_3 s_3) \quad (6)$$

where f_{1-3} and s_{1-3} are the direction cosines of the fault strike unit vector and slip unit vector, respectively, considering the fault strike as a line with 0° plunge. Using equations (3) to (6) on analysable craters fully constrains the kinematics of the cross-cutting faults. Thus this method represents an innovative way of gathering quantitative kinematic data on remotely sensed faults.

3.3. Dating methods

The *absolute age* of rocks is usually determined based on the analysis of decay of radioactive isotopes. In the case of terrestrial planets, only the Apollo-returned Lunar samples could be accurately dated (Wilhelms, 1987). As implied in chapter 1.3.1 for chronology, knowledge of the Moon surface permitted the results of Lunar studies to be extended to the other terrestrial planets. Many authors assess that there is a strong evidence that the meteoritic bombardment has been somewhat uniform across the inner solar system (Neukum, 1983; Neukum & Ivanov, 1994; Strom & Neukum, 1988; Neukum *et al.*, 2001a, b), thus comparable to the lunar example, for which absolute ages are available. As a consequence, the age of remotely sensed terrains can be estimated by comparing impact crater size-frequency distributions (SFD) to planet-specific cratering rates derived from scaling laws applied to the Lunar model. Several models permit estimation of terrestrial planets absolute ages from SFDs using dedicated production functions and chronology models (*e.g.* for Mercury: Neukum, 1983; Strom & Neukum, 1988; Ivanov *et al.*, 2001; Neukum *et al.*, 2001a; Marchi *et al.*, 2009,

2011). An example of a chronology model proposed for Mercury is given by Neukum *et al.* (2001a) and is shown in figure 3.12.

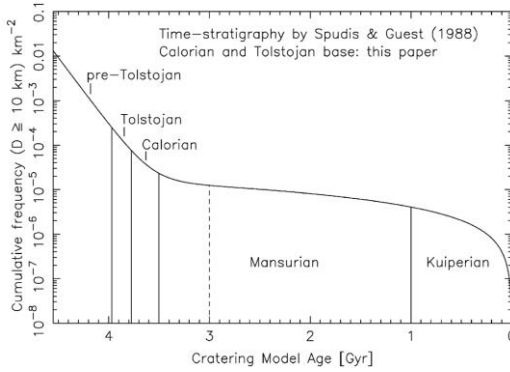


Figure 3.12. Mercury impact cratering chronology model proposed by Neukum *et al.* (2001a) and applied to Spudis & Guest (1988) chronostratigraphy.

3.3.1. Relative age determination

Since the modeled production functions rely on different principles and may give different results, in this work I present just the relative age of studied areas obtained with crater cumulative SFDs (CSFDs). A similar analysis was done also in the past by McGill & King (1983) or recently by Whitten *et al.* (2014) in their comparative study of the relative ages of intercrater and intermediate plains. Crater SFDs of planetary surfaces are a powerful tool to determine remotely-sensed units *relative age* using crater counting techniques (*e.g.* using CraterTools add on for ArcMap by Kneissl *et al.*, 2011). The main principle behind planetary relative age estimation is that the higher the number of craters per area, the older the related unit. Thus it is possible to compare CSFDs of different study areas to assess the sequence of events that formed the main geologic provinces found within Victoria quadrangle.

Cumulative size-frequency distribution

Based on the directions given by the Crater Analysis Techniques Working Group (1979), I followed the rules for building crater CSFDs:

- 1) Sort the crater diameters in ascending order ($d_1, d_2, d_3, \dots, d_n$);
- 2) Plot on log-log scale the diameter of each crater, d_n , against the total cumulative number of craters, n , per unit area, n/A , being A the counting surface area;

3) Plot the error interval, $\pm \sigma$, which is $(n \pm n^{1/2}) / A$.

The plot can be easily obtained also using Craterstats2 software (Michael & Neukum, 2010).

A quick method to directly compare the areal density of impact craters, consists in giving the value of $N(D)$, where N is the cumulative number of craters with diameter $\geq D$ [km] per 10^6 km^2 area (*e.g.* see the comparative study of Whitten *et al.*, 2014).

The crater counting results of this thesis will be therefore given both in terms of $N(D)$ and CSFDs on selected study areas. The choice of these areas will be based on the geologic mapping results presented in chapter 4.

3.3.2. Buffered crater counting

Since this thesis is aimed at studying surface structures, I adopted the linear feature dating technique proposed by Tanaka (1982), which relies on the principle that the density of impact craters superposing a linear feature, depends on the area defined by crater diameters. This method was then updated and addressed to as the “buffered crater counting” technique by Fassett & Head (2008) and it has hitherto been used principally for valley networks (Fassett & Head, 2008; Hoke & Hynek, 2009; Bouley *et al.*, 2010) or on fault systems (Giacomini *et al.*, 2015; Kneissl *et al.*, 2015).

The buffer (S_{buffer}) applied to each linear feature involved in the fault system depends on the formula:

$$S_{buffer} = 1.5 \times D + 0.5 \times W_v \quad (7)$$

Where D is the diameter of the crater and W_v the linear feature width.

The linear feature width, W_v is a useful parameter when dealing with valley networks, because it adds the valley width to the buffer area. While, in case of faults, for example, it may be related to a thrust-related antiform fold (see Giacomini *et al.*, 2015). However, in this study, I prefer not to consider this parameter, because some of the small craters were found on the crest of the antiform folds, and it was not clear whether they were actually superposing the fault (*i.e.* younger than the fault), or they were just drag on top of the fold by the thrust motion (*i.e.* older than the fault). Considering this issue, since it

is necessary to count just those craters that postdate the fault, I used the following diameter-only, constraining formula:

$$S_{\text{buffer}} = 1.5 \times D \quad (8)$$

Lowering the S_{buffer} size means taking into account a smaller counting area, which is dependent on the distance of the fault from the crater centre considering also crater continuous ejecta, whose extent is usually $1D$ from crater perimeter (Melosh, 1989).

It can be said that relation (8) is a “semi-stringent” method, when compared to the “stringent” method used by Tanaka (1982), Wichman & Schultz (1989) and lately also by Giacomini *et al.* (2015), which considers just those craters directly superposing the feature (*i.e.* without considering their ejecta).

From relations (7) and (8) it is clear that each counted crater generates its own area around the feature, thus the cumulative number of craters, N_c , will be given by the following relation:

$$N_c = \sum_{n=1}^k 1/A_n \quad (9)$$

Where A_n is the buffered area for each crater diameter, automatically calculated inside ArcMap.

Using relations (8) and (9) thus allowed me to plot the cumulative SFD of the mapped fault systems inside Victoria quadrangle.

4. Results

4.1. H2 geologic map

The geologic map available in the attached plate provides a full overview of the geologic and structural framework of the Victoria quadrangle (see Fig. 4.1 for the total digitized linework). In the following paragraphs, the elements composing the map are analysed in detail.

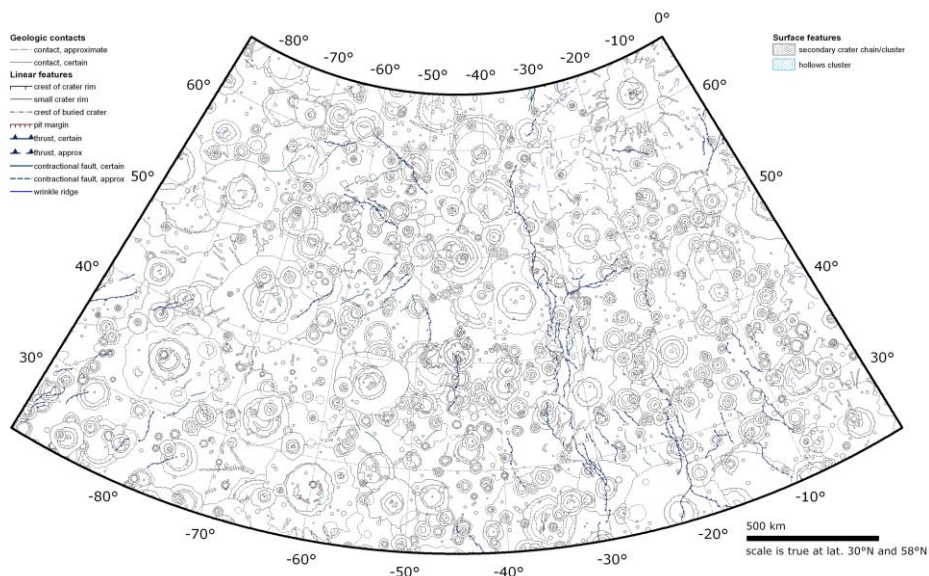


Figure 4.1. Overall linework (linear features, surface features and geologic contact) from which H2 geologic map was built.

4.1.1. Surface and linear features

Surface features encompass clusters (> 6 km) and chains of secondary craters (*i.e.* derived from primary impacts) and *hollow* fields (> 6 km). Secondaries are widespread due to the dense cratering record. Hollows are a very common feature on Mercury (*e.g.* Blewett *et al.*, 2011; Thomas *et al.*, 2014a) but few hollow clusters > 6 km could be mapped within Victoria quadrangle (*e.g.* Fig. 4.2).

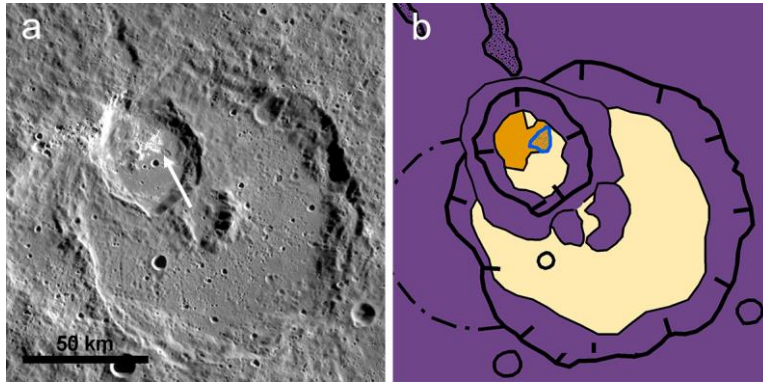


Figure 4.2. Two unnamed craters in the south-eastern corner of H2 quadrangle (smaller crater: -3.6° W; 25.6° N). The smaller and younger crater has a small hollow cluster on its floor (white arrow). (a) H2-Bm-7 basemap (200 mpp). (b) Detail of the geologic map (this work, refer to Fig 4.5 for colour legend).

The feature linework is composed of crater crests, faults and irregular pits (see tables 3.2 to 3.4) for a total of 2248 digitized linear features (Fig. 4.3). Faults, which are the main topic of this research, are discussed in detail in chapter 4.1.3.

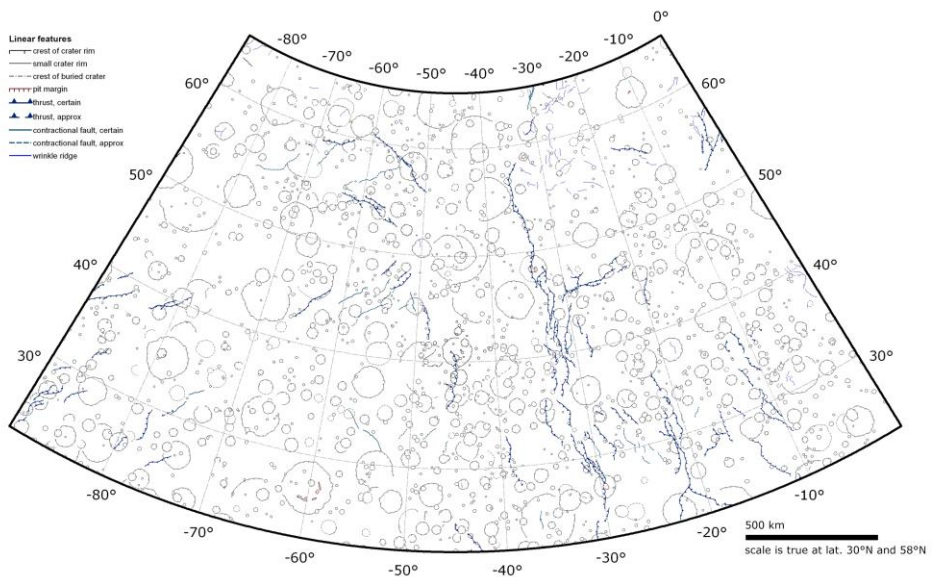


Figure 4.3. Linear features composing H2 geologic map (faults, craters and pits).

As explained in chapter 3.1.1., this map shows craters > 5 km. Using this size threshold, ~ 1750 craters were mapped in the quadrangle (Fig. 4.4); more than 500 of these craters

have a diameter > 20 km and their deposits could be mapped and classified as already explained in chapter 3.1.2. The mapped craters represent a useful record for dating techniques and their relative size–frequency distributions are presented in chapter 4.3.

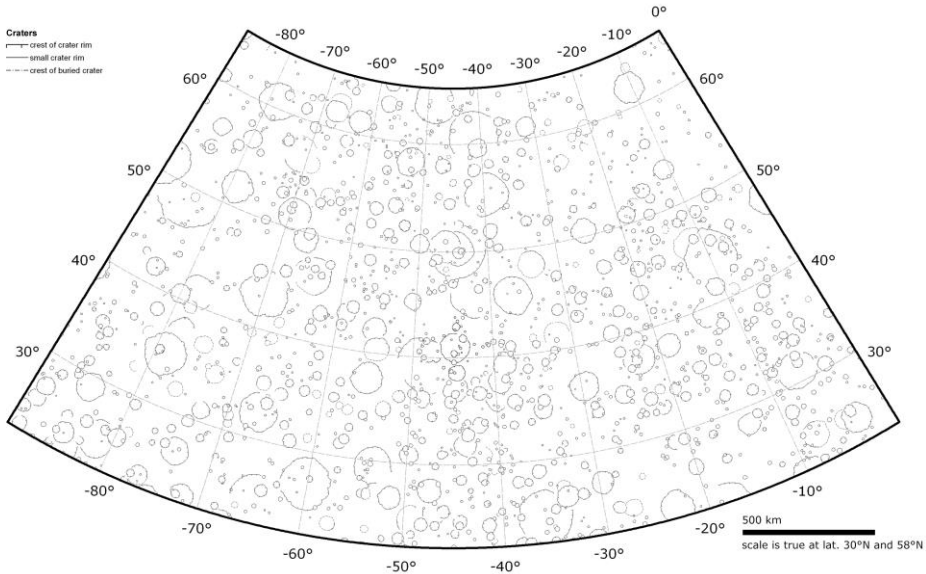


Figure 4.4. Linework for craters (> 5 km, > 20 km and buried craters) within H2 quadrangle.

Irregular pits mapped in this quadrangle are already known in literature (*e.g.* Kerber *et al.*, 2011; Goudge *et al.*, 2014; Thomas *et al.*, 2014a). H2 pits are found on crater floors only, and in particular the pit-bearing craters are: Abedin (see Thomas *et al.*, 2014a), Praxiteles, Geddes on Antoniadi Dorsum, an unnamed crater north-east of Derzhavin crater on Victoria Rupes (see Kerber *et al.*, 2011) and an unnamed crater at the north tip of Victoria Rupes (see Goudge *et al.*, 2014). Curiously, the last three pit-bearing craters are aligned along the same fault system (here called the “Victoria system”, see chapter 4.1.3). The presence of faults, in fact, is believed to be the cause of magma ascent and explosive volcanism (Thomas *et al.*, 2014b).

4.1.2. Map units

A smaller scale version of H2 geologic map is shown in figure 4.5. The geologic units characterising H2 quadrangle are those already known in literature and described in chapter 1.3.2. Below follows a brief description of main units associated with unit labels present in the attached plate.

Description of map units

- C3 C3 craters – Fresh craters with sharp rims. Well recognisable and textured ejecta blanket. Largest craters present secondary crater chains extending radially from the crater centre. These craters often have central peaks or peak rings. Crater floor is intact to poorly cratered by < 5 km craters, often presenting a smooth morphology. This class broadly corresponds to USGS–C₅ and USGS–C₄ craters (McCauley *et al.*, 1981).
- C2 C2 craters – Degraded craters with subdued but still recognisable rims. Proximal ejecta are more recognisable than distant ejecta. They may not always present a textured ejecta blanket. Central peaks and peak rings are still recognisable. Crater floor may have smooth to hummocky morphology and is more densely cratered than c3. This class approximately corresponds to USGS–C₃ to USGS–C₂ craters (McCauley *et al.*, 1981).
- C1 C1 craters – Strongly degraded craters with subdued, sometimes discontinuous rims sometimes recognisable only with the aid of topography. Largest craters (> 150 km) may still preserve recognisable proximal ejecta and internal subdued peak rings. These craters often present a hummocky and densely cratered floor. This class approximately corresponds to USGS–C₂ to USGS–C₁ craters (McCauley *et al.*, 1981).
- SCI Smooth crater infilling – Very similar to the smooth plains unit (SP), but confined to crater area.
- HCF Hummocky crater floor – Very similar to the intercrater plains unit (ICP), but confined to crater area.

- SP Smooth plains – Smooth and poorly cratered plain surfaces, superposed only by C3 craters. Their boundary is usually neat and well recognisable, defined by older crater rims, ICP reliefs or tectonic features. Older underlying craters are often recognisable as “ghost craters”. H2 SP principally correspond to the northern smooth plains unit described in Denevi *et al.* (2013), but may also include flat-floored smooth pools localised on largest craters ejecta blankets.
- IMP Intermediate plains – Smooth undulated to planar surfaces, more densely cratered than SP and superposed both by C3 and C2 craters. Resurfacing processes may have partially covered older C1 craters. IMP are always adjoining with ICP, but seldom present clear boundaries; they rather blend from smooth to rough surfaces with gradational contacts.
- ICP Intercrater plains – Rough, gently rolling surfaces. ICP are the most densely cratered surface on Mercury and encompass distal crater ejecta, all the older unrecognisable crater materials and subdued secondary clusters and chains. All of the three crater classes superpose this unit.

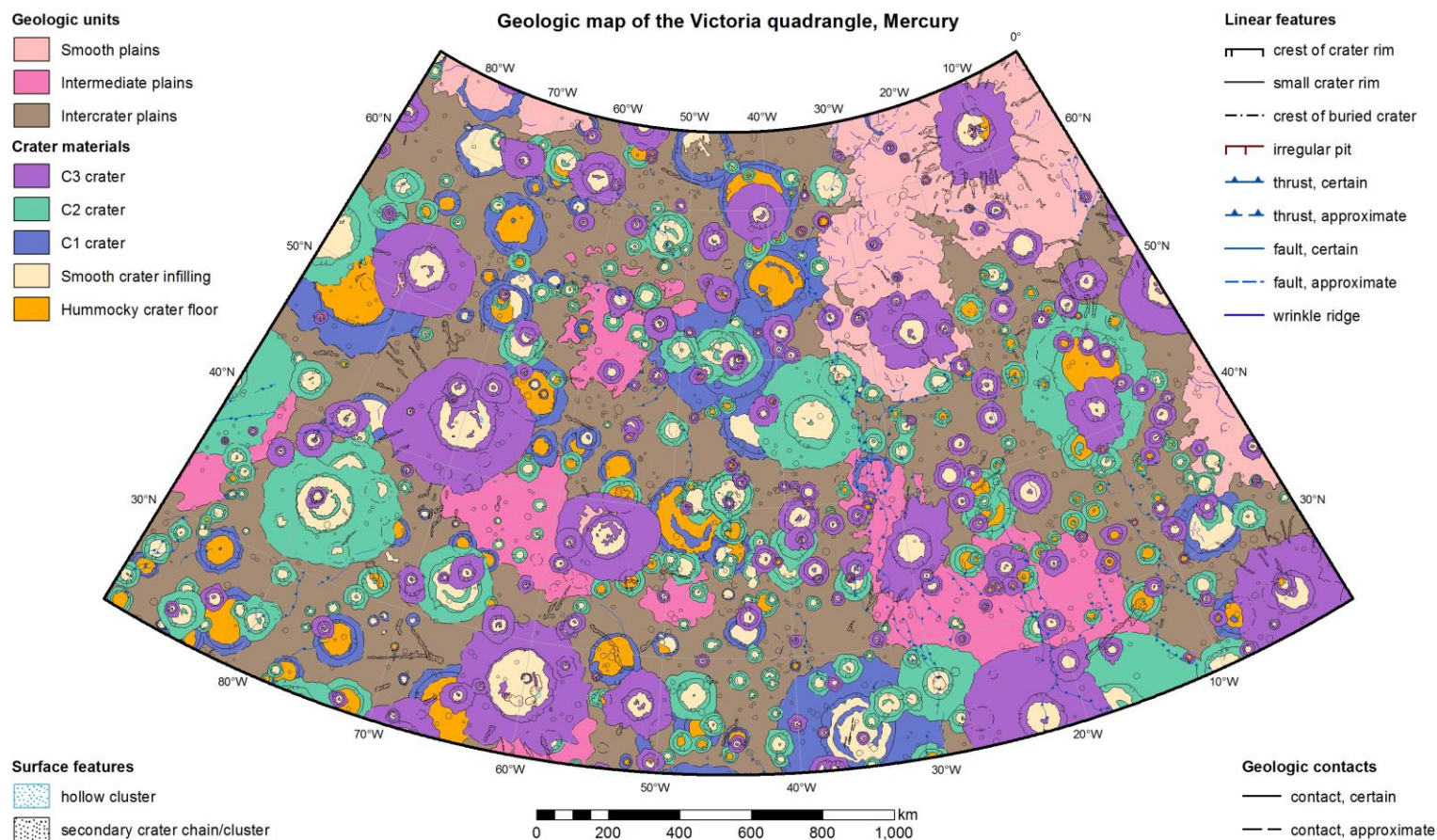


Figure 4.5. Geologic map of Victoria quadrangle (H2) also presented in the 1:3,000,000 scale attached plate.

Stratigraphy of main units

H2 geologic mapping led to the re-introduction of IMP unit, which was recently re-classified into either smooth plains or intercrater plains (Denevi *et al.*, 2013; Whitten *et al.*, 2014). In particular, Denevi *et al.* (2013) critically reviewed the past Mariner 10 mapping of intermediate plains concluding that IMP with poorly defined boundaries and a host of secondary craters can be re-classified as intercrater plains, whereas smoother patches can be re-classified as smooth plains. Moreover, Denevi *et al.* (2013) assess that “the variation in illumination and viewing conditions in Mariner 10 images is likely to have contributed to the large range of surface roughnesses in areas previously mapped as intermediate plains”. However, the mapping scale used in this work (1:600.000) led to the necessity of re-introducing this unit in limited areas of the quadrangle, because of localized textural changes. Despite this, IMP extent is much less than the intermediate plains extent in McGill & King (1983). This is probably due to the difference in resolution between M10 and MESSENGER data, but also to a constraining rule followed during the contact linework. In fact, in case of gradational contacts, IMP were identified by a contact limited to smoother areas (*i.e.* leaving the areas with slightly more secondary craters outside the contact). Inspection of topography reveals that IMP may be related to older ghost crater floors in H2 western region. In H2 eastern region, IMP approximately correspond to a terrain patch mapped as smooth plains by Denevi *et al.* (2013). The re-classification of this eastern patch was motivated by crater classes superposition. In fact, while SP are superposed just by C3 craters, the IMP are superposed by both C2 and C3 craters. No C1 craters were found to superpose this unit in this area.

Intercrater plains are usually described as the oldest “unit” on Mercury, but they are rather a mixture of crater materials and fractured remains of their parent unit (*i.e.* of volcanic origin as argued by most authors, see Whitten *et al.*, 2014, and references therein), which was continuously superposed by cratering. It follows that, the larger the mapping scale and mapping precision, the smaller the extent of the ICP (*i.e.* the extent of the mappable crater materials superposing the ICP is larger). The ambiguity of this terrain unit was already stressed by Guest & O’Donnell (1977) and, although MESSENGER has greatly improved data interpretation, these terrains still remain

poorly constrained by morphological evidence (*e.g.* see the large variety of ICP textures described in Whitten *et al.*, 2014). On the contrary, the younger smooth plains are well defined by their uniform and peculiar smooth texture and sharp boundaries with the adjoining units, thus an increase in resolution would not change their approximate extent.

Based on the above considerations, I propose the stratigraphic scheme shown in figure 4.6 as a possible summary of the units mapped in this quadrangle. In this scheme crater materials are drawn with a breccia-like texture, representing their simple stratigraphic order, rather than all the possible superposition relationships among continuous crater ejecta found in the quadrangle (*e.g.* C3 craters superposing C1 craters).

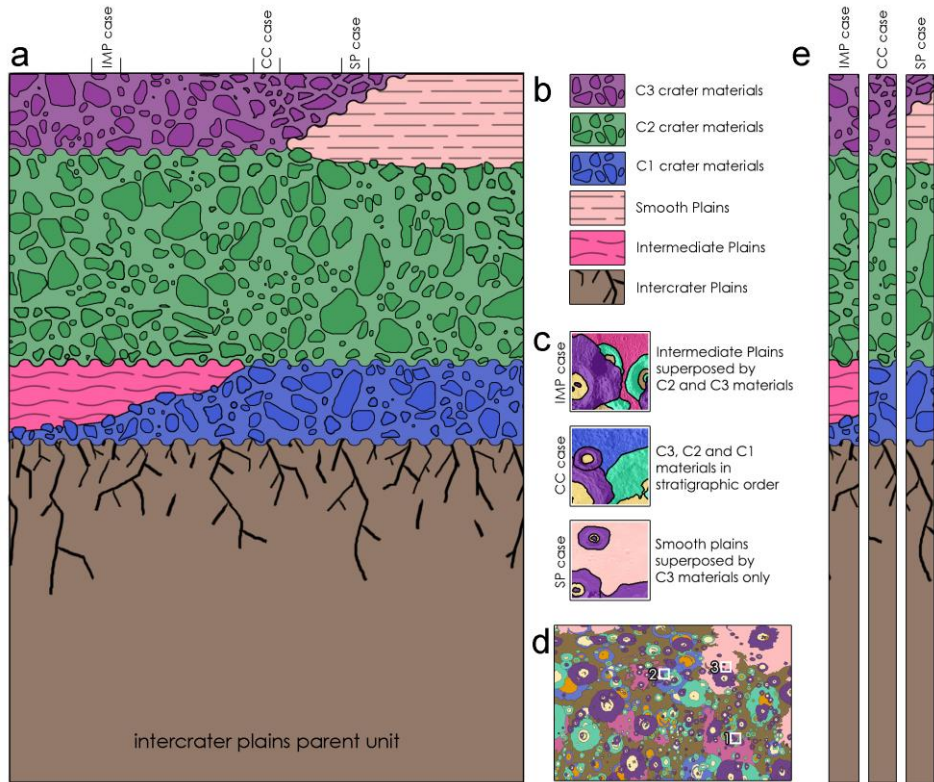


Figure 4.6. (a) Stratigraphic scheme of H2 main units. (b) Legend of units. (c) Three example areas: IMP, Intermediate plains example area; CC, crater classes example area; SP smooth plains example area. (d) H2 quadrangle showing the location of the three example areas. (e) Stratigraphic columns extrapolated from (a) where indicated. See text for details.

4.1.3. Structural framework

The map in figure 4.3 shows more than 400 segments of contractional features (including wrinkle ridges) and more than 200 of these features were digitized as faults (*i.e.* thrusts and generic contractional faults). In figure 4.7 the structural scheme of the area is presented associated with rose diagrams of the mapped faults. Rose-diagrams were obtained plotting the mapped segments as length-weighted 5° bins, such that more importance is given to the most prominent faults. Rose diagram (RD) –a (Fig. 4.7) clearly shows the presence of two main fault families: one family is ~NNW–SSE oriented, the second family is NE–SW oriented. In RD–a a N–S trend is highlighted and it is clearly due to the Victoria Rupes, Endeavour Rupes and Antoniadi Dorsum alignment (see nomenclature labels in Fig. 4.7). Moreover, a single bin in figure 4.7a is evidenced within the less-populated NW–SE trend and this is due to the prominent Carnegie Rupes in the central-western part of the quadrangle (see nomenclature label in Fig. 4.7). The evidence shown by RD–a is observable also on RD–b, where only the thrust strikes are plotted, but the NE–SW family is not clearly recognisable as it was in RD–a. The NE–SW populated trend is better observable in RD–c, which shows the resulting strikes of the less prominent contractional faults (mapped as “other contractional faults”) to the west and to the south of Carnegie Rupes. A summary of these observations is presented in RD–d, where all kinds of contractional faults (thrusts and other contractional faults) are plotted together. Wrinkle ridges, mapped as an independent category of morphostructural features (see Tab. 3.2), are analysed in RD–e. Rose plot –e shows that wrinkle ridges are more randomly distributed with a preferential ~E–W strike.

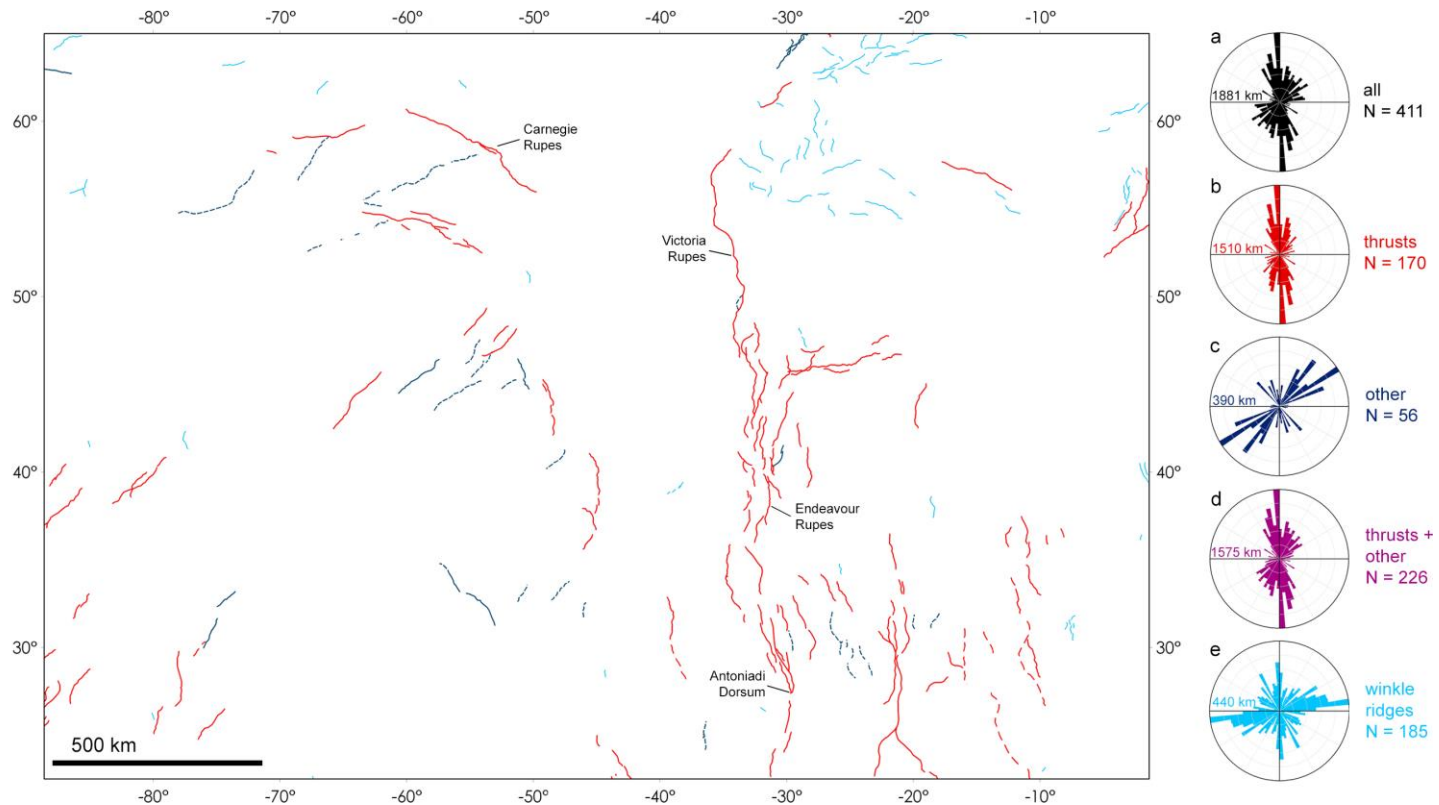


Figure 4.7. Structural scheme of Victoria quadrangle in equidistant cylindrical projection (centre Lat. 43.75° N; centre Lon. 45° W), colours correspond to the rose plots on the right. Rose diagrams a–e show the azimuths of the mapped morphostructural feature azimuths weighted to segment lengths, the maximum cumulative length is indicated to the inner left of the outer circle: (a) all features (black); (b) thrusts (red); (c) other contractional faults (blue); (d) thrusts and other contractional faults together (purple); (e) wrinkle ridges (cyan). The diagrams use N values indicated to the right, divided per 5° bins.

As a conclusion to these observations and considering the most representative RDs in figure 4.7, it is possible to overlay RD-b and RD-c in one single normalised rose plot (Fig. 4.8). Wrinkle ridges are constrained to the smooth plains unit and probably related to processes concerning the northern smooth plains in quadrangle Borea (H1), thus they will not be considered in this analysis. From the analysis of figure 4.8, it can be said that Victoria quadrangle has three main fault systems, a ~N-S system, a ~NE-SW system and a less populated ~NW-SE system. The first one ranges from 0° to 25° and from 150° to 180° (i.e. ~N-S, in a 180° azimuth range without considering dip direction, pink area in Fig. 4.8) and is predominant in this area, thus it will be addressed to as the “Victoria system” (VS), since it also encompasses Victoria Rupes. The second one ranges mainly from 25° to 80° (blue area in Fig. 4.8), but in order to encompass also ENE-WSW minor segments (i.e. smaller bins) striking $> 80^{\circ}$, the whole 25° – 90° range was considered in this system; since this system encompasses weak and unnamed linear features, I will use the name of a large crater located in the middle of the area cross-cut by these faults to address it as “Larrocha system” (LS). The final system has few faults, but in order to encompass also smaller bins and finally cover the whole 180° range (i.e. 360° in the specular plot of Figure 4.8), it is considered to stand between 90° and 150° (yellow area in Fig. 4.8); it includes the Carnegie Rupes thrust, thus it can be addressed to as the “Carnegie system” (CS). The poorly populated range between 80° and 120° (grey dots in Fig. 4.8), which encompasses both the LS and the CS smaller bins, is better discussed in the paragraph called *The illumination bias*.

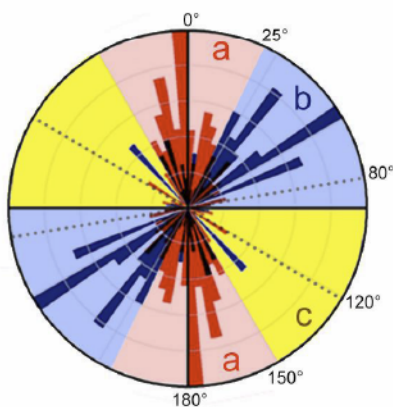


Figure 4.8. This rose diagram was constructed overlapping RD-f on RD-d (Fig. 4.7) and resizing RD-f outer circle to the extent of RD-d. These two rose diagrams were chosen as the most representative for assessing the azimuth ranges of the two main H2 fault systems. Azimuths are given in the 180° range since this is a specular plot. (a) The pink areas (0° – 25° and 150° – 180°) highlight the azimuth ranges for the “Victoria system”. (b) The light blue area (25° – 90°) highlights the azimuth range for the “Larrocha system”. (c) The yellow area (90° – 150°), highlights the azimuth range for the “Carnegie system” (see text for details). The grey dotted lines indicate a poorly populated range between 80° and 120° .

In figure 4.8, Victoria system and the oblique systems (Larrocha and Carnegie) seem to be identified mostly by thrusts and other contractional faults, respectively. However both fault categories can have a wide range of strikes (*e.g.* compare the smaller bins in RD–b and –c in Fig. 4.7), thus they must not be intended as representative of either system. Inspection of figure 4.7, also reveals that the three fault systems seem to be located preferentially either on the central-eastern area (Victoria system), or on the western area (Larrocha and Carnegie systems). Fault strikes abruptly change at $\sim 50^\circ$ W, however, Larrocha system \sim NE–SW segments are present also on H2 eastern part. This evidence requires a more thorough analysis of the three fault systems.

The illumination bias

The rose plot shown in figure 4.8 shows a poorly populated range between 80° and 120° and thus a decrease in bin size along the E–W direction. This trend is usually considered biased by the predominant E–W illumination direction on Mercury’s surface (*e.g.* Di Achille *et al.*, 2012). However, as seen in RD–i and –j (Fig. 4.7), the E–W direction seems to be well covered by the strikes of wrinkle ridges, which (being smaller) should be less prominent than thrusts and other contractional faults. Hence, the large variety of basemaps and mosaics used for mapping H2 quadrangle (see chapters 2.3 and 2.4) probably permitted to avoid, as much as possible, the illumination bias described in Di Achille *et al.*, 2012.

Victoria system (VS)

Faults involved in the VS can be better analysed if divided into different groups and sub-groups. In particular, I defined the following sub-groups hierarchy: 1) system; 2) array; 3) sector; 4) segment. As explained above, fault systems were identified by the main trends observable with rose plot analysis (Fig. 4.8). Arrays are identified by analysing the longitudinal continuity and distribution of fault segments. Sectors are identified mainly by their spreading degree and clustering, although also their dip direction may be a reason for defining a group. In figure 4.9, the VS arrays and sectors are indicated.

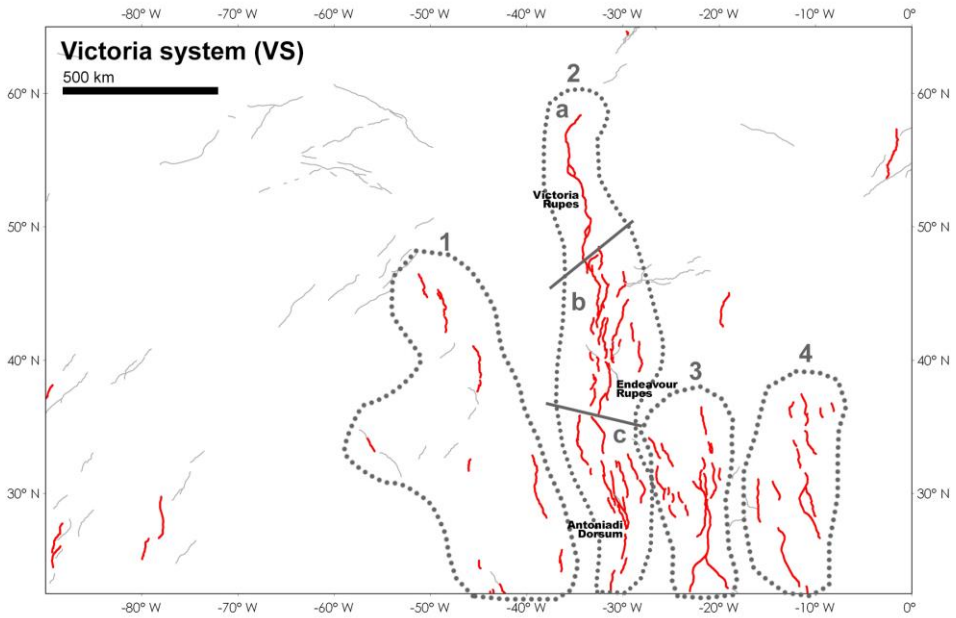


Figure 4.9. Scheme of Victoria system (VS) arrays and sectors. Red lines: VS fault segments. Light grey lines: CS and LS fault segments. The grey dotted areas indicate four different arrays labelled with numbers (1–4). Sectors are divided by grey solid lines and labelled with internal letters (a–c).

Victoria system is divided into four arrays: VS–1, VS–2, VS–3 and VS–4 (Fig. 4.9) plus few scattered and isolated segments interconnected with the oblique system.

Array VS–1 is a discontinuous and less populated array (~10 segments), which coexists with or intersects the oblique CS and LS segments and is mostly characterized by west-dipping thrusts.

VS–2 is the main array in terms of development and morphological relief, and is identified from north to south by Victoria Rupes, Endeavour Rupes and Antoniadi Dorsum. These three features are the prominent reasons for distinguishing three sectors: VS–2a, VS–2b and VS–2c, respectively (Fig. 4.10). The Victoria Rupes sector (VS–2a) is characterized by a more than 550 km long continuous west-dipping thrust, the longest thrust segment inside H2 (Fig. 4.10a). Conversely, the Endeavour Rupes sector (VS–2b) is characterized by more than 25 segments scattered on a ~150 km wide faulted zone (Fig. 4.10b). It encompasses both east- and west-dipping thrusts and cuts a narrow IMP area, which seems to be confined to the south by a north-dipping thrust segment in its

easternmost patch. VS-2b main fault segments cross-cut a resurfaced crater (see centre of figure 4.10b), while two oblique faults (visible in the geologic map of Fig. 4.10b) seem to follow the crater south-margins, which probably aided the nucleation of these smaller fault branches (*e.g.* see Rothery & Massironi, 2013; Massironi *et al.*, 2015). The Antoniadi Dorsum sector (VS-2c) encompasses almost 20 segments that form a lozenge-shaped fault zone mostly within IMP deposits, with a maximum width of ~ 110 km. The fault zone narrows to the south and ends with a single segment at the boundary with H6 Kuiper quadrangle (Fig. 4.10c).

The abrupt change in segment frequency between VS-2a and VS-2b happens almost in correspondence of the unnamed pit-bearing crater in figure 4.10a and this is probably due to a different rock rheology.

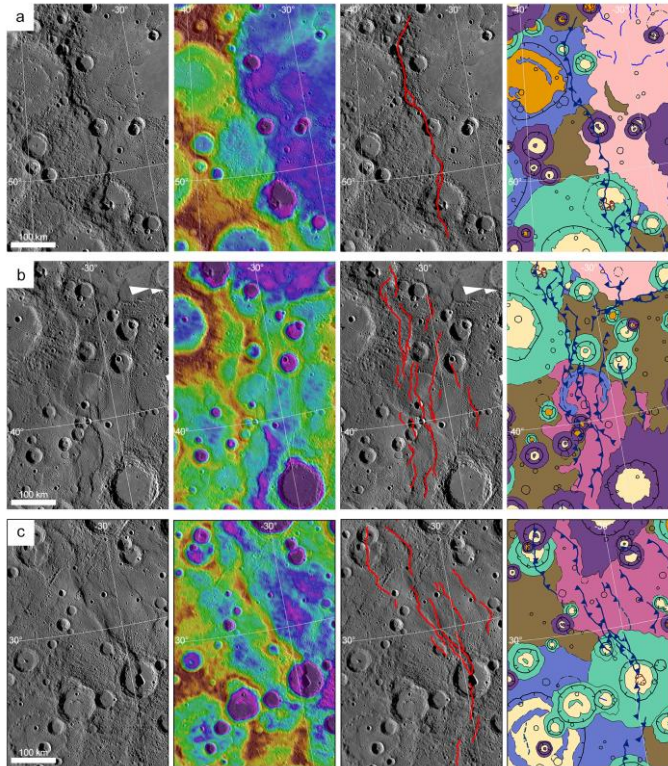


Figure 4.10. Overview of VS-2 array in LCC projection. The four columns show from left to right: MDIS BDR basemap (166 mpp), stereo-topography (Preusker *et al.*, 2011) with colour coding scaled to the view extent, fault segments (red lines) interpreted to belong to each sector on MDIS BDR basemap and geologic map (this work, refer to Fig. 4.5 for colour legend). (a) VS-2a sector. (b) VS-2b sector. (c) VS-2c sector.

Array VS-3 encompasses more than 20 segments east of Antoniadi Dorsum scattered across a ~ 220 km wide zone that develops through the easternmost IMP unit (Fig. 4.11a). This array apparently blends with VS-2c described above. Array VS-4 comprises 14 widely spaced fault segments east of VS-3 that develop more on ICP rather than IMP (Fig. 4.11b).

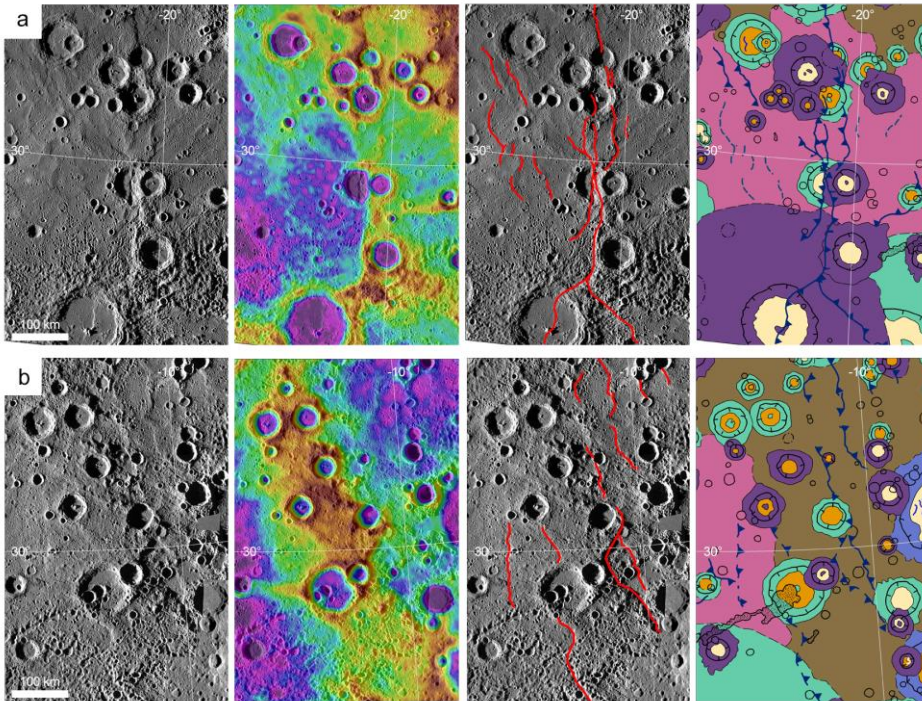


Figure 4.11. Overview of VS-3 and VS-4 arrays in LCC projection (rotated 20° clockwise for a better output view). The four columns show from left to right: MDIS v8 basemap (250 mpp), DLR topography (Preusker *et al.*, 2011) with colour coding scaled to the view extent, fault segments (red lines) interpreted to belong to each array on MDIS v8 basemap and geologic map (this work, refer to Fig. 4.5 for colour legend). (a) VS-3 array. (b) VS-4 array.

Carnegie system (CS)

Carnegie system is composed of few scattered fault segments, and following the same group hierarchy adopted for VS, the CS can be divided as shown in (Fig 4.12). Most of these segments coexist with the other fault systems and, in particular, the southern CS segments coexist with VS segments. The only analysable array of this system is represented by the Carnegie Rupes area (see Fig. 4.12). Array CS-1 is divided into two

sectors: CS-1a is constituted uniquely by the Carnegie Rupes, a 330 km long, NE dipping thrust, and CS-1b encompasses more discontinuous parallel segments with a total length similar to Carnegie Rupes. The two sectors cross-cut and are linked by a LS segments, thus they will be better analysed in that context. Array Cs-1 includes mainly east-dipping thrusts, being thus antithetic to the west-dipping thrusts of VS-2a to the east. A further analysis of CS-1 reveals that it might be in continuity with the VS-1 segments to the south that, although west-dipping like the VS-2 array, they are alternating with LS segments just like CS-1.

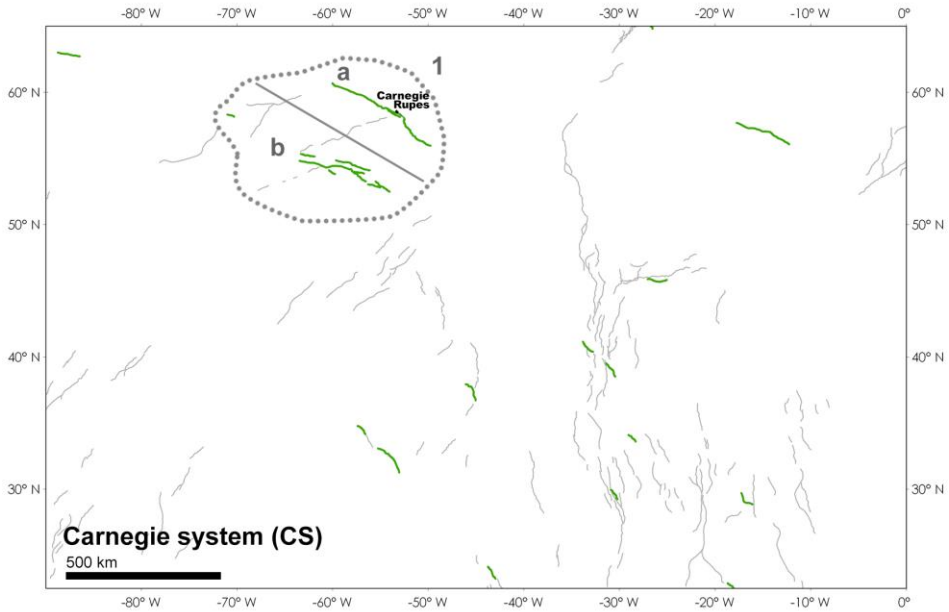


Figure 4.12. Scheme of Carnegie system (CS). Green lines: CS fault segments. Light grey lines: VS and LS fault segments. The grey dotted line encloses array CS-1. Sectors are divided by a grey solid line and labelled with internal letters (a-b).

Larrocha system (LS)

The array/sector subdivision adopted for Larrocha system is shown in figure 4.13. In this case, arrays were distinguished following fault segments aligned along a ~NE-SW direction.

The main evidence is that LS is split into two areas divided by a wide segments-free area (> 400 km wide) around -40°W . This gap is also free of CS segments and poor in VS segments and is limited by the continuous VS-2 array segments to the east.

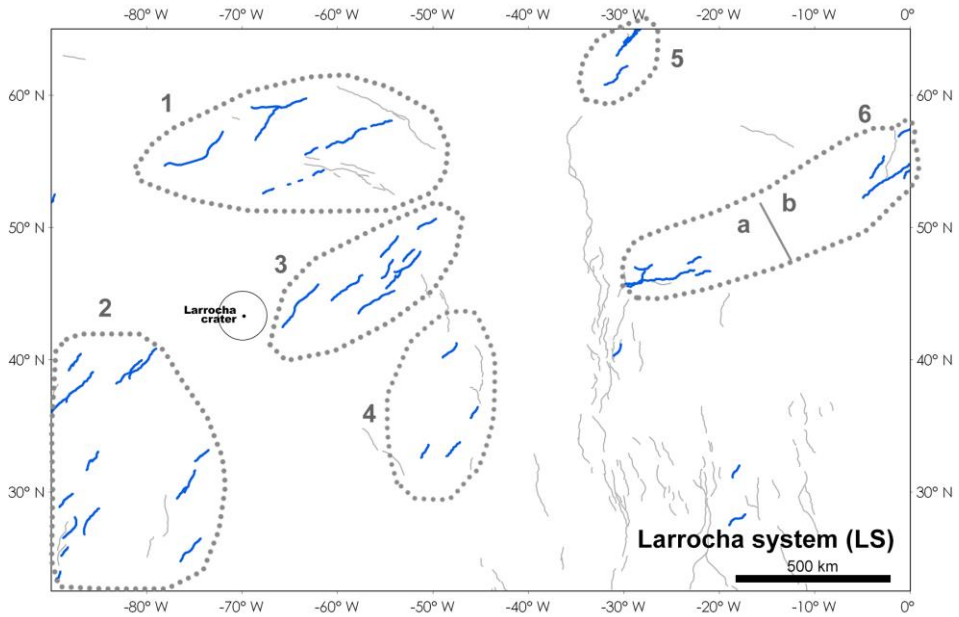


Figure 4.13. Scheme of Larrocha system (LS). Blue lines: LS fault segments. Light grey lines: VS and CS fault segments. The grey dotted lines enclose six different arrays labelled with numbers (1–6) so that arrays 1–4 are enclosed in H2 western area and arrays 5–6 inside H2 eastern area. The grey solid line divides LS-6 into two sectors labelled with internal letters (a–b).

LS-1 is characterised by long segments alternating with CS-1 array segments. The two system arrays cross with each other in opposite directions creating a lozenge-shaped pattern at 30° angles in map view (Fig 4.14a). The LS-1 segments are less prominent than Carnegie Rupes and were inferred from slight shadow and topographic evidence (see white arrows in Fig. 4.14a). LS-2 is constituted by sparse segments that clearly continue to H3 quadrangle. LS-3 segments constitute a NE–SW clustered alignment shown in figure 4.14b. LS-4 array coexists with VS-1 array and its segments seem to interrupt the continuity of the longitudinal segments.

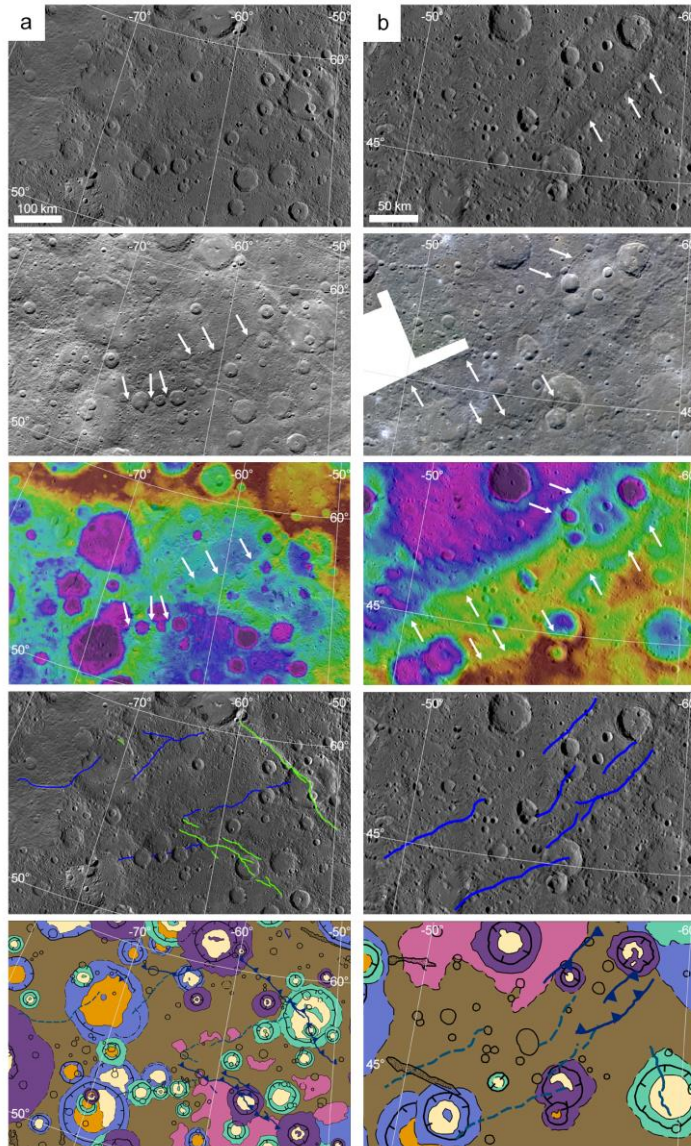


Figure 4.14. Details of CS-1, LS-1 and LS-2 arrays in LCC projection. (a) CS-1 and LS-1 arrays intersecting each other. The easternmost NW-SE fault is Carnegie Rupes cross-cutting Duccio crater; (b) a detail of LS-2 array. The five rows show from top to bottom: BDR basemap (166 mpp), WAC-G mosaic (200 mpp, see H2-Bm-6 in chapter 2.3) in (a) and MD3 colour mosaic (332 mpp, see H2-Bm-8 in chapter 2.3) in (b), MLA topography in (a) and stereo-topography (Preusker *et al.*, 2011) in (b) with colour coding scaled to the view extent, CS fault segments (green lines) or LS fault segments (blue lines) on the BDR basemap and geologic map (this work, refer to Fig. 4.5 for colour legend). White arrows indicate aligned shadows and related topography that allowed location of some approximate faults.

The northern array LS-5 seems to be aligned with VS-2a, but it is actually represented by few weak segments crossing smooth plains. However, it might be linked to the VS-2a northern virgation happening at 56.9° N, 36.9° W (visible in Fig. 4.10), being thus part of the same fault family. Array LS-6 is represented by two main NE-SW striking faults (and their associated minor segments) that partially function as a smooth plains boundary. Since the main segments are 500 km away from each other, two different sectors were distinguished (*e.g.* see sector LS-6a in Fig. 4.15); their strike seems aligned with the western LS-2 array.

Further interpretation and discussion of the described fault systems is presented in chapter 5.

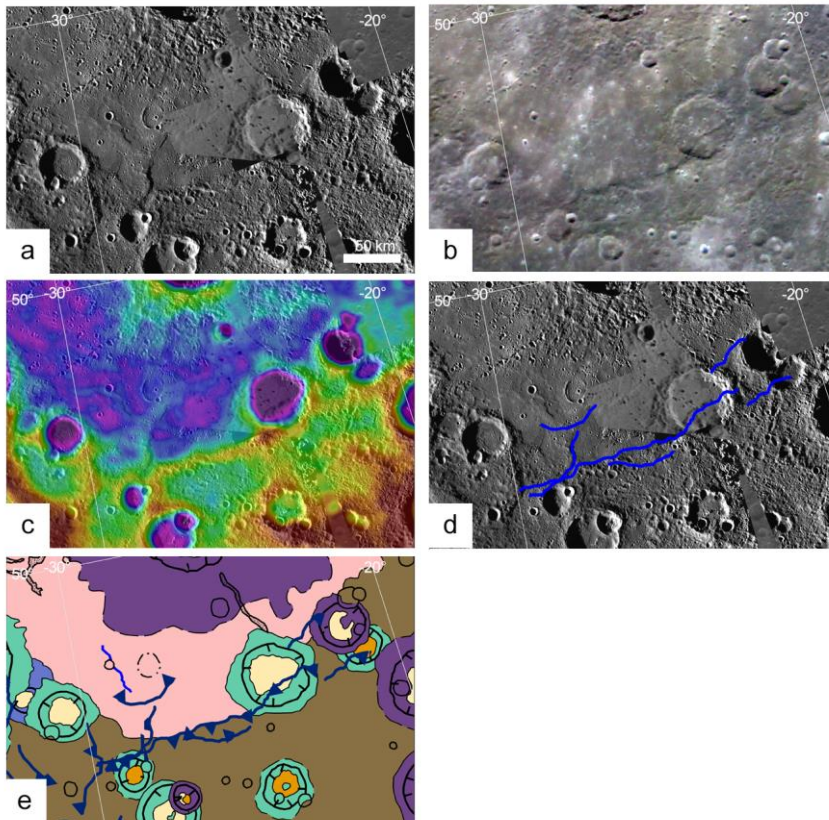


Figure 4.15. Details of LS-6a sector in LCC projection. (a) MDIS complete basemap (250 mpp); (b) MDR colour mosaic (665 mpp, see H2-Bm-9 in chapter 2.3); (c) stereo-topography (Preusker *et al.*, 2011) with colour coding scaled to the view extent; (d) sector related fault segments (blue lines) on MDIS basemap; (e) geologic map (this work, refer to Fig. 4.5 for colour legend).

4.1.4. Relative age of map elements

Using the crater linework of the H2 geologic map, which encompasses all craters > 5 km, it was possible to build the crater counting dataset shown in figure 4.16. In this crater counting layer most of the secondary craters were already excluded during the mapping process. However, a bias from secondaries is not excluded since it is believed that on Mercury, craters smaller than 10 km are likely the result of secondary cratering (Strom *et al.*, 2008; Xiao *et al.*, 2014).

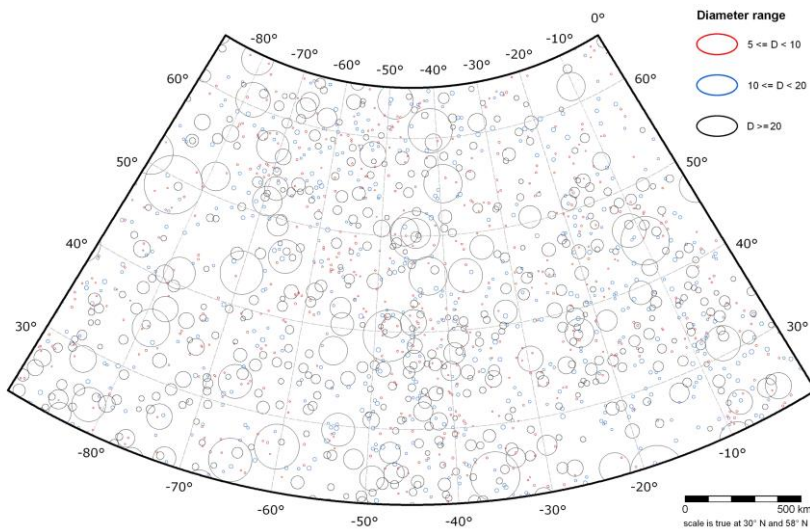


Figure 4.16. Crater counting layer obtained re-drawing the mapped craters (> 5 km) with CraterTools for ArcMap (Kneissl *et al.*, 2011). The less densely cratered patches correspond either to smooth plains areas or to regions biased by secondary crater chains and clusters.

Relative age of map units

The dataset in figure 4.16 was used with the study areas shown in figure 4.17 to assess the relative ages of each location and the average relative ages of the main geologic units. For smooth plains and intermediate plains, I chose the widest areas covered by these units removing from the counting layer all those reshaped and covered craters.

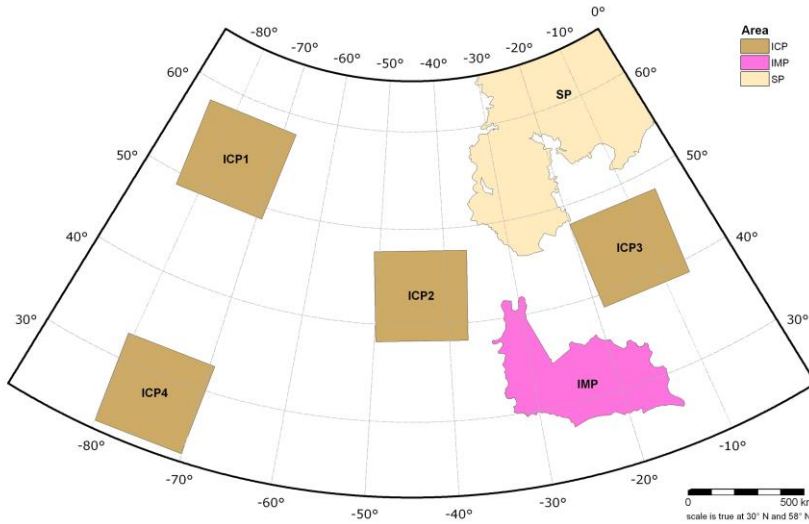


Figure 4.17. Selected study areas within Victoria quadrangle. Refer to table 4.1 for area information and details.

Results for the counted areas are shown in table 4.1 in terms of N(5), N(10) and N(20) (see chapter 3.3.1), and with the SFD in figure 4.18. A cumulative count of all ICP areas is also presented (i.e. “ICP”).

Table 4.1. Crater counting results for study areas.

Name	Area km ²	craters ^a	N(5)	N(10)	N(20)
SP	420334	97	209 ± 22	105 ± 16	40 ± 10
IMP	227311	80	347 ± 39	246 ± 33	84 ± 19
ICP1	161790	57	525 ± 57	390 ± 49	134 ± 29
ICP2	163950	86	352 ± 47	210 ± 36	99 ± 25
ICP3	163978	60	366 ± 47	238 ± 38	98 ± 24
ICP4	157858	34	215 ± 37	171 ± 33	114 ± 27
ICP	647576	237	366 ± 24	253 ± 20	111 ± 13

^a number of counted craters with centre falling inside the counting area

Inspection of figure 4.18 reveals the relative age of H2 main geologic units. As expected, smooth plains and intercrater plains SFDs are widely spaced and confirm the older age of ICP with respect to SP. The IMP counted area too confirms the intermediate age of this unit, however the cumulative frequency of craters smaller than

~ 15 km coincides with that of ICP; this is consistent with the findings by Whitten *et al.* (2014) that observed the same overlapping results between ICP and IMP for craters smaller than a given diameter. The grayed-out areas in figure 4.18 indicate diameters smaller than 10 km that are believed to be biased by the result of secondary cratering, thus SFD slope should be steeper in that area.

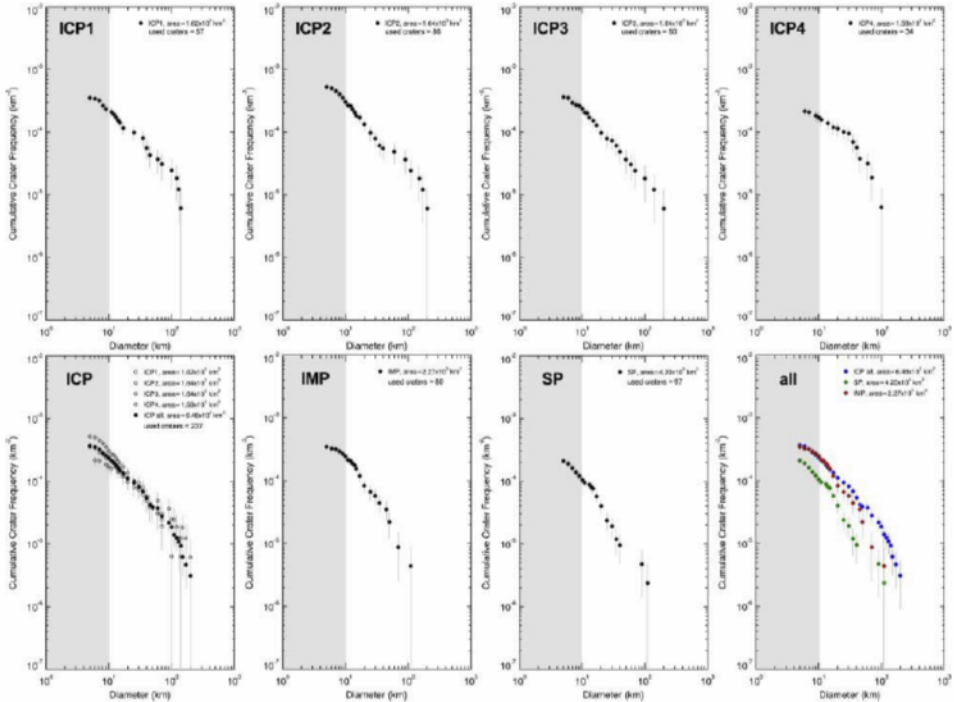


Figure 4.18. Crater counting results for H2 study areas shown in figure 4.17 with pseudo-log binning (see Hiesinger *et al.*, 2000). The grey areas indicate the plot region highly biased by secondaries. The plot marked "ICP" shows an overlap of plots ICP1 to ICP4 (empty circles) and their average cumulative SFD (solid circles). The plot marked as "all" shows the comparison between H2 main geologic units: smooth plains (green), intermediate plains (red) and intercrater plains (blue).

Relative age of fault systems

In chapter 4.1.3 three different fault systems were found inside H2 quadrangle, however only one out of the three, the Victoria system, was suitable to provide enough data to assess its relative age with SFD. This issue is mainly due to the young age of Hermean faults that are seldom superposed by impact craters (*e.g.* Watters *et al.*, 2004, 2009; Solomon *et al.*, 2008). Since VS is the most developed system and presents an

interesting relationship with the smooth plains unit, its results alone were found to be sufficient for a comparative analysis with H2 geologic units. In figure 4.19, an extended view of Victoria quadrangle shows the buffered area along most of the VS fault segments and also along the northern LS-5 array, whose trend seemed to be coherent with the northern tip turn of the VS-1a sector. Results of the buffered crater counting are shown in the inset in figure 4.19 and are compared to the main units' cumulative SFDs in figure 4.20. The buffered crater counting SFD was not obtained using the standard counting layer derived from mapping in figure 4.16. Instead, craters superposing the structures were mapped anew, adding to the counting even craters > 1 km, while craters > 20 km were considered only if classified as C_3 craters. Results shown in figure 4.20 prove that the activity of Victoria system (plus some VS-like segments from the other systems) continued after the emplacement of smooth plains.

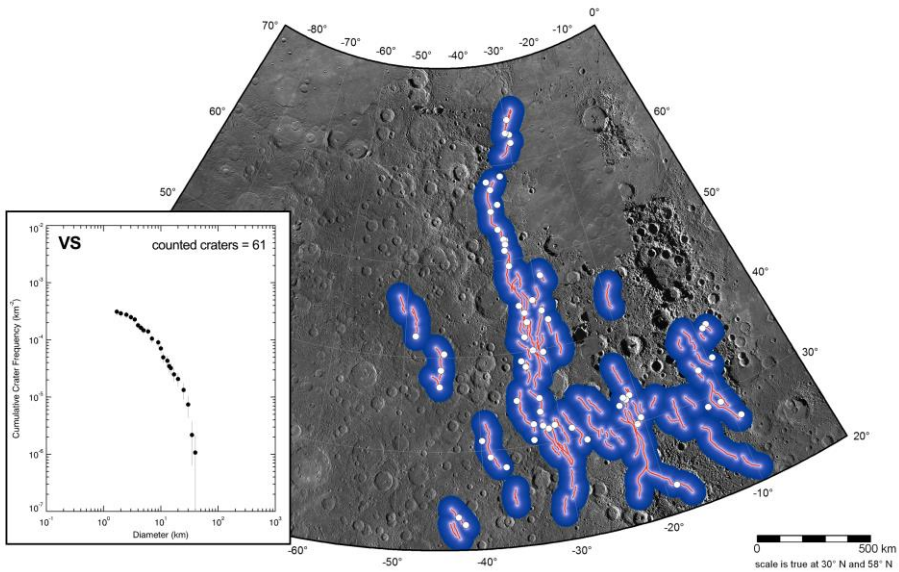


Figure 4.19. Buffered crater counting results for the VS system plus LS-5 array and some interspersed oblique segments. Faults (red lines) was buffered 61 times, with a different S_{buffer} for each crater superposing the structures. Buffers fade from light blue (smaller buffers) to dark blue (larger buffers). Red lines are the buffered fault segments. The white circles represent the location of the 61 counted craters (> 1 km). The VS inset shows the resulting cumulative SFD.

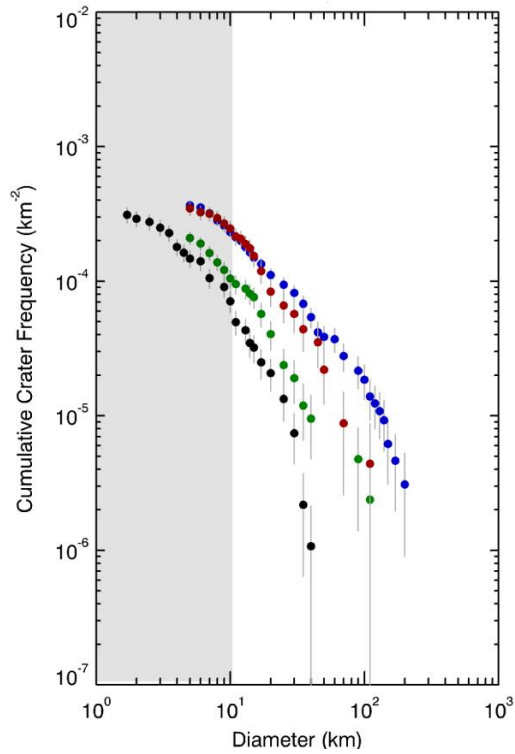


Figure 4.20. Cumulative SFDs with pseudo-log binning (see Hiesinger *et al.*, 2000) showing the comparison between H2 main units (refer to Fig. 4.18 for legend) and VS faults (black solid circles). The grey area indicates the plot region highly biased by secondaries.

4.2. Kinematic analysis results

The results presented below are an extract from Galluzzi *et al.* (2015) that contains an updated table with one additional analysed crater. This analysis is referred to 30% of Mercury, and is followed by a closer look at the H2 quadrangle, which needs a dedicated discussion to constrain the structural analysis results made in the previous paragraphs.

Mercury is probably the best planet where to apply the method described in Chapter 3.2. The surface of Mercury abounds in craters, which still keep recognisable rims (although many have been moderately modified by space weathering or gravitational processes), and it abounds in morphostructural features, especially lobate scarps. Therefore, the method can be applied to those craters cross-cut by Mercurian lobate scarps to obtain fault dips and rakes.

4.2.1. Mercurian faulted craters

The stereo-topographic models by Preusker *et al.* (2011) (see Chapter 2.5) were used to retrieve kinematic data on the analysed faults. This DTM covers 30% of Mercury's surface with a grid spacing of 1 km and it allows reliable measurements of features with a horizontal extent of at least 15 km.

Within the limits imposed by data coverage, resolution and illumination, 45 craters intersected by linear features, for which topographic data were available, were found. Most of these craters had to be excluded, however, due to the following reasons and observational limits: (a) small wrinkle ridges at the crater floors, which might result from local stress fields rather than from global contraction; (b) faults too small to produce a resolvable dislocation on the rim; (c) craters too close to DTM boundaries, where there are higher uncertainties in elevation estimates; and (d) craters with complicated morphology such as palaeo-landforms inherited by older and larger underlying ghost craters, whose pre-existing slopes were not totally reset after the formation of younger craters. Discarding all the above cases, 15, plus one new crater, out of 45 craters were found suitable for the described analyses (Fig. 4.21).

The 16 faulted craters were numbered sequentially and accompanied by a letter corresponding to the cross-cutting fault (Tab. 4.2). This means that craters 01–A, 02–A and 03–A are cross-cut by the same lobate scarp (Carnegie Rupes, Fig. 4.22a), as are craters 08–F, 09–F and 10–F, which are located in the Rembrandt crater area (*i.e.* by Enterprise Rupes, Fig. 4.22b). Craters 02–A and 03–A, along with craters 11–G and 13–I (Figs. 4.22c and 4.22d, respectively), are the smallest craters of the dataset in table 4.2. While the results of the first two craters can be compared with the results of the underlying older crater 01–A (see chapter 4.2.3), the results from craters 11–G and 13–I cannot be verified with any other feature; their reliability will therefore be treated with caution in the subsequent analysis. Craters 08–F, 09–F and 10–F are located on Enterprise Rupes (Fig. 4.22b). There is no superposition relationship among the three craters and they are probably similar in age, although they in fact yield a different estimate of the fault dip δ . This is likely a function of the fault strike, which changes substantially eastwards from crater 08–F to crater 10–F (N 263° to N 216°; Tab. 4.2), although the slip trend remains almost the same for craters 08–F and 09–F (N 107° and N 116°, respectively; Tab. 4.2) and is different for crater 10–F (N 158°; Tab. 4.2). The resulting rake for crater 09–F is in fact 116° (close to dip-slip), 141° (right oblique-slip) for crater 08–F and 59° (left oblique-slip) for crater 10–F. Craters 08– to 10–F confirm the existence of a consistent relationship between the fault rake and its dip, discussed in chapter 5.2. The lowest derived dips of 9° and 7° are those obtained for craters 07–E (Thakur) and 12–H, respectively (Figs. 4.22g and 4.22h). Such low dips are consistent with the accentuated arcuated shape in plan view of the fault scarp trace. As a comparison, crater 06–D (Fig. 4.22i), which is cross-cut by a more rectilinear lobate scarp than those of the abovementioned craters, leads to a steeper dip estimate (29°; Tab. 4.2).

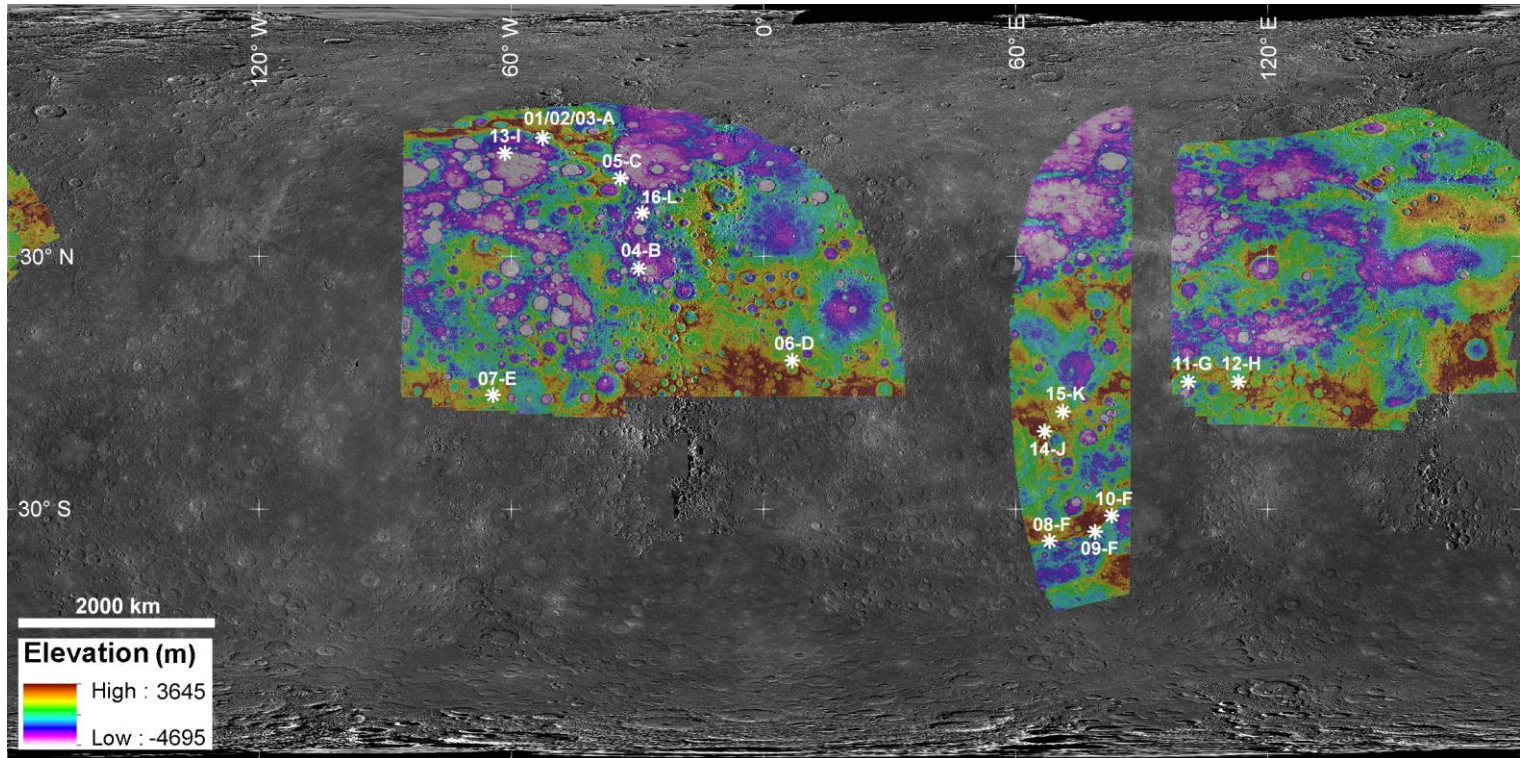


Figure 4.21. Global map of Mercury in equirectangular projection (MDIS orbit mosaic v9 by NASA/JHUAPL/CIW), associated with the stereo-DTM by Preusker *et al.* (2011), showing the location of the studied faulted craters.

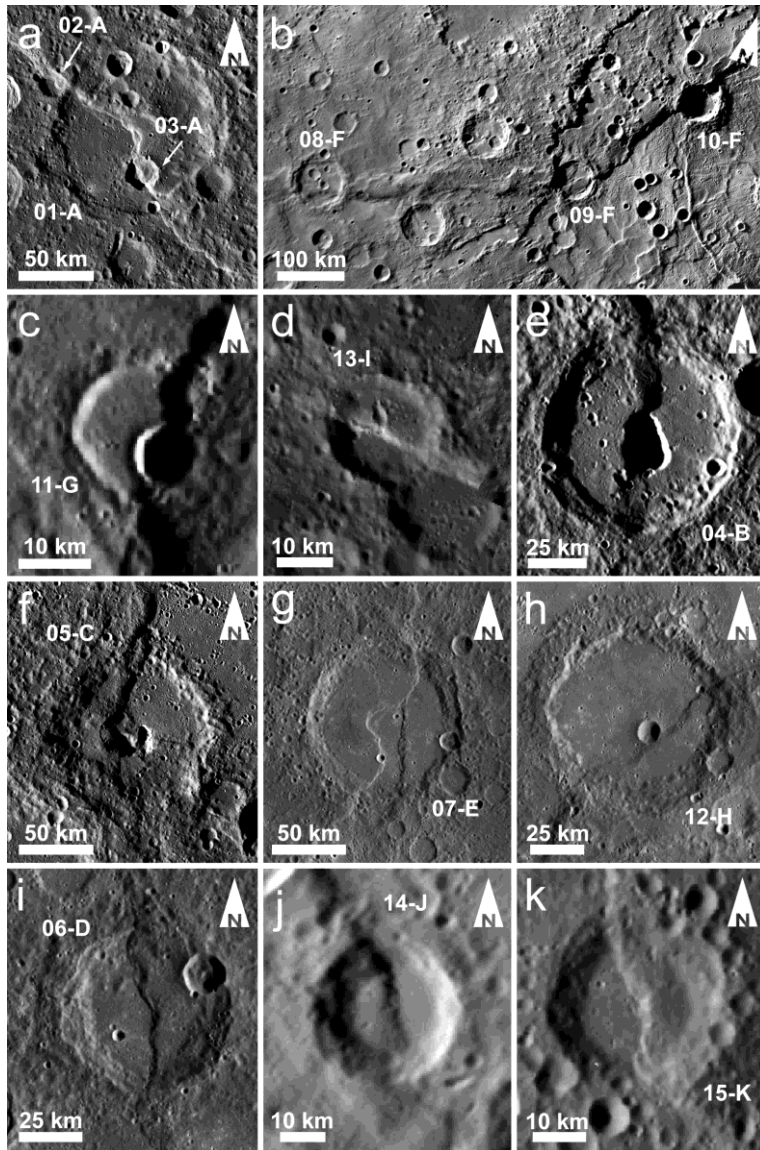


Figure 4.22. MDIS images of the 15 analysed faulted craters of Mercury from Galluzzi *et al.*, 2015 in stereographic projection. The new crater 16-L is presented in chapter 4.2.2. All the images are taken from the 250 mpp v8 mosaic, except for (f) and (j), which are taken from the 500 mpp mosaic by Becker *et al.* (2009) (a) Craters 01-A, Duccio (largest crater), 02-A and 03-A (white arrows) on Carnegie Rupes. (b) From West to East, craters 08-F, 09-F and 10-F on Enterprise Rupes. (c) Crater 11-G, on Beagle Rupes. (d) Crater 13-I. (e) Crater 04-B, Geddes on Antoniadi Dorsum. (f) Crater 05-C, on Victoria Rupes. (g) Crater 07-E, Thakur. (h) Crater 12-H. (i) Crater 06-D. (j) Crater 14-J. (k) Crater 15-K.

Table 4.2. Dislocation data of Mercurian faulted craters

Crater	Lon. (dd)	Lat. (dd)	Diameter (km)	Δx^a (km)	Δh (km)	n	$\sigma \Delta h$ (km)	trend ^b	plunge	σ plunge	strike ^c	δ	$\sigma \delta$	φ^b	λ	$\sigma \lambda$	D (km)	σD (km)
01-A ^d	-52.5	58.2	109.90	4.14	2.43	6	0.25	241°	30°	4°	323°	31°	4°	82°	83°	10°	4.80	0.70
02-A ^d	-55.0	58.9	18.27	1.19	1.53	1	0.14	218°	52°	4°	297°	53°	4°	79°	83°	7°	1.94	0.20
03-A ^d	-52.3	57.5	22.13	1.43	1.25	1	0.14	236°	41°	4°	333°	42°	4°	97°	95°	9°	1.90	0.26
04-B ^d	-29.6	27.1	87.30	4.52	1.14	4	0.22	104°	14°	3°	185°	14°	3°	81°	81°	14°	4.66	1.29
05-C ^d	-34.0	49.4	98.57	3.96	1.42	3	0.20	96°	20°	3°	183°	20°	3°	87°	87°	14°	4.20	0.88
06-D	6.9	5.3	64.79	1.89	0.77	4	0.14	223°	22°	4°	356°	29°	8°	133°	129°	12°	2.04	0.50
07-E	-64.4	-3.0	107.98	4.44	0.69	3	0.18	90°	9°	2°	199°	9°	3°	109°	109°	15°	4.50	1.67
08-F	68.1	-37.9	79.73	3.07	1.89	4	0.16	107°	32°	3°	263°	57°	16°	156°	141°	7°	3.60	0.46
09-F	78.8	-35.5	59.70	2.93	1.47	5	0.34	116°	26°	6°	235°	30°	7°	119°	116°	10°	3.27	0.99
10-F	82.9	-31.7	55.51	3.96	0.93	6	0.22	158°	13°	3°	216°	15°	5°	58°	59°	11°	4.07	1.41
11-G	101.2	0.2	16.63	1.87	0.54	1	0.14	335°	16°	4°	12°	26°	10°	37°	40°	10°	1.94	0.68
12-H	113.1	0.2	85.83	4.43	0.53	5	0.22	343°	7°	3°	55°	7°	3°	72°	72°	13°	4.46	2.59
13-I ^d	-61.5	54.6	20.38	1.67	0.33	1	0.14	181°	11°	5°	292°	12°	5°	111°	111°	15°	1.71	0.98
14-J	66.9	-11.6	32.14	0.82	0.79	1	0.14	85°	44°	6°	161°	45°	6°	76°	80°	10°	1.13	0.23
15-K	71.3	-6.9	32.33	2.39	0.40	1	0.14	253°	10°	3°	343°	10°	3°	90°	90°	14°	2.43	1.16
16-L ^{d,e}	-28.2	39.9	15.01	1.08	0.39	3	0.14	96°	20°	7°	167°	21°	7°	71°	72°	14°	1.15	0.54

^a the standard deviation is assumed to be 10% of the value

^b the standard deviation is 15° for all angles

^c the standard deviation is 1° for all angles

^d This crater is inside H2 quadrangle. For craters with $n > 1$ further data are shown in table 4.3

^e new crater, not present in Galluzzi et al. (2015)

Average dislocation results of the 15 analysed faulted craters on Mercury (Galluzzi *et al.*, 2015), plus one new crater (16-L, this work). The craters are referred to numerically from 01 to 16 and associated with capital letters from A to L representing the corresponding eleven faults. Column Δx shows the measured slip horizontal component. Column Δh shows the average slip vertical component. Column n shows the number of profiles drawn on each crater to obtain the average Δh result. Fault strike was measured using the right-hand rule, and the slip trend indicates the direction of hanging-wall motion. Column δ shows the calculated true dip angles. The angle between the slip trend and the fault strike φ is also indicated. Column λ displays the rake values that were calculated on the footwall side of the fault from the strike direction to the slip vector, using the Aki & Richards (2002) convention. Each parameter is also associated with its calculated standard deviation σ .

4.2.2. H2 faulted craters

Listed in table 4.2 there are 5 faulted craters located inside H2 quadrangle: 01–A, 02–A, 03–A (Fig. 4.22a), 04–B (Fig. 4.22e), 05–C (Fig. 4.22f) and 13–I (Fig. 4.22d). In addition to these craters presented in Galluzzi *et al.*, (2015), a sixth crater was considered. This crater was named 16–L and is located north of Holbein crater and east of Endeavour Rupes, thus it can help to further analyse the Victoria system. In figure 4.23 a detailed view of H2 faulted craters is presented.

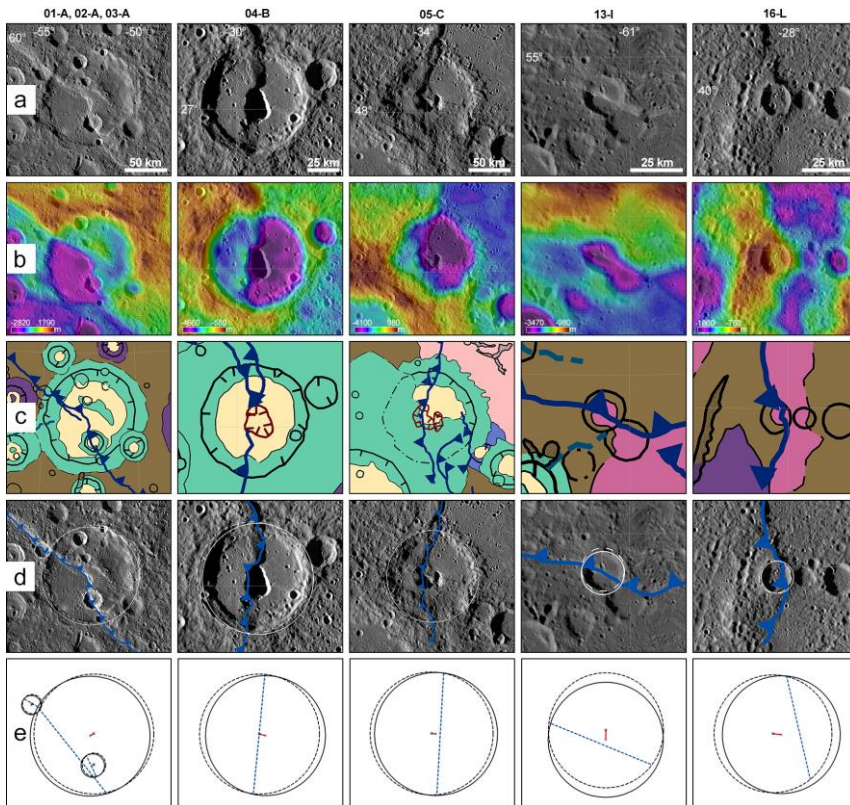


Figure 4.23. H2 faulted craters divided per columns (see labels at the top). Each line shows different analyzable layers. (a) BDR basemap (166 mpp) with indicated scale bar and coordinates for lines (a) to (d). (b) stereo-DTM by Preusker *et al.* (2011) with colour coding scaled to the view extent. (c) geologic map (this work, refer to figure 4.5 for legend). (d) BDR basemap with indicated thrust (blue line, triangles are toward the hangingwall) and circles for hangingwall (solid white line) and footwall (dashed white line). (e) A detail of built circles, refer to table 4.2 for crater diameters, strike and trend data.

Craters 01–A to 03–A, although cross-cut by the same fault, provide a different estimate of the true dip angle, ranging from 31° to 53° . Although some error certainly arises from the limited size of craters 02–A and 03–A when compared with crater 01–A, the main discrepancy might result from the different age of the three craters in relation to fault activity. The two smaller craters clearly formed after the larger crater, 01–A (Duccio). Following Melosh & McKinnon (1988), who argue that lobate scarps formed after the emplacement of large craters during the Late Heavy Bombardment (LHB) period, it is possible to hypothesize that the fault formed after the imposition of crater 01–A. On the other hand, the Δx measurements show a dislocation of crater 01–A about three times larger than that recorded by craters 02–A and 03–A; on this basis, it is possible to argue that the fault was already active before the formation of craters 02–A and 03–A. Because of their limited size, the younger craters probably did not totally erase the pre-existing fault scarp during the impact. The hypothesized scenario would lead to a vertical offset measurement across 02–A and 03–A that is higher than the actual Δh caused by the fault motion. This would explain the observed steeper dip when compared with crater 01–A. For this reason, although craters 02–A and 03–A are still useful for evaluating the history of incremental shortening, the data obtained from Duccio crater are a more accurate estimate of the finite fault displacement. Hence, thanks to the results obtained from this crater, Carnegie Rupes is an almost pure dip-slip thrust (*i.e.* rake $\sim 83^\circ$), dipping $\sim 31^\circ$ NE. The small crater 13–I returns an almost dip-slip motion as well (*i.e.* rake $\sim 111^\circ$) but a lower dip angle, 12° NE.

Craters 04–B (Geddes, Fig. 4.22e) and 05–C (Fig. 4.22f) are located at the same longitude and are cut by faults grouped into the same N–S-trending fault array VS–2 (see chapter 4.1.3). Nevertheless, since they are spaced ~ 900 km from each other, the individual fault segments that cut them were labelled differently (B on VS–2c, and C on VS–2a). This is consistent with the existing nomenclature that places the two craters on separate features (Geddes crater, 04–B on Antoniadi Dorsum and the unnamed crater 05–C on Victoria Rupes), which are evidently part of the same thrust system (*i.e.* the “Victoria system”, see chapter 4.1.3). The similarity between the two fault segments is marked not only by their strike (N 183° and N 185° ; Table 4.2), but also by the derived dip, trend and rake. Craters 04–B and 05–C indicate that the VS–1 array has a dip of $15\text{--}20^\circ$ and near dip-slip kinematics (Tab. 4.2).

The newly added crater 16-L is located between 04-B and 05-C giving results for the missing “Endeavour sector”, VS-2b. Despite its small size, the derived data show a 20° dip and near dip-slip kinematics (Tab. 4.2) and confirms the derived kinematics of the entire VS-2 array.

Detailed data for the most significant H2 faulted craters are shown in table 4.3, where all measurements and derived values are presented (n measurements for each crater as shown in table 4.2).

Table 4.3. Dislocation data of H2 faulted craters.

Name	Δx (km)	Δh (km)	ζ	trend	strike	φ	δ	λ	D (km)
01-A	4.14	2.22	28 °	241 °	323 °	82 °	28 °	83 °	4.70
01-A	"	2.74	34 °	"	"	"	34 °	83 °	4.97
01-A	"	2.29	29 °	"	"	"	29 °	83 °	4.73
01-A	"	2.48	31 °	"	"	"	31 °	83 °	4.83
01-A	"	2.68	33 °	"	"	"	33 °	83 °	4.93
01-A	"	2.16	28 °	"	"	"	28 °	83 °	4.67
04-B	4.52	0.86	11 °	104 °	185 °	81 °	11 °	81 °	4.61
04-B	"	1.29	16 °	"	"	"	16 °	81 °	4.71
04-B	"	1.07	13 °	"	"	"	13 °	81 °	4.65
04-B	"	1.32	16 °	"	"	"	16 °	81 °	4.71
05-C	3.96	1.47	20 °	96 °	183 °	87 °	20 °	90 °	4.22
05-C	"	1.20	17 °	"	"	"	17 °	89 °	4.13
05-C	"	1.59	22 °	"	"	"	22 °	93 °	4.26
16-L	1.08	0.35	18 °	96 °	167 °	71 °	19 °	72 °	1.13
16-L	"	0.40	20 °	"	"	"	21 °	72 °	1.15
16-L	"	0.41	21 °	"	"	"	22 °	72 °	1.15

Refer to table 4.2 for average data error estimates.

Figure 4.24 summarizes the data presented in table 4.3 with stereo-plots located on top of each studied fault.

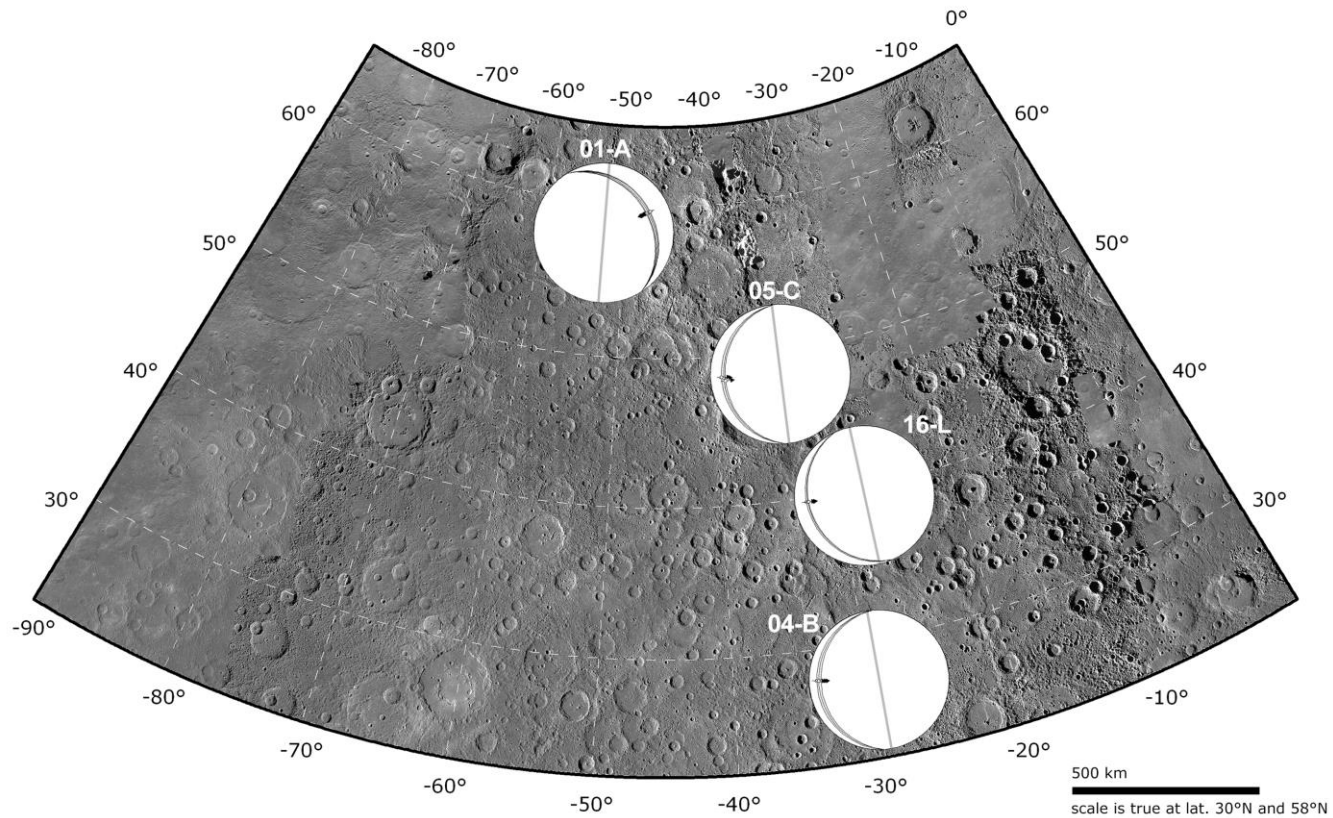


Figure 4.24. Stereo-plots for the most significant thrusts cross-cutting craters inside H2 quadrangle on H2-Bm-2 basemap (MDIS v8, 250 mpp). Each stereo-plot was built with the data in table 4.3. They are placed on top of the studied craters and rotated so that the grey lines are parallel to the meridians.

Uncertainties and error discussion

An analysis of the uncertainties on the derived parameters (plunge, ϕ , dip, rake and amount of displacement) starts from errors and uncertainties on the measured data (Δx , trend, Δh and strike; from now on called also input parameters). Since the input parameters come from different sources and this approach is based on a mix of different types of data, including images and DTM (and their associated uncertainties), a detailed error analysis is not an immediate task. For this reason, the analysis of each input parameter deserves a dedicated discussion.

The method used to measure Δx is a mixture of quantitative data derived from image features and qualitative image interpretation. A source of error comes both from the subjectivity in crater rim fitting and shifting, and from image resolution, linked to ground pixel size and other optical parameters. Systematic errors due to subjective interpretation are difficult to estimate and depend on many factors. An empiric approach is repeating the measurement of the same features several times and by different users with a comparable background and experience of geologic mapping, so that an average value and an associated uncertainty can be derived. Based on a test performed with three different mappers, it is possible to associate a standard deviation of about 10% of the measured Δx . It has to be stressed that in this dataset craters with uncertainties due to highly irregular or unrecognisable edges are already excluded. So far as the uncertainty originated by image resolution is concerned, the ground pixel size is normally between 150 and 250 m. Despite this, the measurement is derived by fitting a feature that involves many pixels. This means that the overall position error is negligible with respect to other error sources, as it is estimated to be well below one pixel. The slip trend is strictly connected to the Δx parameter, since they both describe the vector connecting the two circle centres (*i.e.* vector orientation and magnitude, respectively). Therefore, it is affected by similar uncertainties and by applying the same approach as before (*i.e.* repeated measurements) an uncertainty of about 15° was estimated.

The DTM derived parameter, Δh is measured as a difference in DTM elevation between two points, being the measurement repeated on different sections whenever the crater morphology allows it. Uncertainties in Δh are then determined by DTM errors and

measurement variability from different profiles. Preusker *et al.* (2011) estimated a standard deviation of 135 m on the stereo-derived DTM when compared with MESSENGER Laser Altimeter (MLA) data, to which a much higher accuracy is attributed. This value was derived from MLA binning within a running 15-km-long box, which gives an indication of the "effective resolution" of the DTM. Although taking into account craters smaller than 15 km was avoided, the remaining craters were analysed using the DTM at its higher spatial resolution (1 km). On the other hand, I am not interested in an absolute error, but in the relative elevation error between points that are relatively close to each other (16 to 110 km) and a better accuracy is expected in this case.

In order to account for the local variability in crater rim elevations, whenever possible (*e.g.* large craters, data availability) Δh was estimated along different profiles. In these cases the average and the standard deviation are derived as Δh and its associated uncertainty, respectively.

Finally, Zuber *et al.* (2012) found long wavelength features in surface elevations, the origin of which still remains unclear (Byrne *et al.*, 2014). These oscillations are up to 3 km in amplitude and have wavelengths of ~ 1200 km. In the worst case, it is possible to expect a contribution up to ~ 300 m in a 100 km-wide crater. I do not consider these oscillations to have a meaningful effect on these measurements as it is possible to argue that, for largest craters (> 50 km), the impact completely reset the local topography and for the smallest craters (< 50 km) the offset due to an underlying shallow slope is negligible. In any case, craters embedded in complex local topography were excluded from the dataset.

Based on the above discussion, a maximum value of between 135 m (from DTM uncertainty) and the standard deviation computed from the repeated measurements of each crater is attributed to the standard deviation of each Δh (Tab. 4.2). The strike measurement is similar to the slip trend, being an angular measurement of the line linking the intersections between the fault and the crater rim. The variability of multiple measurements in this case is very low, bringing a typical standard deviation of 1° . Taking into account the above mentioned sources of uncertainty, the uncertainties in the derived fault parameters were computed by propagating the errors through the standard

approach used for statistical errors. Most of the derived parameters (plunge, φ , dip, rake) show statistical uncertainties between $< 10\%$ and 40% . The worst cases refer to the highest relative errors on Δh associated with the smallest displacement vertical components (*i.e.* smallest craters). In particular, the propagated error on the displacement magnitude D is between 10% and 58% (Tab. 4.2). Moreover, the D parameter is subject to uncertainties arising from the relative age of the crater with respect to the fault activity. The value of $D \pm \sigma D$ can either correspond to the total amount of displacement registered by the fault or, if the fault partly acted before the emplacement of the crater, to a minimum amount of displacement registered by the crater since the time of the impact. These considerations strongly affect the Δx parameter, which can be at its maximum in the first case, or at minimum in the second case. Finally, since the D parameter depends also on Δh (*i.e.* equations (3) and (4), chapter 3.2.4), it is important to carefully consider the crater size. Pre-existing scarps can be erased by large impacts, but this might not be the same for smaller impacts: this issue affects Δh and all its derived parameters, as already demonstrated by the example of craters 02–A and 03–A.

5. Discussion

5.1. Structural analysis of H2 quadrangle

The tectonic fabrics hierarchy (*i.e.* systems, arrays, sectors, segments) adopted in chapter 4.1.3 has permitted a systematic analysis of the structural framework of H2 quadrangle. A brief summary of the main findings is given here with the aim of placing constraints and open issues for a discussion.

Based on consistency in strike, alignment and distribution, it was possible to recognise three main fault systems (Fig. 5.1)

- 1) *Victoria system*, formed by N–S trending fault arrays;
- 2) *Carnegie system*, formed by NW–SE trending fault arrays;
- 3) *Larrocha system*, formed by NE–SW trending fault arrays.

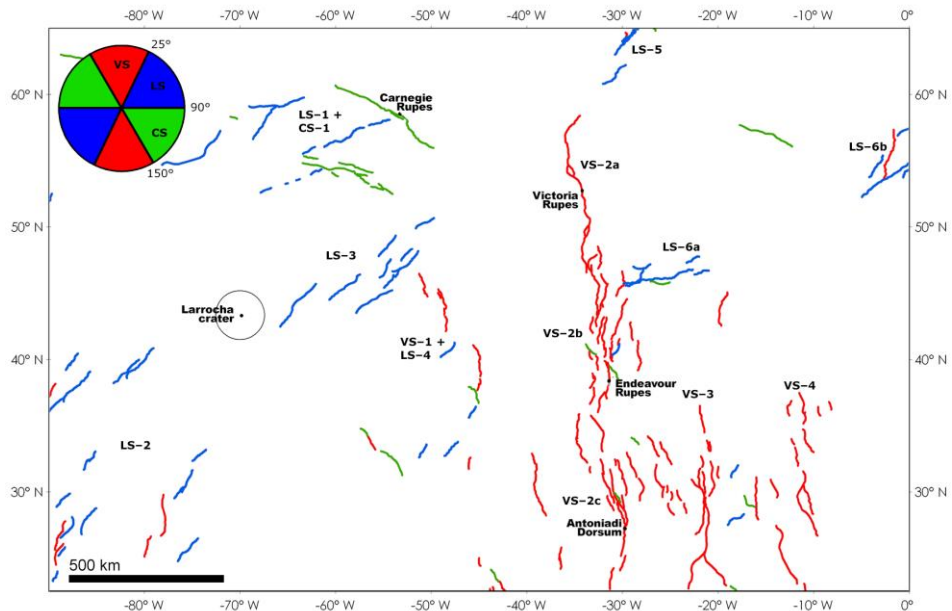


Figure 5.1. Summary of the individuated fault systems and sectors as analysed in chapter 4.1.3. The circle to the upper-left shows the system strike ranges: red, Victoria system; blue, Larrocha system; green, Carnegie system.

The subdivision into arrays and sectors highlighted the following main evidence:

- a) VS is the most prominent and developed system and is concentrated in the central-eastern area of H2 quadrangle. Its main array, VS-2 ($\sim 32^\circ$ W) varies its segmentation from north to south, starting from the single segment of Victoria Rupes sector (VS-2a), passing by the widely-segmented area of Endeavour Rupes sector (VS-2b), and ending with the lozenge-shaped segmented-area of Antoniadi Dorsum sector (VS-2c);
- b) While VS segmentation continues to the east of VS-2b and VS-2c with arrays VS-3 and VS-4, no fault arrays are found east of VS-2a (*i.e.* in the northern smooth plains region);
- c) LS is mostly developed in the western area of H2 quadrangle;
- d) CS is characterised by few, but long, faults and is concentrated in the north-western area of H2 quadrangle, where it alternates with the LS-1 array in a 30° “net” of fault segments;
- e) A more than 400 km wide, fault-free area divides LS+CS from VS in the central part of the quadrangle. In particular, LS is interrupted by the fault-free gap and re-surfaces to the east with few smooth plains-bounding faults.

5.1.1. Fault system interaction and fault segmentation analysis

Although single systems and arrays are relatively well separated, few short segments belonging to a different system are often observed within most arrays. These oblique segments pertaining to a different system are located, within each array, at the transition between sectors. A possible explanation for the segments with strike oblique or quasi-orthogonal to that of the array they are located in (figures 4.9, 4.12 and 4.13) is that they accommodate the transition between main sectors or segments in a manner similar to the relay ramps observed in terrestrial fault systems. For instance, some of the scattered CS and LS oblique segments are located within VS-2, VS-3 and VS-4 arrays and the same happens for some VS scattered segments inside LS-2 array. Insofar as they mark the transition between sectors within arrays, these small segments must be considered as part of the arrays in which they are found, and not as members of a different system.

Alternatively, they could be viewed as part of a different, maybe older system, which has been exploited as segment boundary in the array they are presently located.

The more detailed segmentation analysis within H2 quadrangle can be performed on the VS-2 array, as shown in figure 5.2. This array has been interpreted as a fold-and-thrust belt by Byrne *et al.* (2014) similar to those found on Earth (Poblet & Lisle, 2011) and Venus (Burke *et al.*, 1984). Although some differences exist between Byrne *et al.*'s structural mapping and the linework of this thesis (attributable to a different interpretation of the basemap layers), the vergence and distribution of the most prominent thrust segments is consistent between the two works. Moreover, the method for deriving fault slip data of Galluzzi *et al.* (2015) allowed to gather quantitative data at three different locations along the array that, consequently, permitted derivation of a local stress inversion (Fig. 5.2) using all the measurements in table 4.3 (for a total of 10 measurements taken on craters 04-B, 05-C and 16-L). These inversion results confirm that the VS-2 is an almost pure thrust system accommodating an ~E-W shortening. The sector boundaries within the VS-2 array can be identified with a relatively good degree of confidence, because of the spatial coincidence with different geological features that may control the segmentation (Fig. 5.2). The northern tip of VS-2a is less than 30 km away from a pit bearing crater. To the south, the transition between VS-2a (*i.e.* Victoria Rupes single-fault sector) and VS-2b (*i.e.* Endeavour Rupes highly-segmented sector) is in correspondence of the pit bearing crater here called 05-C (see Fig. 4.10a). Further south, the passage between VS-2b and VS-2c is characterized by an increase in fault segments length and a narrowing of the fault zone. I surmise that transition is related to Holbein impact that buried a faulted zone east of Endeavour Rupes (Fig. 5.2). It is possible that Holbein impact happened right at the end VS faulting, thus being a syntectonic impact (see arrows in Fig. 5.2a). However, Holbein ejecta are in turn cut by a VS-2c segment (which is why this crater was not considered in the buffered crater counting of chapter 4.1.4), and thus fault motion of a possibly reorganized fault array slightly continued also after Holbein impact.

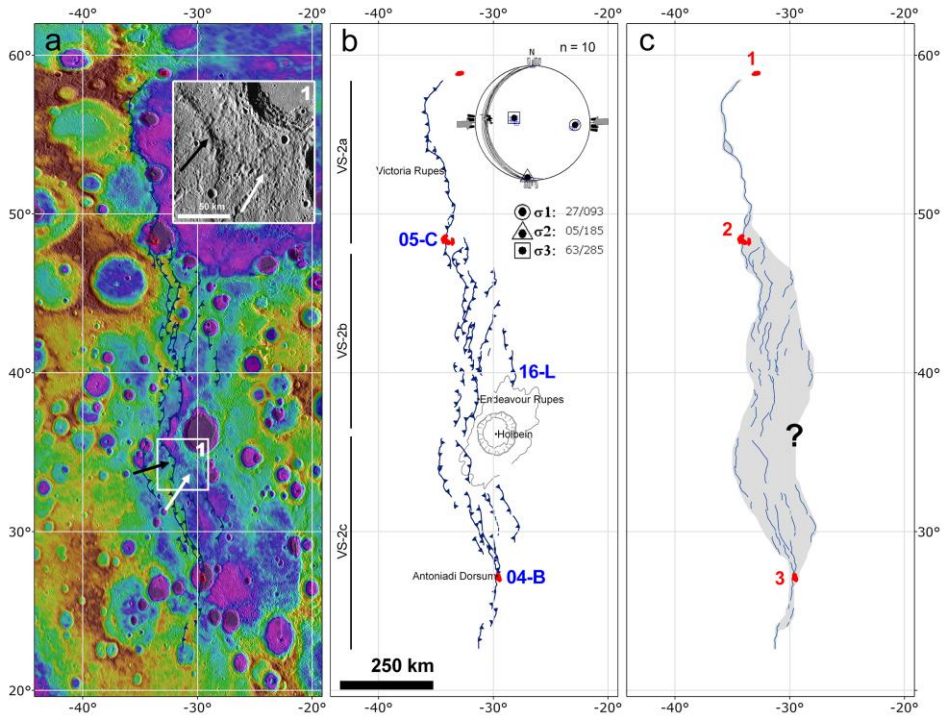


Figure 5.2. Representation of Victoria system VS-2 array in equirectangular projection centred on H2 quadrangle. (a) stereo-topography (Preusker *et al.*, 2011); in inset (1) the white arrow indicates a topographic relief buried by Holbein crater ejecta and the black arrow indicates a topographic relief corresponding to a thrust segment cutting Holbein ejecta. (b) structural scheme of VS-2 array: red polygons represent irregular pit locations; blue lines are thrusts with triangle laying on the footwall; grey contacts indicate Holbein crater main boundaries (from the geologic map, this work); to the left VS-2 sectors are indicated; to the upper-right a stereo-plot shows the kinematic axis (blue circles, squares and triangles) and the average finite stress axes (black circle, square and triangle) for VS-2 array derived from data of craters 04-B, 05-C and 16-L in table 4.3 (blue labels). (c) simplified structural scheme showing a grey area that highlights a lozenge-shaped fractured area between VS-2b and VS-2c. The question mark stands on Holbein crater location indicating an uncertain region with probably buried thrust segments. Irregular pits are marked with a red number: pit 1 (see Goudge *et al.*, 2014) stands at the northern tip of VS-2a sector; pit 2 (see Kerber *et al.*, 2011) stands at the cornerstone between VS-2a and VS-2b sectors; pit 3 (see Kerber *et al.*, 2011) stands on the point where VS-2c narrows and abruptly decreases its segmentation.

Finally, another pit bearing crater, Geddes, (also called 04-B in the faulted crater analysis, see Fig. 4.10c), marks an abrupt narrowing of sector VS-2c which heralds the end of the whole VS-2 array.

The presence, along the VS-2 array, of these pits, interpreted as volcanic vents by Kerber *et al.* (2011), is probably linked to the presence of faults, as also stressed by

Thomas *et al.* (2014b) and Rothery *et al.* (2014) in other regions of Mercury. However, the finding that these volcanic vents are located in correspondence of the VS–2 sectors “cornerstones”, may suggest an even tighter relationship between volcanic activity and fault segmentation along this array. In this view, vents not only were controlled by fault motion, but also acted to organize the segmentation between sectors within arrays, possibly in a later stage of fault activity.

Another interesting case of tectonic control on the map distribution of geological units is observed at the VS–2a and VS–2b boundary. Here, to the east of pit bearing crater 05–C, a LS segment, visible in figure 4.15, a NE–SW striking fault segment bounds to the south the northern smooth plains region. To the south of this segment a wide faulted zone composed of VS–3 and VS–4 arrays is present (Fig. 4.11). To the north of this segment, thus to the east of Victoria Rupes, no intense faulting of VS segments is observed. Thus, it may be the case that the NE–SW striking faults (pertaining to LS–6 array, Fig. 4.15) controlled the smooth plains flow, which, in turn, may have buried pre-existing VS and/or LS segments to the north.

Considering this last described fault framework, it is possible that pits formed at the intersection of the two main fault systems VS and LS. This occurrence is quite common on Earth, where relevant upwelling processes (*e.g.* volcanoes, geothermal fluids and vents) usually happen in correspondence of fault intersections (*e.g.* Acocella & Funicello, 2006). In this view LS–6a should act as a relay zone between the younger VS arrays. Further analysis on fault timing is made in chapter 5.1.3,

Another example of fault system interaction is represented by arrays LS–1 and CS–1, whose segments intersect each other at 30° angles, reminiscent of the mid-latitude tidal despinning pattern described by Melosh, 1977. Nevertheless, data gathered on Carnegie Rupes through the cross-cut Duccio crater, reveal a near dip-slip motion (*i.e.* $83 \pm 10^\circ$, table 4.2), conflicting with the lateral motion that would be expected with a tidal despinning model. Despite this, Dombard & Hauck (2008) hypothesised that tidal despinning forces ceased just before the LHB period since there is a lack of latitudinal patterns in the distribution of lobate scarps, but the post-LHB global contraction may have re-activated old despinning structures, inheriting their orientation. However, the observed pattern is not continuous and is limited to the LS–1 and CS–1 area, where the

LS–1 faults are inferred from slight topographic changes that do not permit further speculation on their origin.

5.1.2. The Victoria tectonic bulge

Between Carnegie Rupes and Victoria Rupes, a broad topographic ridge is present (Fig. 5.3). Although the relief-bounding faults (some segments have been called high-terrain-bounding faults by Byrne *et al.*, 2014, based on their significant elevation offset) have been preliminary assigned, based on their trend, to two different systems (CS–1 and VS–2 arrays, respectively), I further refine this view and propose that the NW–SE striking segments of CS–1 could be an oblique part of the VS–2 array, and thus be part of the same system. Hence, the high-terrain area would represent a regional pop-up grown between the two kinematically-linked arrays.

Under this hypothesis, kinematic data derived from 01–A crater (*i.e.* Duccio) can be added to the stress inversion for the VS. With this addition, the finite shortening axis for the combined Victoria – Carnegie system (seen as part of a single and kinematically linked system) trends 71° (Fig. 5.3) instead of 93° (Fig. 5.2b). The result of the modified stress inversion is more consistent, compared to the previous inversion, with the trend of the topographic bulge crossing the whole central part of the quadrangle, which is bounded by VS–2a faults and Carnegie Rupes to the north and by VS–1 and VS–2b plus VS–2c faults to the south. Note that the main central topographic relief also corresponds to the fault-free gap between LS and VS systems.

In summary, structural and fault kinematic evidence suggests that VS and CS fault arrays are part of a single displacement system formed by east-directed main thrusts and west-directed antithetic thrusts, that created the regional tectonic bulge. This interpretation would explain why the bulge has retained a structural coherence, as suggested by the lack of significant faults inside the high-relief area.

A similarly-striking, narrow and higher relief belt is observed to the east, in correspondence of VS–4 array, but no quantitative kinematic analysis is available in this area.

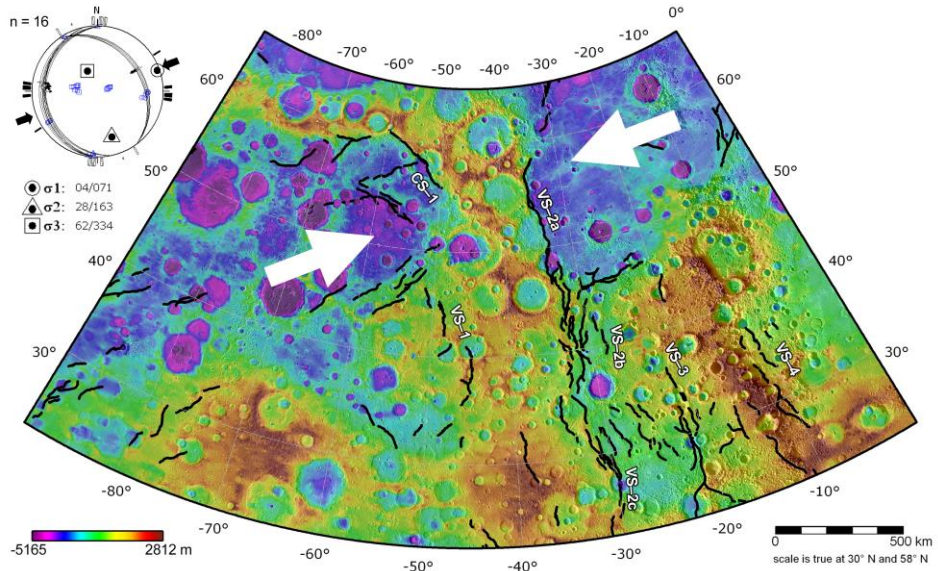


Figure 5.3. MLA topography with mapped contractional faults (black lines). To the upper left, a stereo-plot showing stress inversion results derived from craters 01-A, 04-B, 05-C and 16-L in table 4.3 is reported. Blue circles, squares and triangles represent the kinematic axes. The resulting average stress inversion is reported in the legend with dip/trend data for each stress axis (σ_1 –3). Arrows trend, 71° N, is reported also on the topographic map (white arrows). Sectors involved in the bulge are reported on the figure.

Evidence from independent datasets

A trend similar to that of the topographic relief is visible in the maps from Smith *et al.* (2012) showing Mercury’s free-air gravity anomaly and crustal thickness. The maps shown in figure 5.4 were derived re-projecting and georeferencing Smith *et al.* (2012) figures in order to fit Victoria quadrangle. In figure 5.4a, a positive anomaly is aligned with the fault-free central topographic bulge. In figure 5.4b, the crustal thickness is larger along the same bulge, following a similar trend. This evidence might suggest the presence of deep crustal discontinuities that controlled the N–S alignment of the Victoria system.

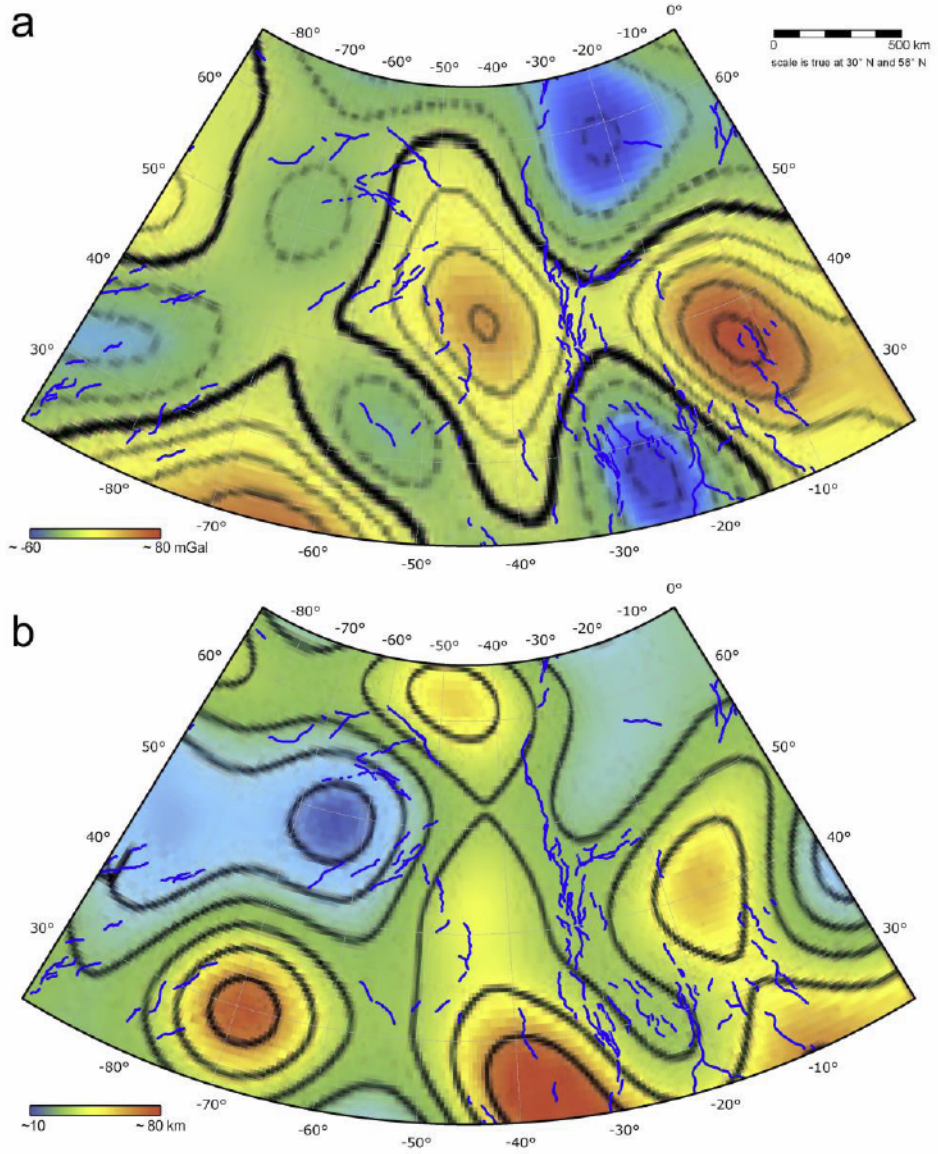


Figure 5.4. Modified and re-projected H2 detail of Mercury's maps from Smith *et al.* (2012). Scale bars are approximated from the original global scale bars. (a) Free-air gravity anomaly. (b) Crustal thickness.

5.1.3. Timing of fault activity

In chapter 4.1.4, the buffered crater counting provided evidence suggesting a young relative age of the Victoria system. This inference is also supported by the relationship between Victoria Rupes and the northern smooth plains, which are cut by this thrust (Fig. 5.5). However, it is likely that the Victoria Rupes thrust also served as a topographic barrier for the smooth plains. This means that syndepositional tectonics occurred during emplacement of the smooth plains flow, which could have led to burying of pre-existing thrust segments to the east of Victoria Rupes.

Since in the previous paragraphs it was proposed that Carnegie system must have acted as an oblique antithetic element of the Victoria thrust system, the two fault systems should be regarded as coeval.

In the case of the Larrocha system, unfortunately it was not possible to retrieve a statistically significant relative age. However, some speculations can be made based on morphological evidence and on its relationship with the other systems:

a) LS is defined mainly by faults that cause subtle topographic changes, they are difficult to identify and must be often inferred from the comparison between several basemaps and topography. This is consistent with the analysis of Byrne *et al.* (2014), who map few NE–SW contractional faults in this area and do not distinguish any high-terrain-bounding fault among them.

b) LS is principally developed to the west, and only a few segments can be found east of the central tectonic bulge. These eastern segments define the southern smooth plains contact.

From these two observations it is possible to speculate that: a) LS is composed of more degraded faults than VS ones; b) LS was erased by the prominent VS faults that interrupt the continuity of this system in the central part of the quadrangle. Hence, it is proposed that the Larrocha system is older than the Victoria system.

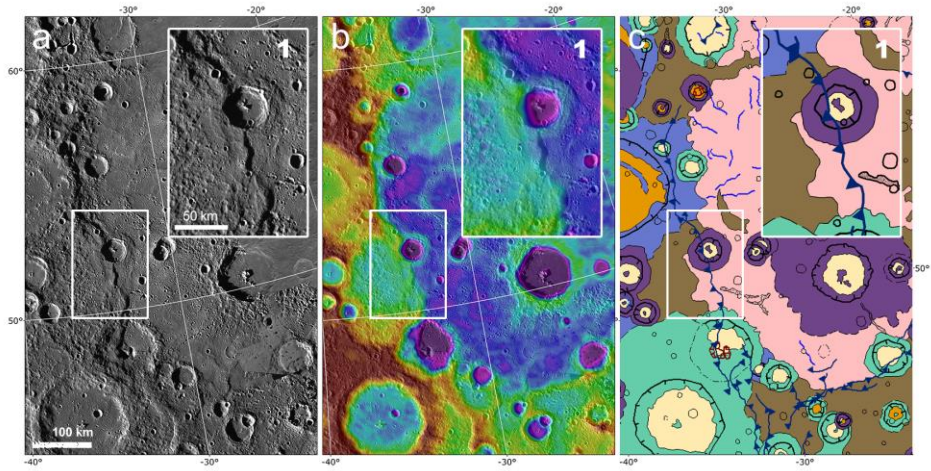


Figure 5.5. Detail of a smooth plains region within H2 quadrangle, where Victoria Rupes cuts (inset 1) this unit, but also constitutes its boundary because of the high topographic relief generated by VS thrust array. (a) MDIS complete mosaic (250 mpp). (b) MLA topography. (c) Geologic map (this work, refer to figure 4.5 for colour legend).

5.2. Structural analysis at semi-global scale

Several authors have proposed general relationships between fault orientation and kinematics, and their latitudinal distribution on Mercury. Melosh (1977) argued that on a despun planet, N–S oriented thrusts at low latitudes, NW–SE and NE–SW strike-slip faults at mid-latitudes and E–W normal faults at high latitudes should be found. The tidal despinning model was refined for Mercury by Pechmann & Melosh (1979) and subsequently by Matsuyama & Nimmo (2009), who proposed a wider distribution of thrusts even at higher latitudes. These models directly, albeit qualitatively, correlate fault strikes and slip with their geographical position.

The distribution of thrusts due to the proposed tectonic models varies from the total randomness predicted by the global contraction due to core solidification, to the precise latitudinal variations expected by the tidal despinning model. In principle, it should be possible to verify proposed models by crosschecking fault parameters retrieved in this work with their global distribution. However, given the wide distribution and high number of lobate scarps present on the surface of Mercury (*e.g.* Byrne *et al.*, 2014), the 12 analysed thrusts are too few to be representative for global scale tectonic interpretation. Despite this, the original dataset may still provide quantitative kinematic constraints and constitute a general frame for future analyses when more data become available.

5.2.1. Relation between fault geometric and kinematic parameters

The cumulative data relationships between geometric and kinematic fault parameters provided by the offset craters analysis are presented in the diagrams of figures 5.6 to 5.9. Since I did not find craters cut by normal faults, the diagrams show only positive rake values (convention by Aki & Richards, 2002) and are divided, according to the fault parameters, into fields that range from dip-slip reverse to right- and left-lateral strike-slip faults, passing through the different reverse oblique-slip faults.

Figure 5.6 illustrates the relation between dip on the x -axis and rake on the y -axis. To better illustrate the expected trend, I have traced on the diagram a parabolic curve that encompasses, in a qualitative manner, the plotted measurements. The curve was built considering two end-member cases: a horizontal pure dip-slip thrust and a vertical pure

strike-slip fault, assuming homogeneous plane strain conditions. Thus, it intercepts the dip axis at $(90^\circ; 0^\circ)$ and its vertex stands on $(0^\circ; 90^\circ)$, being its formula $x = (1/90)y^2 - 2y + 90$. This parabola qualitatively illustrates the predicted pattern for the dip – rake data, spreading from shallow dips and near dip-slip rakes of the reverse faults field, to steeper dips and oblique-slip rakes toward the strike-slip faults field. The relationship outlined by the arbitrarily chosen parabolic curve apparently holds for both larger and smaller (and younger) craters, and is valid from H2 quadrangle to a semi-global scale.

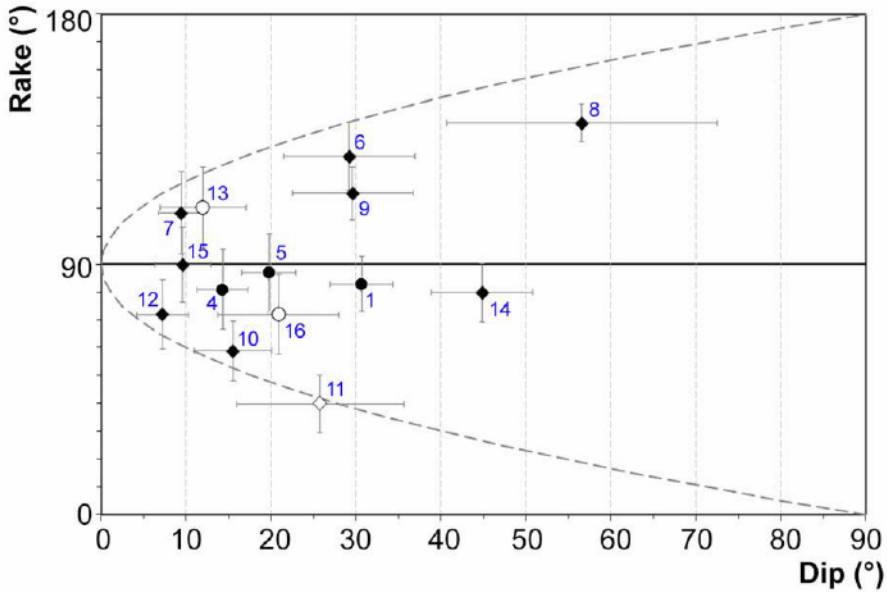


Figure 5.6. Dip-rake diagram for the data in table 4.2; for fault 'A', only data from crater 01-A were considered. The blue numbers correspond to faulted crater number. The error bars represent the standard deviations of dip and rake in table 4.2. The dashed parabola qualitatively encloses the expected trend. Data deriving from H2 faulted craters are represented by a circle instead of a diamond. Empty diamonds and circle indicate data derived from smaller craters.

In figure 5.7, fault strikes (x -axis) are plotted against fault rake (y -axis) to compare the azimuth of faults and their kinematics. Here and in the following diagrams fault "F" (*i.e.* Enterprise Rupes) is considered as represented by its centremost crater 09-F and therefore I avoided plotting the results from craters 08-F and 10-F (Fig. 4.22b). Unlike the dip – rake plot, which follows generally expected trends as observed on earth, and follows basic rules of crustal rheology, the strike-rake diagram for Mercury should

show no particular trend in case of a random processes like global contraction, or alternatively should show a modulated distribution in case of the tidal despinning model. In a pure global contraction model, the curve should be flat in the thrust field (i.e. pure dip-slip thrusts with random strikes). The grey areas in figure 5.7 were placed to help recognising the location where pure tidal despinning structures should be expected. The superposition of global contraction and an hypothetical re-activation of tidal despinning faults (e.g. Dombard & Hauck 2008) should have shifted rakes toward the thrust region. The resulting plot shows that some faults striking N–S to ~NNW–SSE cluster near dip-slip rake angles and thus are almost pure dip-slip thrusts (Fig. 5.7). On the other hand, faults striking increasingly toward the E–W direction have a progressive shift toward moderate strike-slip rake angles and thus are oblique-reverse faults. One of the two younger and smaller craters apparently follows the trend of the older craters. Faults cross-cutting craters 09–F and 12–H have compatible strikes with the tidal despinning model, and their oblique rake (*i.e.* neither pure dip-slip, nor pure strike-slip) might suggest that a gradual shift toward the thrust field occurred. Thus these data cautiously convey that the old tidal despinning fabrics can still be discerned within the younger superposition of global contraction. However, the distribution of 11–G and 06–D, which record the highest oblique-slip motion, is outside the hypothesised trends, suggesting that other processes that allow the presence of oblique-slip motion may complicate the faulting pattern.

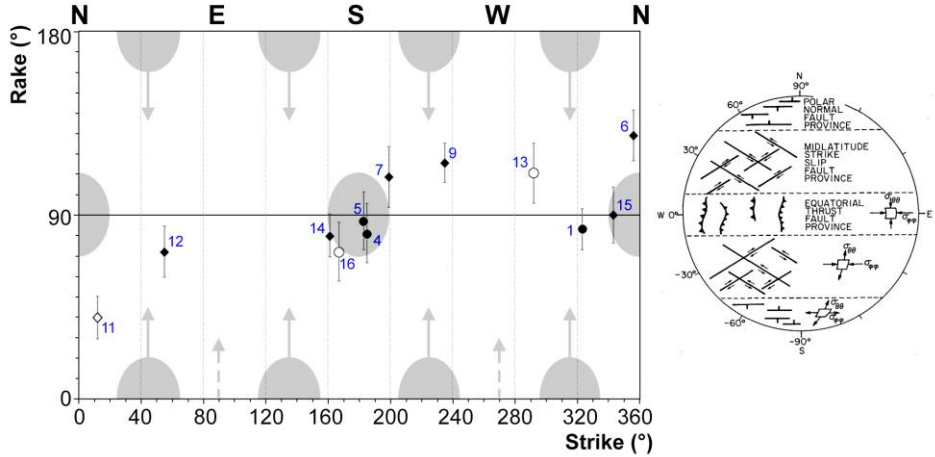


Figure 5.7. Strike-rake diagram for the 12 analysed lobate scarps (data from table 4.2). The blue numbers correspond to faulted crater number. The error bars represent rake standard deviation in table 4.2. In the upper part of the diagram, cardinal points are also indicated. Strikes are measured with the right-hand rule so that faults striking east or west lie in the same direction but dip in opposite directions (south and north, respectively); the same applies for faults striking north and south that dip east and west, respectively. Data deriving from H2 faulted craters are represented by a circle instead of a diamond. Empty diamonds and circle indicate data derived from smaller craters. The grey areas represent the expected approximate locations of pure tidal despinning structures as predicted by Melosh (1977) model, reported to the right. Grey arrows represent an hypothetical shift toward the thrust region due to fault re-activation (e.g. Dombard & Hauck, 2008). Since this diagram shows only positive rakes, the dashed arrows represent the shift toward the thrust region from the E-W tidal despinning normal faults (that for Aki & Richards, 2002, convention have negative rakes, thus are not displayed on this diagram).

More insights on the existence of global tectonic patterns can be gathered by analysing fault parameters with respect to fault location. In figure 5.8, fault dips (x -axis) are plotted against fault latitude (y -axis). This representation portrays how fault dips change throughout the analysed latitudinal range (from 40°S to 60°N). A speculation that can be derived from diagram in figure 5.8 is related to fault re-activation. If Dombard & Hauck (2008) theory on re-activation of tidal despinning faults is valid, it is reasonable to expect that re-activated faults inherited not only the strike, but also the dip of ancient tidal despinning structures. This means that at higher latitudes, where strike-slip faults are expected for the tidal despinning model, structures re-activated as thrusts should have a steeper dip than expected for a newly formed thrust. To help in this distinction, grey areas were placed on the expected latitude range of tidal despinning structures (*i.e.* for thrusts: 0° – ± 25° lat.; strike-slip faults: ± 25° – ± 55° lat.; normal faults: ± 55° – ±

90° lat.; Melosh, 1977; Melosh & McKinnon, 1988). These areas fade toward dip limits imposed by idealized Andersonian faulting (*i.e.* thrusts: $\sim 30^\circ$; normal faults: $\sim 45^\circ - \sim 60^\circ$; strike-slip faults: $\sim 60^\circ - 90^\circ$). As already forewarned by figure 5.6, it is evident also from this diagram that most of the analysed thrusts have lower dips than expected by Andersonian faulting. However, even if a shift toward shallower dips is present, dip angles of faults cross-cutting craters 01-A and 09-F are steeper and located at higher latitudes, while faults with low-angle dips are preferentially located at low latitudes. Unfortunately data are limited in number, but populating this diagram could provide further insights in Mercurian tectonics.

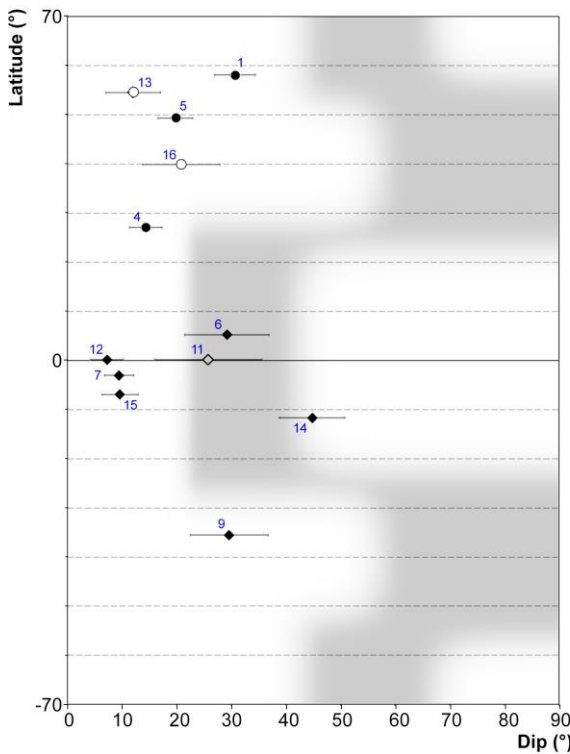


Figure 5.8. Dip-latitude diagram for the 12 analysed lobate scarps (data from table 4.2), showing fault true dip variations throughout the analysed latitudinal range. The blue number correspond to faulted crater number. The error bars represent dip standard deviation in table 4.2. Data deriving from H2 faulted craters are represented by a circle instead of a diamond. Empty diamonds and circle indicate data derived from smaller craters. The grey areas represent the latitudinal bands where tidal despinning faults should have occurred. They fade toward the nearby regions based on idealized Andersonian faulting (see text for details).

In figure 5.9 fault latitude (*x*-axis) is plotted against fault rake (*y*-axis). Here the representation of fault latitude is simplified by giving only its modulus value. This allows us a quicker visual inspection of rake changes with latitude (*i.e.* low-, mid- and high-latitudes). The diagram shows that near dip-slip thrusts are present at all latitudes, casting doubts on the validity of tidal despinning model, unless fault re-activation

(Dombard & Hauck, 2008) is considered. The dataset is not statistically significant to ascertain whether transpressive faults are widely distributed or latitudinally concentrated, but grey areas were placed on the expected tidal despinning latitudinal ranges as done for figure 5.8.

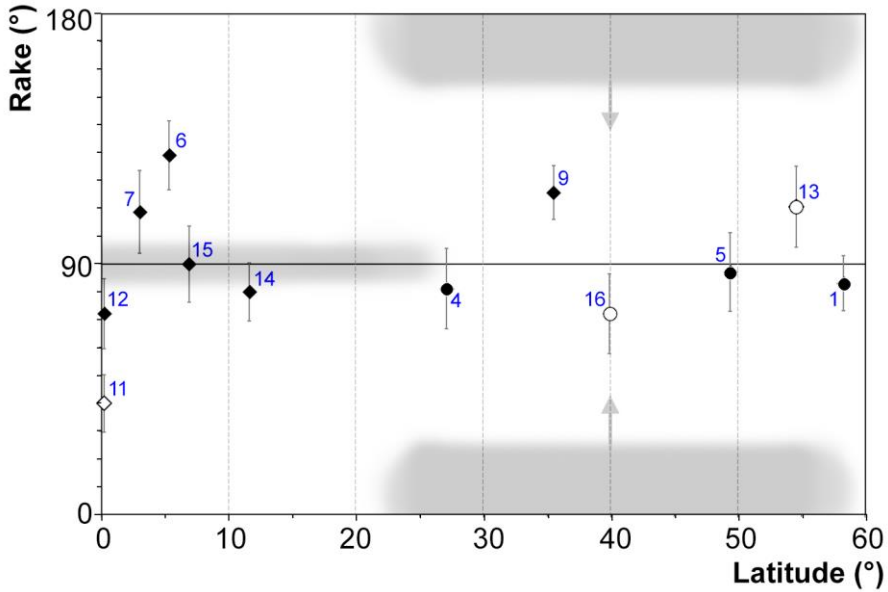


Figure 5.9. Latitude-rake diagram for the 12 analysed lobate scarps (data from table 4.2). All latitudes are shown as positive values, independent of the hemisphere. The blue number correspond to faulted crater number. The error bars represent rake standard deviation in table 4.2. Data deriving from H2 faulted craters are represented by a circle instead of a diamond. Empty diamonds and circle indicate data derived from smaller craters. The grey areas represent the latitudinal bands where tidal despinning faults should have occurred (see text for details). Grey arrows represent an hypothetical shift toward the dip-slip region due to fault re-activation (e.g. Dombard & Hauck, 2008).

Diagram in figure 5.9 highlights: (1) the compatibility of some craters (09–F, 13–I) with the shift toward the thrust region of hypothetical tidal despinning pre-existing strike-slip structures; (2) the “anomalous” distribution of other oblique-slip faults (06–D, 07–E). Considering what has been told for diagram in figure 5.7, it is clear once again that some faults, in particular the one cross-cutting crater 06–D, might elude both the global contraction and the tidal despinning expected trends. While 06–D strike, dip and latitude could be in accordance with a tidal despinning model, its rake is incompatible both with

tidal despinning and global contraction, suggesting that another process, *e.g.* mantle convection as proposed by King (2008), might have influenced the nucleation of oblique faults. This is in accordance with Massironi *et al.* (2015) who interpreted oblique structures analysed using Galluzzi *et al.* (2015) method, including the one cross-cutting 06-D, as thrust oblique or lateral ramps, concluding that, such structures are incompatible with a pure and isotropic global contraction model.

The data used for the proposed diagrams require further investigation since tens of faulted craters could not be analysed because of their limited size or complicated morphology. Hence, high resolution topography will be crucial to increase the available dataset and to study trends in fault parameters.

6. Summary and conclusions

6.1. Tectonics of Victoria quadrangle

The realization of the presented 1:3,000,000 geologic map offered a complete overview of H2 quadrangle of Mercury, and the gathered tectonic and kinematic results were extended to a semi-global scale to provide constraints on the validity of existing tectonic models of the planet. All the three main geologic provinces known on Mercury were found in the H2 quadrangle: smooth plains, intermediate plains and intercrater plains. The mapped smooth plains area is consistent with the mapping by Denevi *et al.* (2013). Although intermediate plains have been lately reclassified either as smooth plains or intercrater plains (Denevi *et al.*, 2013; Whitten *et al.*, 2014), mapping at a scale of 1:600:000 led me to re-introduce this unit within the mapped area due to evidence from superposition relationships.

As regards craters, I decided to use three crater degradation classes, C1 being the most degraded craters and C3 the freshest craters. This classification, simplified with respect to the official USGS classification (*i.e.* C1 to C5), was sufficient to demonstrate that: a) smooth plains are superposed only by C3 craters and b) intermediate plains are superposed by C3 and C2 craters; c) C1 craters superpose only intercrater plains. Almost 1800 craters > 5 km were mapped in the quadrangle and constituted the basis for a relative age determination through crater counting. Relative age results confirm that intermediate plains are older than smooth plains and younger than intercrater plains, although they present overlapping frequencies for craters < 15 km, which is in accordance with the findings by Whitten *et al.* (2014).

Within H2 quadrangle I distinguished three different types of contractional structures: wrinkle ridges, thrusts and other less prominent faults, largely of contractional nature. Thrusts were mapped in correspondence of the lobate scarps and high relief ridges. The less prominent contractional faults present a more rectilinear morphology and were often inferred from topography. Three main systems were identified and their orientation was statistically defined through rose-diagram analysis: the N–S Victoria system, the NW–SE Carnegie system and the NE–SW Larrocha system.

A detailed analysis based on a hierarchical segment subdivision, led to the conclusions that:

- 1) the Victoria – Antoniadi array, defined as a fold-and-thrust belt by Byrne *et al.* (2014), defines a central longitudinal tectonic bulge limited to the west by Carnegie Rupes and other Carnegie system east-dipping faults, which are inferred to be kinematically related and antithetical to the Victoria system faults;
- 2) the Victoria – Antoniadi array is characterised by the presence of pit craters (*i.e.* volcanic vents) defining three cornerstones along the array that correspond to systematic changes in fault zone segmentation, implying a strict relationship between volcanic activity and faulting in this area;
- 3) the Larrocha system faults are more degraded faults, interrupted by the H2 central bulge, thus probably they are older and were overprinted and obscured by the younger VS activity.

The young age of VS is confirmed both by morphological evidence and by the cumulative SFD obtained with the buffered crater counting method, which stands below the smooth plains cumulative SFD. This finding is in accordance with the absolute ages derived by Giacomini *et al.* (2015) on a different region of Mercury, Blossom Rupes (*i.e.* 3.5 to 3.7 Ga). However, Victoria Rupes both bounds and cuts smooth plains, implying a sin-depositional activity, as argued elsewhere on Mercury (*e.g.* Solomon *et al.* 2008; Watters *et al.*, 2009).

6.2. Fault slip analysis

The use of faulted craters as kinematic markers (as defined in Galluzzi *et al.*, 2015) can help in the quantitative study of planetary tectonics. Two main input parameters for the method illustrated in the quoted paper are the horizontal (Δx) and vertical (Δh) fault displacement components that can be measured from imagery and topography, respectively. When Δx and Δh are measured, the fault geometry and kinematics can be completely defined. Even if Δh is unknown (*i.e.* there is no available topography across the fault), Δx trend (*i.e.* slip trend) alone can yield information on the fault kinematics since the angle between fault strike and slip trend on the horizontal plane, ϕ is often

very similar to the rake angle λ calculated along the fault plane. The usefulness of this parameter was remarked by Massironi *et al.* (2015) that used it to assess the fault horizontal component of slip.

By applying this method on 16 faulted craters found across the 30% of Mercury's surface covered by flyby stereo-derived DTM (Preusker *et al.*, 2011), the results interestingly show that the derived fault dips are within a much wider range ($7^\circ < \delta < 57^\circ$) than the $30\text{--}35^\circ$ interval predicted by Watters *et al.* (2002). This could be explained by the fact that these data are obtained from direct measurements made on multiple faulted markers, rather than from a numerical fit of the geomorphic surface of a single lobate scarp (*i.e.* Discovery Rupes, Watters *et al.*, 2002), and therefore have the advantage of showing the natural variability inherent to fault geometry, possibly related to crustal rheological differences (*e.g.* faults forming within different lithologies). The calculated rake variability ($40^\circ < \lambda < 141^\circ$) denotes a large variety of thrust motions, and emphasizes that some of the reverse faults on Mercury are not pure dip-slip thrusts, as commonly expected. Thus, fault slip data were further analysed using dip-rake, strike-rake, dip-latitude and strike-latitude diagrams. When used together, these diagrams may help distinguishing faults re-activated by global contraction from tidal despinning pre-existing structures, from which they may have inherited the strike (Dombard & Hauk, 2008) but also the dip. These diagrams also revealed that some oblique-slip faults plot differently from tidal despinning or global contraction expected trends, suggesting that other processes such as mantle convection (*e.g.* King, 2008) had an important role in the tectonics of Mercury.

Seven out of the 16 studied craters are located within Victoria quadrangle, revealing that the Victoria – Antoniadi array dips from a minimum of $15^\circ \pm 3^\circ$ to a maximum of $20^\circ \pm 7^\circ$, while Carnegie Rupes dips $30^\circ \pm 3^\circ$. The most representative craters, located on Carnegie Rupes, Victoria Rupes, east of Endeavour Rupes and Antoniadi Dorsum, permitted calculation of the finite kinematic axis affecting the central tectonic bulge, which trends 71° E. Although affected by many uncertainties, this is the first attempt to calculate quantitative fault slip data and perform a stress inversion on a remotely sensed planetary surface.

6.3. Open issues and future work

Many questions raised from this work are still unsolved and require future investigations. One important issue relates to the very low dips of thrust faults resulting from the kinematic analysis of displaced craters. Idealized Andersonian thrust dips should be around $\sim 30^\circ$. The shallower dips observed for low-angle overthrusts is often the result of fluid overpressure (*e.g.* Hubbert & Rubey, 1959; McClay, 1992). No such mechanism can be documented on Mercury, but this planet certainly hides processes beneath the surface that caused the formation of hollows (*e.g.* Blewett *et al.*, 2011; Thomas *et al.*, 2014a) and vents (*e.g.* Kerber *et al.*, 2009, 2011; Rothery *et al.*, 2014; Thomas *et al.* 2014b) that were active for a long period of time (Thomas *et al.*, 2014c; Rothery *et al.*, 2014). Whereas the origin and growth of these features were aided by faults (Thomas *et al.*, 2014b), fault shallow dips might have been favoured by magmatic and volatile processes. Hence, this hypothesis needs further investigation.

The results obtained with the kinematic analysis have been limited by data coverage and resolution. However, faulted craters proved to be a useful tool for regional and global-scale tectonic interpretations (Galluzzi *et al.*, 2015; Massironi *et al.*, 2015). Furthermore, the global coverage produced by MESSENGER already provides sufficient data for determining slip trends all over Mercury. For this reason, the creation of a global database of faulted craters would be of great help for future investigations, once that more data are available. I believe that BepiColombo future targeting choices should be guided also by the issues discussed above. As an instance, HRIC captured frames will certainly better elucidate the pattern of fault intersections with key features, such as craters and vents. In addition, craters of smaller size could be measured in a more suitable way and extend the global database on Hermean kinematics.

Appendix A

A.1. ISIS3 processing techniques

The USGS Integrated Software for Imagers and Spectrometers (ISIS, Gaddis et al., 1997; Torson & Becker, 1997; Eliason et al., 1997) is a powerful tool for processing spacecraft images. In the following paragraphs, I make a list of the scripts used for gathering the processed data used in this thesis. In addition to ISIS3, also the Geospatial Data Abstraction Library (GDAL) was used to convert each processed ISIS image (*i.e.* cube file, *.cub) to a geotiff file readable by the GIS application (*e.g.* geotiff file, *.tif).

A.1.1. MDIS single frames and mosaics

The scripts below were written following the directions of the ISIS3 application documentation, the information contained in the MDIS Data User Workshop 2013 presentation (by Becker, K., Becker, T. and Hare, T.) and the suggestions coming from the ISIS3 support forum (see: <https://isis.astrogeology.usgs.gov/>).

```

mkdir -p LEV0 LEV1 LEV2 LEV3 RASTER MOSAIC

ls *.IMG | sed s:\.IMG::> basename.lis

mdis2isis -batchlist=basename.lis from=\$1.IMG
to=LEV0/\$1.lev0.cub

spiceinit -batchlist=basename.lis from=LEV0/\$1.lev0.cub

mdiscal -batchlist=basename.lis from=LEV0/\$1.lev0.cub
to=LEV1/\$1.lev1.cub

## A: Command for single frames ##

cam2map -batchlist=basename.lis from=LEV1/\$1.lev1.cub
to=LEV2/\$1.lev2.cub map=equivictoria.map

## B: Commmands for mosaicking ##

ls LEV1/*.lev1.cub > LEV1/baseLEV1.lis

mosrange fromlist=LEV1/baseLEV1.lis map=equivictoria.map
to=LEV2/template.map precision=0

cam2map -batchlist=basename.lis from=LEV1/\$1.lev1.cub
to=LEV2/\$1.lev2.cub map=LEV2/template.map pixres=map

```

Where `cam2map` application projects the MDIS cube files either using A) the file `equivictoria.map` for single frames, or B) the file `template.map` auto-generated by the `mosrange` application for mosaics.

The `equivictoria.map` projection file is defined below:

```

## MAP PROJECTION - equivictoria.map ##

Group = Mapping
  ProjectionName = Equirectangular

  TargetName      = Mercury
  EquatorialRadius = 2440000.0 <meters>
  PolarRadius     = 2440000.0 <meters>

  LatitudeType     = Planetocentric
  LongitudeDirection = PositiveEast
  LongitudeDomain   = 360 <degrees>

# Mercury H-02 Victoria
  CenterLatitude = 43.75 <degrees>
  CenterLongitude = 315.00 <degrees>

# OVERLAP = 0 <degrees>
# MinimumLatitude = -22.500000000000 <degrees>
# MaximumLatitude = 65.000000000000 <degrees>
# MinimumLongitude = 270.000000000000 <degrees>
# MaximumLongitude = 360.000000000000 <degrees>

# OVERLAP = 5 <degrees>
  MinimumLatitude = -17.500000000000 <degrees>
  MaximumLatitude = 70.000000000000 <degrees>
  MinimumLongitude = 265.000000000000 <degrees>
  MaximumLongitude = 365.000000000000 <degrees>

###MaximumLongitude is 365° to let the map2map application
  trim beyond 0°###

# BDR MAP SCALE
# PixelResolution = 166.35169433071 <meters/pixel>
  Scale = 256.000000000000 <pixels/degree>
End_Group

```

After the frames are projected, it is necessary to apply the photometry corrections suggested for each MDIS WAC/NAC filter by :

```
## MDIS PHOTOMETRIC CORRECTION ##

# Photometry correction with coefficient values for NAC "M"
  filter

ls LEV2/*M.lev2.cub && sed s:LEV2/:: | sed s:\.lev2.cub::>
  LEV3/baseM.lis

photomet -batchlist=baseM.lis from=LEV2/\$1.lev2.cub
  to=LEV3/\$1.lev3.cub phtname=hapkehen theta=17.76662946
  wh=0.278080114 hg1=0.227774899 hg2=0.714203968 hh=0.075
  b0=2.3 zerob0standard=false normname=albedo incref=30.0
  incmat=0.0 thresh=10e30 albedo=1.0

# Photometry correction with coefficient values for WAC "G"
  filter

ls LEV2/*G.lev2.cub && sed s:LEV2/:: | sed s:\.lev2.cub::>
  LEV3/baseG.lis

photomet -batchlist=baseG.lis from=LEV2/\$1.lev2.cub
  to=LEV3/\$1.lev3.cub phtname=hapkehen theta=17.76662946
  wh=0.278080114 hg1=0.227774899 hg2=0.714203968 hh=0.075
  b0=2.3 zerob0standard=false normname=albedo incref=30.0
  incmat=0.0 thresh=10e30 albedo=1.0

# Photometry correction with coefficient values for WAC "F"

ls LEV2/*F.lev2.cub && sed s:LEV2/:: | sed s:\.lev2.cub::>
  LEV3/baseF.lis

photomet -batchlist=baseF.lis from=LEV2/\$1.lev2.cub
  to=LEV3/\$1.lev3.cub phtname=hapkehen theta=12.07775431
  wh=0.153713769 hg1=0.221313433 hg2=0.887633784 hh=0.075
  b0=2.3 zerob0standard=false normname=albedo incref=30.0
  incmat=0.0 thresh=10e30 albedo=1.0

# Photometry correction with coefficient values for WAC "I"

ls LEV2/*I.lev2.cub && sed s:LEV2/:: | sed s:\.lev2.cub::>
  LEV3/baseI.lis

photomet -batchlist=baseI.lis from=LEV2/\$1.lev2.cub
  to=LEV3/\$1.lev3.cub phtname=hapkehen theta=18.41686847
  wh=0.35324478 hg1=0.276538744 hg2=0.613700193 hh=0.075
  b0=2.3 zerob0standard=false normname=albedo incref=30.0
  incmat=0.0 thresh=10e30 albedo=1.0
```



```

# Photometry correction with coefficient values for WAC "E"

ls LEV2/*E.lev2.cub && sed s:LEV2/:: | sed s:\.lev2.cub::>
    LEV3/baseE.lis

photomet -batchlist=baseE.lis from=LEV2/\$1.lev2.cub
        to=LEV3/\$1.lev3.cub phtname=hapkehen theta=15.78892162
        wh=0.215984749 hg1=0.206649235 hg2=0.811417942 hh=0.075
        b0=2.3 zerob0standard=false normname=albedo incref=30.0
        incmat=0.0 thresh=10e30 albedo=1.0

# Photometry correction with coefficient values for WAC "D"

ls LEV2/*D.lev2.cub && sed s:LEV2/:: | sed s:\.lev2.cub::>
    LEV3/baseD.lis

photomet -batchlist=baseD.lis from=LEV2/\$1.lev2.cub
        to=LEV3/\$1.lev3.cub phtname=hapkehen theta=15.78892162
        wh=0.215984749 hg1=0.206649235 hg2=0.811417942 hh=0.075 b0=2.3
        zerob0standard=false normname=albedo incref=30.0 incmat=0.0
        thresh=10e30 albedo=1.0

# Photometry correction with coefficient values for WAC "C"

ls LEV2/*C.lev2.cub && sed s:LEV2/:: | sed s:\.lev2.cub::>
    LEV3/baseC.lis

photomet -batchlist=baseC.lis from=LEV2/\$1.lev2.cub
        to=LEV3/\$1.lev3.cub phtname=hapkehen theta=13.82780392
        wh=0.182212955 hg1=0.212533357 hg2=0.856934992 hh=0.075 b0=2.3
        zerob0standard=false normname=albedo incref=30.0 incmat=0.0
        thresh=10e30 albedo=1.0

# Photometry correction with coefficient values for WAC "J"

ls LEV2/*J.lev2.cub && sed s:LEV2/:: | sed s:\.lev2.cub::>
    LEV3/baseJ.lis

photomet -batchlist=baseJ.lis from=LEV2/\$1.lev2.cub
        to=LEV3/\$1.lev3.cub phtname=hapkehen theta=18.07191127
        wh=0.32654443 hg1=0.261680383 hg2=0.650146228 hh=0.075 b0=2.3
        zerob0standard=false normname=albedo incref=30.0 incmat=0.0
        thresh=10e30 albedo=1.0

# Photometry correction with coefficient values for WAC "L"

ls LEV2/*L.lev2.cub && sed s:LEV2/:: | sed s:\.lev2.cub::>
    LEV3/baseL.lis

photomet -batchlist=baseL.lis from=LEV2/\$1.lev2.cub
        to=LEV3/\$1.lev3.cub phtname=hapkehen theta=17.96224797
        wh=0.304047732 hg1=0.245886415 hg2=0.678657724 hh=0.075 b0=2.3
        zerob0standard=false normname=albedo incref=30.0 incmat=0.0
        thresh=10e30 albedo=1.0

```

Finally, the frame/mosaic is stretched to 8bit and saved as a geotiff file:

```
## SINGLE FRAMES (A) AND MOSAICS (B) OUTPUT ##

## A: Commands for single frames ##

# 8bit stretch with clip at 0.5

stretch -batchlist=basename.lis from=LEV3/\$1.lev3.cub
to=LEV3/\$1.lev3.8bit.cub+8bit+1:254 USEPERCENTAGES=true
pairs="0:1 0.5:1 99.5:254 100:254" null=0 lis=1 lrs=0 his=255
hrs=255

# GeoTiff raster

gdal_translate -batchlist=basename.lis LEV3/\$1.lev3.8bit.cub
RASTER/\$1.lev3.8bit.tif

## B: Commands for mosaics ##

ls LEV3/*.lev3.cub > LEV3/baseLEV3.lis

automos fromlist=LEV3/baseLEV3.lis
mosaic=MOSAIC/mosaic.lev4.cub

# 8bit stretch with clip at 0.5

stretch from=MOSAIC/mosaic.lev4.cub
to=MOSAIC/mosaic.lev4.8bit.cub+8bit+1:254 USEPERCENTAGES=true
pairs="0:1 0.5:1 99.5:254 100:254" null=0 lis=1 lrs=0 his=255
hrs=255

# GeoTiff raster

gdal_translate MOSAIC/mosaic.lev4.8bit.cub
MOSAIC/mosaic.lev4.8bit.tif
```

The stretch command is useful to reduce the output file size, since it reduces a 32bit image into an 8bit image.

A.1.2. MDIS BDR mosaics

The tiles used for mosaicking H2-Bm-0 basemap with 5° overlap are 13 in total (see Fig. 2.1). Each tile is composed by the image file (*i.e.* *.img) and the label file containing image information (*i.e.* *.lbl) and sharing the file name with the associated image. Thus the list concerning H2 and 5° overlap is:

```
## BDR FILE LIST - baseBDR.lis ##
ls *BDR*.LBL | sed s:\.LBL::> baseBDR.lis
MDIS_BDR_256PPD_H01NP0
MDIS_BDR_256PPD_H02NE0
MDIS_BDR_256PPD_H02NW0
MDIS_BDR_256PPD_H02SE0
MDIS_BDR_256PPD_H02SW0
MDIS_BDR_256PPD_H03NE0
MDIS_BDR_256PPD_H03SE0
MDIS_BDR_256PPD_H05NW0
MDIS_BDR_256PPD_H05SW0
MDIS_BDR_256PPD_H06NE0
MDIS_BDR_256PPD_H06NW0
MDIS_BDR_256PPD_H07NE0
MDIS_BDR_256PPD_H10NW0
```

Each tile is already projected in equirectangular projection centred on its own centre. Thus, it was necessary to re-project the used tiles with a common projection, centred on H2 quadrangle centre using the application `map2map` that accesses to the file `equivictoria.map` described in A.1.1. After all the files are re-projected, the `automos` application is used to create the BDR mosaic:

```
## BDR MOSAICKING ##
mkdir -p CUB MAP H02

pds2isis -batchlist=baseBDR.lis from=\$1.LBL to=CUB/\$1.cub

map2map -batchlist=baseBDR.lis from=CUB/\$1.cub+1
        to=MAP/\$1.map.cub map=equivictoria.map matchmap=yes
        trim=yes

ls MAP/*.map.cub > MAP/projected.lis

automos fromlist=MAP/projected.lis
        mosaic=H02/H02_MDIS_BDR_256PPD_overlap_equ.cub
        matchbandbin=no priority=beneath

stretch from=H02/H02_MDIS_BDR_256PPD_overlap_equ.cub
        to=H02/H02_MDIS_BDR_256PPD_overlap_equ.8bit.cub+8bit+1:2
        54 USEPERCENTAGES=true pairs="0:1 0.5:1 99.5:254
        100:254" null=0 lis=1 lrs=0 his=255 hrs=255

gdal_translate H02/H02_MDIS_BDR_256PPD_overlap_equ.8bit.cub
        H02/H02_MDIS_BDR_256PPD_overlap_equ.8bit.tif
```

References

- ACOCELLA, V. & FUNICIELLO, R. (2006). Transverse systems along the extensional Tyrrhenian margin of central Italy and their influence on volcanism. *Tectonics*, **25** (2), DOI: [10.1029/2005TC001845](https://doi.org/10.1029/2005TC001845).
- AHARONSON, O., ZUBER, M. T. & SOLOMON, S. C. (2004). Crustal remanence in an internally magnetized non-uniform shell: a possible source for Mercury's magnetic field?. *Earth and Planetary Science Letters*, **218** (3), 261–268, DOI: [10.1016/S0012-821X\(03\)00682-4](https://doi.org/10.1016/S0012-821X(03)00682-4).
- AKI, K. & RICHARDS, P. G. (2002). Quantitative Seismology. 2nd edn. University Science Books, Sausalito, CA. ISBN: 0935702962.
- ALLMENDINGER, R. W., CARDOZO, N. & FISHER, D. M. (2011). Structural Geology Algorithms: Vectors and Tensors. Cambridge University Press. ISBN: 9781107401389.
- ARTHUR, D. W. G., AGNIERAY, A. P., HORVATH, R. A., WOOD, C. A. & CHAPMAN, C. R. (1963). The system of lunar craters, quadrant I. *Communications of the Lunar and Planetary Laboratory*, **2**, 71–78, bibcode: [1964CoLPL...2...71A](https://ui.adsabs.org/1964CoLPL...2...71A).
- BECKER, K. J., ROBINSON, M. S., BECKER, T. L., WELLER, L. A., TURNER, S., NGUYEN, L., SELBY, C., DENEVI, B. W., MURCHIE, S. L., MCNUTT, R. L. & SOLOMON, S. C. (2009). Near global mosaic of Mercury. In: *AGU Fall Meeting Abstracts*, **1**, 1189, bibcode: [2009AGUFM.P21A1189B](https://ui.adsabs.org/2009AGUFM.P21A1189B).
- BENKHOFF, J., VAN CASTEREN, J., HAYAKAWA, H., FUJIMOTO, M., LAAKSO, H., NOVARA, M., FERRI, P., MIDDLETON, H. R. & ZIETHE, R. (2010). BepiColombo—Comprehensive exploration of Mercury: Mission overview and science goals. *Planetary and Space Science*, **58** (1), 2–20, DOI: [10.1016/j.pss.2009.09.020](https://doi.org/10.1016/j.pss.2009.09.020).
- BLEWETT, D. T., CHABOT, N. L., DENEVI, B. W., ERNST, C. M., HEAD, J. W., IZENBERG, N. R., MURCHIE, S. L., SOLOMON, S. C., NITTLER, L. R., MCCOY, T. J., XIAO, Z., BAKER, D. M. H., FASSETT, C. I., BRADEN, S. E., OBERST, J., SCHOLTEN, F., PREUSKER, F. & HURWITZ, D. M. (2011). Hollows on Mercury: MESSENGER evidence for geologically recent volatile-related activity. *Science*, **333** (6051), 1856–1859, DOI: [10.1126/science.1211681](https://doi.org/10.1126/science.1211681).
- BOTTKE, W. F., JEDICKE, R., MORBIDELLI, A., PETIT, J. M. & GLADMAN, B. (2000). Understanding the distribution of near-Earth asteroids. *Science*, **288** (5474), 2190–2194, DOI: [10.1126/science.288.5474.2190](https://doi.org/10.1126/science.288.5474.2190).
- BOULEY, S., CRADDOCK, R. A., MANGOLD, N. & ANSAN, V. (2010). Characterization of fluvial activity in Parana Valles using different age-dating techniques. *Icarus*, **207** (2), 686–698, DOI: [10.1016/j.icarus.2009.12.030](https://doi.org/10.1016/j.icarus.2009.12.030).
- BURKE, K., SENGOR, C. & FRANCIS, P. (1984). Maxwell Montes in-Collisional Plateau on Venus?. In: *Lunar and Planetary Science Conference*, **15th**, 104–105, bibcode: [1984LPI...15..104B](https://ui.adsabs.org/1984LPI...15..104B).
- BYRNE, P. K., KLIMCZAK, C., ŞENGÖR, A. C., SOLOMON, S. C., WATTERS, T. R. & HAUCK, S. A. (2014). Mercury's global contraction much greater than earlier estimates. *Nature Geoscience*, **7** (4), 301–307, DOI: [10.1038/ngeo2097](https://doi.org/10.1038/ngeo2097).
- CINTALA, M. J., HEAD, J. W. & MUTCH, T. A. (1976). Characteristics of fresh martian craters as a function of diameter: Comparison with the Moon and Mercury. *Geophysical Research Letters*, **3** (3), 117–120, DOI: [10.1029/GL003i003p00117](https://doi.org/10.1029/GL003i003p00117).

- COWIE, P. A. & SCHOLZ, C. H. (1992). Displacement-length scaling relationship for faults: data synthesis and discussion. *Journal of Structural Geology*, **14** (10), 1149–1156, DOI: [10.1016/0191-8141\(92\)90066-6](https://doi.org/10.1016/0191-8141(92)90066-6).
- CRATER ANALYSIS TECHNIQUES WORKING GROUP (1979). Standard techniques for presentation and analysis of crater size-frequency data. *Icarus*, **37** (2), 467–474, DOI: [10.1016/0019-1035\(79\)90009-5](https://doi.org/10.1016/0019-1035(79)90009-5).
- DANIELSON, G. E., Klaasen, K. P. & Anderson, J. L. (1975). Acquisition and description of Mariner 10 television science data at Mercury. *Journal of Geophysical Research*, **80** (17), 2357–2393, DOI: [10.1029/JB080i017p02357](https://doi.org/10.1029/JB080i017p02357).
- DAVIES, M. E., Dornik, S. E., Gault, D. E. & Strom, R. G. (1978). Atlas of Mercury. *NASA Special Publication*, **423**, bibcode: [1978NASSP.423.....D](https://ui.adsabs.org/1978NASSP.423.....D).
- DEETZ, C. H. & ADAMS, O. S. (1934). Elements of map projection with applications to map and chart construction. 4th ed. *Special publication* (U.S. Coast and Geodetic Survey), **68**. US Government Printing Office.
- DE HON, R. A., Scott, D. H. & Underwood, J. R., Jr. (1981). Geologic map of the Kuiper Quadrangle of Mercury. *US Geological Survey*, Map **I-1233**.
- DENEVI, B. W., Ernst, C. M., Meyer, H. M., Robinson, M. S., Murchie, S. L., Whitten, J. L., Head, J. W., Watters, T. R., Solomon, S. C., Ostrach, L. R., Chapman, C. R., Byrne, P. K., Klimczak, C. & Peplowski, P. N. (2013). The distribution and origin of smooth plains on Mercury. *Journal of Geophysical Research: Planets*, **118** (5), 891–907, DOI: [10.1002/jgre.20075](https://doi.org/10.1002/jgre.20075).
- DI ACHILLE, G., Popa, C., Massironi, M., Mazzotta Epifani, E., Zusi, M., Cremonese, G. & Palumbo, P. (2012). Mercury's radius change estimates revisited using MESSENGER data. *Icarus*, **221** (1), 456–460, DOI: [10.1016/j.icarus.2012.07.005](https://doi.org/10.1016/j.icarus.2012.07.005).
- DOMBARD, A. J. & HAUCK II, S. A. (2008). Despinning plus global contraction and the orientation of lobate scarps on Mercury: Predictions for MESSENGER. *Icarus*, **198** (1), 274–276, DOI: [10.1016/j.icarus.2008.06.008](https://doi.org/10.1016/j.icarus.2008.06.008).
- DZURISIN, D. (1978). The tectonic and volcanic history of Mercury as inferred from studies of scarps, ridges, troughs, and other lineaments. *Journal of Geophysical Research: Solid Earth* (1978–2012), **83** (B10), 4883–4906, DOI: [10.1029/JB083iB10p04883](https://doi.org/10.1029/JB083iB10p04883).
- ELIASON, E. M. (1997). Production of digital image models using the ISIS system. In: *Lunar and Planetary Science Conference*, **28th**, 331, bibcode: [1997LPL....28..331E](https://ui.adsabs.org/1997LPL....28..331E).
- FASSETT, C. I. & HEAD III, J. W. (2008). Valley network-fed, open-basin lakes on Mars: Distribution and implications for Noachian surface and subsurface hydrology. *Icarus*, **198** (1), 37–56, DOI: [10.1016/j.icarus.2008.06.016](https://doi.org/10.1016/j.icarus.2008.06.016).
- FASSETT, C. I., Kadish, S. J., Head, J. W., Solomon, S. C. & Strom, R. G. (2011). The global population of large craters on Mercury and comparison with the Moon. *Geophysical Research Letters*, **38** (10), DOI: [10.1029/2011GL047294](https://doi.org/10.1029/2011GL047294).
- FASSETT, C. I., Head, J. W., Blewett, D. T., Chapman, C. R., Dickson, J. L., Murchie, S. L., Solomon, S. C. & Watters, T. R. (2009). Caloris impact basin: exterior geomorphology, stratigraphy, morphometry, radial sculpture, and smooth plains deposits. *Earth and Planetary Science Letters*, **285** (3), 297–308, DOI: [10.1016/j.epsl.2009.05.022](https://doi.org/10.1016/j.epsl.2009.05.022).
- GADDIS, L., Anderson, J., Becker, K., Becker, T., Cook, D., Edwards, K., ... & Robinson, M. (1997). An overview of the integrated software for imaging spectrometers (ISIS). In: *Lunar and Planetary Science Conference*, **28th**, 387, bibcode: [1997LPL....28..387G](https://ui.adsabs.org/1997LPL....28..387G).

- GALLUZZI, V., Di Achille, G., Ferranti, L., Popa, C. & Palumbo, P. (2015). Faulted craters as indicators for thrust motions on Mercury. *Geological Society, London, Special Publications*, **401**, 313–325, DOI: [10.1144/SP401.17](https://doi.org/10.1144/SP401.17).
- GAULT, D. E. & WEDEKIND, J. A. (1978). Experimental studies of oblique impact. In: *Lunar and Planetary Science Conference*, **9th**, 3843–3875, bibcode: [1978LPSC....9.3843G](https://ui.adsabs.org/1978LPSC....9.3843G).
- GIACOMINI, L., Massironi, M., Marchi, S., Fassett, C. I., Di Achille, G. & Cremonese, G. (2015). Age dating of an extensive thrust system on Mercury: implications for the planet's thermal evolution. *Geological Society, London, Special Publications*, **401**, 291–311, DOI: [10.1144/SP401.21](https://doi.org/10.1144/SP401.21).
- GILBERT, G. K. (1893). The Moon's face: A study of the origin of its features. Philosophical Society of Washington.
- GOLOMBEK, M. P., Tanaka, K. L. & Franklin, B. J. (1996). Extension across Tempe Terra, Mars, from measurements of fault scarp widths and deformed craters. *Journal of Geophysical Research: Planets* (1991–2012), **101** (E11), 26119–26130, DOI: [10.1029/96JE02709](https://doi.org/10.1029/96JE02709).
- GOUDGE, T. A., Head, J. W., Kerber, L., Blewett, D. T., Denevi, B. W., Domingue, D. L., Gillis-Davis, J. J., Gwinner, K., Helbert, J., Holsclaw, G. M., Izenberg, N. R., Klima, R. L., McClintock, W. E., Murchie, S. L., Neumann, G. A., Smith, D. E., Strom, R. J., Xiao, Z., Zuber, M. T. & Solomon, S. C. (2014). Global inventory and characterization of pyroclastic deposits on Mercury: New insights into pyroclastic activity from MESSENGER orbital data. *Journal of Geophysical Research: Planets*, **119** (3), 635–658, DOI: [10.1002/2013JE004480](https://doi.org/10.1002/2013JE004480).
- GROLIER, M. J. & BOYCE, J. (1984). Geologic map of the Borealis region of Mercury. *US Geological Survey*, Map **I-1660**.
- GUEST, J. E. & GREELEY, R. (1983). Geologic map of the Shakespeare quadrangle of Mercury. *US Geological Survey*, Map **I-1408**.
- GUEST, J. E. & O'DONNELL, W. P. (1977). Surface history of Mercury: A review. *Vistas in Astronomy*, **20** (2), 273–300, DOI: [10.1016/0083-6656\(77\)90006-X](https://doi.org/10.1016/0083-6656(77)90006-X).
- HAUCK II, S. A., Dombard, A. J., Phillips, R. J. & Solomon, S. C. (2004). Internal and tectonic evolution of Mercury. *Earth and Planetary Science Letters*, **222** (3), 713–728, DOI: [10.1016/j.epsl.2004.03.037](https://doi.org/10.1016/j.epsl.2004.03.037).
- HAWKINS III, S. E., Boldt, J. D., Darlington, E. H., Espiritu, R., Gold, R. E., Gotwols, B., Grey, M. P., Hash, C. D., Hayes, J. R., Jaskulek, S. E., Kardian Jr., C. J., Keller, M. R., Malaret, E. R., Murchie, S. L., Murphy, P. K., Peacock, K., Prockter, L. M., Reiter, R. A., Robinson, M. S., Schaefer, E. D., Shelton, R. G., Sterner II, R. E., Taylor, H. W., Watters, T. R. & Williams, B. D. (2007). The Mercury dual imaging system on the MESSENGER spacecraft. *Space Science Reviews*, **131** (1–4), 247–338, DOI: [10.1007/s11214-007-9266-3](https://doi.org/10.1007/s11214-007-9266-3).
- HEAD, J. W., Chapman, C. R., Strom, R. G., Fassett, C. I., Denevi, B. W., Blewett, D. T., Ernst, C.M., Watters, T. R., Solomon, S. C., Murchie, S. L., Prockter, L. M., Chabot, N. L., Gillis-Davis, J. J., Whitten, J. L., Goudge, T. A., Baker, D.M., Hurwitz, D. M., Ostrach, L. R., Xiao, Z., Merline, W. J., Kerber, L., Dickson, J. L., Oberst, J., Byrne, P. K., Klimczak, C. & Nittler, L. R. (2011). Flood volcanism in the northern high latitudes of Mercury revealed by MESSENGER. *Science*, **333** (6051), 1853–1856, DOI: [10.1126/science.1211997](https://doi.org/10.1126/science.1211997).
- HIESINGER, H., Jaumann, R., Neukum, G. & Head, J. W. (2000). Ages of mare basalts on the lunar nearside. *Journal of Geophysical Research: Planets* (1991–2012), **105** (E12), 29239–29275, DOI: [10.1029/2000JE001244](https://doi.org/10.1029/2000JE001244).

- HOKE, M. R. & HYNEK, B. M. (2009). Roaming zones of precipitation on ancient Mars as recorded in valley networks. *Journal of Geophysical Research: Planets* (1991–2012), **114** (E8), DOI: [10.1029/2008JE003247](https://doi.org/10.1029/2008JE003247).
- HUBBERT, M. K. & RUBEY, W. W. (1959). Role of fluid pressure in mechanics of overthrust faulting I. Mechanics of fluid-filled porous solids and its application to overthrust faulting. *Geological Society of America Bulletin*, **70** (2), 115–166, DOI: [10.1130/0016-7606\(1959\)70\[115:ROFPIM\]2.0.CO;2](https://doi.org/10.1130/0016-7606(1959)70[115:ROFPIM]2.0.CO;2).
- IVANOV, B. A., Neukum, G. & Wagner, R. (2001). Size-frequency distributions of planetary impact craters and asteroids. In: *Collisional Processes in the Solar System*, **261**, 1–34, DOI: [10.1007/978-94-010-0712-2_1](https://doi.org/10.1007/978-94-010-0712-2_1).
- JENNESS, J. 2011. Tools for Graphics and Shapes: Extension for ArcGIS. Jenness Enterprises. Available at: http://www.jennessent.com/arcgis/shapes_graphics.htm
- KENKMANN, T., Poelchau, M. H. & Wulf, G. (2014). Structural geology of impact craters. *Journal of Structural Geology*, **62**, 156–182, DOI: [10.1016/j.jsg.2014.01.015](https://doi.org/10.1016/j.jsg.2014.01.015).
- KERBER, L., Head, J. W., Solomon, S. C., Murchie, S. L., Blewett, D. T. & Wilson, L. (2009). Explosive volcanic eruptions on Mercury: Eruption conditions, magma volatile content, and implications for interior volatile abundances. *Earth and Planetary Science Letters*, **285** (3), 263–271, DOI: [10.1016/j.epsl.2009.04.037](https://doi.org/10.1016/j.epsl.2009.04.037).
- KERBER, L., Head, J. W., Blewett, D. T., Solomon, S. C., Wilson, L., Murchie, S. L., Robinson, M. S., Denevi, B. W. & Domingue, D. L. (2011). The global distribution of pyroclastic deposits on Mercury: The view from MESSENGER flybys 1–3. *Planetary and Space Science*, **59** (15), 1895–1909, DOI: [10.1016/j.pss.2011.03.020](https://doi.org/10.1016/j.pss.2011.03.020).
- KIEFER, W. S. & MURRAY, B. C. (1987). The formation of Mercury's smooth plains. *Icarus*, **72** (3), 477–491, DOI: [10.1016/0019-1035\(87\)90046-7](https://doi.org/10.1016/0019-1035(87)90046-7).
- KIM, Y. S. & SANDERSON, D. J. (2005). The relationship between displacement and length of faults: a review. *Earth Science Reviews*, **68** (3), 317–334, DOI: [10.1016/j.earscirev.2004.06.003](https://doi.org/10.1016/j.earscirev.2004.06.003).
- KING, J. S. & SCOTT, D. H. (1990). Geologic map of the Beethoven quadrangle of Mercury. *US Geological Survey*, Map **I-2048**.
- KING, S. D. (2008). Pattern of lobate scarps on Mercury's surface reproduced by a model of mantle convection. *Nature Geoscience*, **1** (4), 229–232, DOI: [10.1038/ngeo152](https://doi.org/10.1038/ngeo152).
- KLIMCZAK, C., Byrne, P. K., & Solomon, S. C. (2015). A rock-mechanical assessment of Mercury's global tectonic fabric. *Earth and Planetary Science Letters*, **416**, 82–90, DOI: [10.1016/j.epsl.2015.02.003](https://doi.org/10.1016/j.epsl.2015.02.003).
- KNEISSL, T., Van Gasselt, S. & Neukum, G. (2011). Map-projection-independent crater size-frequency determination in GIS environments—New software tool for ArcGIS. *Planetary and Space Science*, **59** (11), 1243–1254, DOI: [10.1016/j.pss.2010.03.015](https://doi.org/10.1016/j.pss.2010.03.015).
- KNEISSL, T., Michael, G. G., Platz, T. & Walter, S. H. G. (2015). Age determination of linear surface features using the Buffered Crater Counting approach – Case studies of the Sirenum and Fortuna Fossae graben systems on Mars. *Icarus*, **250**, 284–394, DOI: [10.1016/j.icarus.2014.12.008](https://doi.org/10.1016/j.icarus.2014.12.008).
- LEAKE, M. A. (1982). The intercrater plains of Mercury and the Moon: their nature, origin, and role in terrestrial planet evolution. *Advances in Planetary Geology*, **1**, 3–535, bibcode: [1982apg.book....3L](https://ui.adsabs.org/1982apg.book....3L).
- MANCINELLI, P., Minelli, F., Mondini, A., Pauselli, C. & Federico, C. (2015). A downscaling approach for geological characterization of the Raditladi basin of Mercury. *Geological Society, London, Special Publications*, **401**, 57–75, DOI: [10.1144/SP401.10](https://doi.org/10.1144/SP401.10).

- MARCHI, S., Mottola, S., Cremonese, G., Massironi, M. & Martellato, E. (2009). A new chronology for the Moon and Mercury. *The Astronomical Journal*, **137** (6), 4936–4948, DOI: [10.1088/0004-6256/137/6/4936](https://doi.org/10.1088/0004-6256/137/6/4936).
- MARCHI, S., Massironi, M., Cremonese, G., Martellato, E., Giacomini, L. & Prockter, L. (2011). The effects of the target material properties and layering on the crater chronology: The case of Raditladi and Rachmaninoff basins on Mercury. *Planetary and Space Science*, **59** (15), 1968–1980, DOI: [10.1016/j.pss.2011.06.007](https://doi.org/10.1016/j.pss.2011.06.007).
- MARGOT, J. L., Peale, S. J., Jurgens, R. F., Slade, M. A. & Holin, I. V. (2007). Large longitude libration of Mercury reveals a molten core. *Science*, **316** (5825), 710–714, DOI: [10.1126/science.1140514](https://doi.org/10.1126/science.1140514).
- MASSIRONI, M., Di Achille, G., Rothery, D. A., Galluzzi, V., Giacomini, L., Ferrari, S., Zusi, M., Cremonese, G. & Palumbo, P. (2015). Lateral ramps and strike-slip kinematics on Mercury. *Geological Society, London, Special Publications*, **401**, 269–290, DOI: [10.1144/SP401.16](https://doi.org/10.1144/SP401.16).
- MATSUYAMA, I. & NIMMO, F. (2009). Gravity and tectonic patterns of Mercury: Effect of tidal deformation, spin-orbit resonance, nonzero eccentricity, despinning, and reorientation. *Journal of Geophysical Research: Planets* (1991–2012), **114** (E1), DOI: [10.1029/2008JE003252](https://doi.org/10.1029/2008JE003252).
- MCCAULEY, J. F. & WILHELMS, D. E. (1971). Geological provinces of the near side of the Moon. *Icarus*, **15** (3), 363–367, DOI: [10.1016/0019-1035\(71\)90114-X](https://doi.org/10.1016/0019-1035(71)90114-X).
- MCCAULEY, J. F., Guest, J. E., Schaber, G. G., Trask, N. J. & Greeley, R. (1981). Stratigraphy of the Caloris basin, Mercury. *Icarus*, **47** (2), 184–202, DOI: [10.1016/0019-1035\(81\)90166-4](https://doi.org/10.1016/0019-1035(81)90166-4).
- MCCLAY, K. R. (1992). Thrust tectonics. Chapman & Hall, London, ISBN: 978-0-412-43900-1.
- MCGILL, G. E. & KING, E. A. (1983). Geologic map of the Victoria Quadrangle of Mercury. *US Geological Survey, Map* **1-1409**.
- MELOSH, H. J. (1977). Global tectonics of a despun planet. *Icarus*, **31** (2), 221–243, DOI: [10.1016/0019-1035\(77\)90035-5](https://doi.org/10.1016/0019-1035(77)90035-5).
- MELOSH, H. J. (1989). Impact cratering: A geologic process. In: *Oxford Monographs on Geology and Geophysics*, 11. Oxford University Press, New York.
- MELOSH, H. J. & DZURISIN, D. (1978). Mercurian global tectonics: A consequence of tidal despinning?. *Icarus*, **35** (2), 227–236, DOI: [10.1016/0019-1035\(78\)90007-6](https://doi.org/10.1016/0019-1035(78)90007-6).
- MELOSH, H. J. & MCKINNON, W. B. (1988). The tectonics of Mercury. In: Vilas, F., Chapman, C. R. & Matthews, M. S. (eds), *Mercury*, 374–400, University of Arizona Press, ISBN: 0816510857.
- MICHAEL, G. G. & NEUKUM, G. (2010). Planetary surface dating from crater size–frequency distribution measurements: Partial resurfacing events and statistical age uncertainty. *Earth and Planetary Science Letters*, **294** (3), 223–229, DOI: [10.1016/j.epsl.2009.12.041](https://doi.org/10.1016/j.epsl.2009.12.041).
- MICHEL, N. C., Hauck, S. A., Solomon, S. C., Phillips, R. J., Roberts, J. H. & Zuber, M. T. (2013). Thermal evolution of Mercury as constrained by MESSENGER observations. *Journal of Geophysical Research: Planets*, **118** (5), 1033–1044, DOI: [10.1002/jgre.20049](https://doi.org/10.1002/jgre.20049).
- MURCHIE, S. L., Watters, T. R., Robinson, M. S., Head, J. W., Strom, R. G., Chapman, C. R., Solomon, S. C., McClintock, W. E., Prockter, L. M., Domingue, D. L. & Blewett, D. T. (2008). Geology of the Caloris basin, Mercury: A view from MESSENGER. *Science*, **321** (5885), 73–76, DOI: [10.1126/science.1159261](https://doi.org/10.1126/science.1159261).

- MURRAY, B. C., Belton, M. J., Danielson, G. E., Davies, M. E., Gault, D. E., Hapke, B., O'Leary, B., Strom, R. G., Suomi, V. & Trask, N. (1974). Mercury's surface: Preliminary description and interpretation from Mariner 10 pictures. *Science*, **185** (4146), 169–179, DOI: [10.1126/science.185.4146.169](https://doi.org/10.1126/science.185.4146.169).
- MURRAY, B. C., Strom, R. G., Trask, N. J. & Gault, D. E. (1975). Surface history of Mercury: Implications for terrestrial planets. *Journal of Geophysical Research*, **80** (17), 2508–2514, DOI: [10.1029/JB080i017p02508](https://doi.org/10.1029/JB080i017p02508).
- NESS, N. F., Behannon, K. W., Lepping, R. P., Whang, Y. C. & Schatten, K. H. (1974). Magnetic field observations near Mercury: Preliminary results from Mariner 10. *Science*, **185** (4146), 151–160, DOI: [10.1126/science.185.4146.151](https://doi.org/10.1126/science.185.4146.151).
- NEUKUM, G. & IVANOV, B. A. (1994). Crater size distributions and impact probabilities on Earth from lunar, terrestrial-planet, and asteroid cratering data. In: Gehrels, T. (ed), *Hazards due to Comets and Asteroids*, University of Arizona Press, ISBN: 9780816515059.
- NEUKUM, G., Oberst, J., Hoffmann, H., Wagner, R. & Ivanov, B. A. (2001a). Geologic evolution and cratering history of Mercury. *Planetary and Space Science*, **49** (14), 1507–1521, DOI: [10.1016/S0032-0633\(01\)00089-7](https://doi.org/10.1016/S0032-0633(01)00089-7).
- NEUKUM, G., Ivanov, B. A. & Hartmann, W. K. (2001b). Cratering records in the inner solar system in relation to the lunar reference system. *Space Science Reviews*, **96** (1–4), 55–86, DOI: [10.1023/A:1011989004263](https://doi.org/10.1023/A:1011989004263).
- NITTLER, L. R., Starr, R. D., Weider, S. Z., McCoy, T. J., Boynton, W. V., Ebel, D. S., Ernst, C. M., Evans, L. G., Goldsten, J. O., Hamara, D. K., Lawrence, D. J., McNutt, R. L., Schlemm, C. E., Solomon, S. C., Sprague, A. L. & Sprague, A. L. (2011). The major-element composition of Mercury's surface from MESSENGER X-ray spectrometry. *Science*, **333** (6051), 1847–1850, DOI: [10.1126/science.1211567](https://doi.org/10.1126/science.1211567).
- OBERBECK, V. R., Quaide, W. L., Arvidson, R. E. & Aggarwal, H. R. (1977). Comparative studies of lunar, martian, and mercurian craters and plains. *Journal of Geophysical Research*, **82** (11), 1681–1698, DOI: [10.1029/JB082i011p01681](https://doi.org/10.1029/JB082i011p01681).
- OSTRACH, L. R., Robinson, M. S., Denevi, B. W. & Thomas, P. C. (2011). Effects of incidence angle on crater counting observations. In: *Lunar and Planetary Institute Science Conference*, **42**, 1202, bibcode: [2011LPI...42.1202O](https://ui.adsabs.org/2011LPI...42.1202O).
- PAPPALARDO, R. T. & COLLINS, G. C. (2005). Strained craters on Ganymede. *Journal of structural geology*, **27** (5), 827–838, DOI: [10.1016/j.jsg.2004.11.010](https://doi.org/10.1016/j.jsg.2004.11.010).
- PECHMANN, J. B. & MELOSH, H. J. (1979). Global fracture patterns of a despun planet: Application to Mercury. *Icarus*, **38** (2), 243–250, DOI: [10.1016/0019-1035\(79\)90181-7](https://doi.org/10.1016/0019-1035(79)90181-7).
- PLESCIA, J. B. & GOLOMBEK, M. P. (1986). Origin of planetary wrinkle ridges based on the study of terrestrial analogs. *Geological Society of America Bulletin*, **97** (11), 1289–1299, DOI: [10.1130/0016-7606\(1986\)97<1289:OOPWRB>2.0.CO;2](https://doi.org/10.1130/0016-7606(1986)97<1289:OOPWRB>2.0.CO;2).
- POHN, H. A. & OFFIELD, T. W. (1970). Lunar crater morphology and relative-age determination of lunar geologic units—Part 1. Classification. *US Geological Survey Prof. Paper*, 153–162.
- PREUSKER, F., Oberst, J., Head, J. W., Watters, T. R., Robinson, M. S., Zuber, M. T. & Solomon, S. C. (2011). Stereo topographic models of Mercury after three MESSENGER flybys. *Planetary and Space Science*, **59** (15), 1910–1917, DOI: [10.1016/j.pss.2011.07.005](https://doi.org/10.1016/j.pss.2011.07.005).
- POBLET, J. & LISLE, R. J. (2011). Kinematic evolution and structural styles of fold-and-thrust belts. *Geological Society, London, Special Publications*, **349** (1), 1–24, DOI: [10.1144/SP349.1](https://doi.org/10.1144/SP349.1).

- ROBERTS, G. P. (1996). Variation in fault-slip directions along active and segmented normal fault systems. *Journal of Structural Geology*, **18** (6), 835–845 , DOI: [10.1016/S0191-8141\(96\)80016-2](https://doi.org/10.1016/S0191-8141(96)80016-2).
- ROTHERY, D. A. & MASSIRONI, M. (2013). A Spectrum of Tectonised Basin Edges on Mercury. In: *Lunar and Planetary Institute Science Conference*, **44**, 1175 , bibcode: [2013LPI...44.1175R](https://ui.adsabs.org/2013LPI...44.1175R).
- ROTHERY, D. A., Thomas, R. J. & Kerber, L. (2014). Prolonged eruptive history of a compound volcano on Mercury: Volcanic and tectonic implications. *Earth and Planetary Science Letters*, **385**, 59–67 , DOI: [10.1016/j.epsl.2013.10.023](https://doi.org/10.1016/j.epsl.2013.10.023).
- SCHABER, G. G. & MCCAULEY, J. F. (1980). Geologic Map of the Tolstoj Quadrangle of Mercury. *US Geological Survey*, Map **I-1199**.
- SCHULTZ, R. A. & WATTERS, T. R. (2001). Forward mechanical modeling of the Amenthes Rupes thrust fault on Mars. *Geophysical Research Letters*, **28** (24), 4659–4662 , DOI: [10.1029/2001GL013468](https://doi.org/10.1029/2001GL013468).
- SHOEMAKER, E. M. & HACKMAN, R. J. (1962). Stratigraphic basis for a lunar time scale. In: Kopal, Z. & Mikhailov, Z. K. (eds) *The Moon*, International Astronomical Union Symposium, **14**, 289–300 , bibcode: [1962IAUS...14.289S](https://ui.adsabs.org/1962IAUS...14.289S).
- SHOEMAKER, E. M. (1962). Interpretation of lunar craters. In: Kopal, Z. (ed), *Physics and Astronomy of the Moon*, 283–359, Academic Press, New York, ISBN: 9781483232409.
- SIEGFRIED II, R. W. & SOLOMON, S. C. (1974). Mercury: Internal structure and thermal evolution. *Icarus*, **23** (2), 192–205 , DOI: [10.1016/0019-1035\(74\)90005-0](https://doi.org/10.1016/0019-1035(74)90005-0).
- SMITH, D. E., Zuber, M. T., Phillips, R. J., Solomon, S. C., Hauck, S. A., Lemoine, F. G., Mazarico, E., Neumann, G. A., Peale, S. J., Margot, J. L., Johnson, C. L., Torrence, M. H., Perry, M. E., Rowlands, D. D., Goossens, S., Head, J. W. & Taylor, A. H. (2012). Gravity field and internal structure of Mercury from MESSENGER. *Science*, **336** (6078), 214–217 , DOI: [10.1126/science.1218809](https://doi.org/10.1126/science.1218809).
- SOLOMON, S. C. (1976). Some aspects of core formation in Mercury. *Icarus*, **28** (4), 509–521, DOI: [10.1016/0019-1035\(76\)90124-X](https://doi.org/10.1016/0019-1035(76)90124-X).
- SOLOMON, S. C., McNutt Jr., R. L., Gold, R. E. & Domingue, D. L. (2007). MESSENGER mission overview. *Space Science Reviews*, **131** (1–4), 3–39, DOI: [10.1007/s11214-007-9247-6](https://doi.org/10.1007/s11214-007-9247-6).
- SOLOMON, S. C., McNutt, R. L., Watters, T. R., Lawrence, D. J., Feldman, W. C., Head, J. W., Krimigis, S. M., Murchie, S. L., Phillips, R. J., Slavin, J. A. & Zuber, M. T. (2008). Return to Mercury: A global perspective on MESSENGER's first Mercury flyby. *Science*, **321** (5885), 59–62, DOI: [10.1126/science.1159706](https://doi.org/10.1126/science.1159706).
- SPUDIS, P. D. & GUEST, J. E. (1988). Stratigraphy and geologic history of Mercury. In: Vilas, F., Chapman, C. R. & Matthews, M. S. (eds), *Mercury*, 118–164, University of Arizona Press, ISBN: 0816510857.
- SPUDIS, P. D. & PROSSER, J. G. (1984). Geologic map of the Michelangelo quadrangle of Mercury. *US Geological Survey*, Map **I-1659**.
- SPUDIS, P. D. (1985). A Mercurian chronostratigraphic classification. In: *Reports of Planetary Geology and Geophysics Program*, NASA TM-87563, 595–597.
- STEPHENSON, A. (1976). Crustal remanence and the magnetic moment of Mercury. *Earth and Planetary Science Letters*, **28** (3), 454–458 , DOI: [10.1016/0012-821X\(76\)90206-5](https://doi.org/10.1016/0012-821X(76)90206-5).
- STROM, R. G. (1977). Origin and relative age of lunar and mercurian intercrater plains. *Physics of the Earth and Planetary Interiors*, **15** (2), 156–172 , DOI: [10.1016/0031-9201\(77\)90028-0](https://doi.org/10.1016/0031-9201(77)90028-0).

- STROM, R. G. & NEUKUM, G. (1988). The cratering record on Mercury and the origin of impacting objects. In: Vilas, F., Chapman, C. R. & Matthews, M. S. (eds), *Mercury*, 336–373, University of Arizona Press, ISBN: 0816510857.
- STROM, R. G., Trask, N. J. & Guest, J. E. (1975). Tectonism and volcanism on Mercury. *Journal of Geophysical Research*, **80** (17), 2478–2507, DOI: [10.1029/JB080i017p02478](https://doi.org/10.1029/JB080i017p02478).
- STROM, R. G., Malin, M. C. & Leake, M. A. (1990). Geologic map of the Bach quadrangle of Mercury. *US Geological Survey*, Map **I-2015**.
- STROM, R. G., Chapman, C. R., Merline, W. J., Solomon, S. C. & Head, J. W. (2008). Mercury cratering record viewed from MESSENGER's first flyby. *Science*, **321** (5885), 79–81, DOI: [10.1126/science.1159317](https://doi.org/10.1126/science.1159317).
- STROM, R. G., Banks, M. E., Chapman, C. R., Fassett, C. I., Forde, J. A., Head III, J. W., Merline, W. J., Prockter, L. M. & Solomon, S. C. (2011). Mercury crater statistics from MESSENGER flybys: Implications for stratigraphy and resurfacing history. *Planetary and Space Science*, **59** (15), 1960–1967, DOI: [10.1016/j.pss.2011.03.018](https://doi.org/10.1016/j.pss.2011.03.018).
- TANAKA, K. L. (1982). A new time-saving crater-count technique, with application to narrow features. In: *Reports of Planetary Geology Program*. NASA TM-85127.
- TANAKA, K. L., Skinner Jr., J. A. & Hare, T. M. (2011). Planetary geologic mappers handbook. *USGS Astrogeology Science Center*.
- THOMAS, P. G. & ALLEMAND, P. (1993). Quantitative analysis of the extensional tectonics of Tharsis bulge, Mars: Geodynamic implications. *Journal of Geophysical Research: Planets* (1991–2012), **98** (E7), 13097–13108, DOI: [10.1029/93JE01326](https://doi.org/10.1029/93JE01326).
- THOMAS, R. J., Rothery, D. A., Conway, S. J. & Anand, M. (2014a). Hollows on Mercury: Materials and mechanisms involved in their formation. *Icarus*, **229**, 221–235, DOI: [10.1016/j.icarus.2013.11.018](https://doi.org/10.1016/j.icarus.2013.11.018).
- THOMAS, R. J., Rothery, D. A., Conway, S. J. & Anand, M. (2014b). Mechanisms of explosive volcanism on Mercury: Implications from its global distribution and morphology. *Journal of Geophysical Research: Planets*, **119** (10), 2239–2254, DOI: [10.1002/2014JE004692](https://doi.org/10.1002/2014JE004692).
- THOMAS, R. J., Rothery, D. A., Conway, S. J. & Anand, M. (2014c). Long-lived explosive volcanism on Mercury. *Geophysical Research Letters*, **41** (17), 6084–6092, DOI: [10.1002/2014GL061224](https://doi.org/10.1002/2014GL061224).
- TOBLER, W. (1987). Measuring Spatial Resolution. *Proceedings of the Land Resources Information Systems Conference, Beijing*, 12–16.
- TORSON, J. M. & BECKER, K. J. (1997). ISIS-A software architecture for processing planetary images. In: *Lunar and Planetary Science Conference*, **28**, 1443, bibcode: [1997LPI....28.1443T](https://ui.adsabs.org/1997LPI....28.1443T).
- TRASK, N. J. & DZURISIN, D. (1984). Geologic map of the Discovery quadrangle of Mercury. *US Geological Survey*, Map **I-1658**.
- TRASK, N. J. & GUEST, J. E. (1975). Preliminary geologic terrain map of Mercury. *Journal of Geophysical Research*, **80** (17), 2461–2477, DOI: [10.1029/JB080i017p02461](https://doi.org/10.1029/JB080i017p02461).
- TRASK, N. J. & STROM, R. G. (1976). Additional evidence of Mercurian volcanism. *Icarus*, **28** (4), 559–563, DOI: [10.1016/0019-1035\(76\)90129-9](https://doi.org/10.1016/0019-1035(76)90129-9).
- TWISS, R. J. & MOORES, E. M. (2007). Structural Geology (2nd edition). W. H. Freeman, New York, ISBN: 9780716749516.

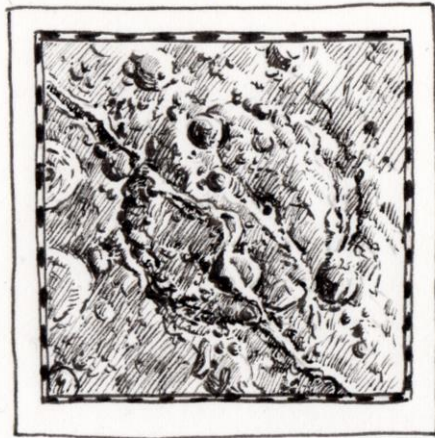
- VILAS, F., Chapman, C. R. & Matthews, M. S. (1988). Mercury. The University of Arizona Press, ISBN: 0816510857.
- WATTERS, T. R. (1993). Compressional tectonism on Mars. *Journal of Geophysical Research: Planets (1991–2012)*, **98** (E9), 17049–17060, DOI: [10.1029/93JE01138](https://doi.org/10.1029/93JE01138).
- WATTERS, T. R. (2003). Thrust faults along the dichotomy boundary in the eastern hemisphere of Mars. *Journal of Geophysical Research: Planets (1991–2012)*, **108** (E6), DOI: [10.1029/2002JE001934](https://doi.org/10.1029/2002JE001934).
- WATTERS, T. R. & NIMMO, F. (2010). The tectonics of Mercury. In: Watters, T. R. & Schultz, R. A. (eds), *Planetary tectonics*, Cambridge University Press, ISBN: 9780521749923.
- WATTERS, T. R., Robinson, M. S. & Cook, A. C. (1998). Topography of lobate scarps on Mercury: New constraints on the planet's contraction. *Geology*, **26** (11), 991–994, DOI: [10.1130/0091-7613\(1998\)026<0991:TOLSOM>2.3.CO;2](https://doi.org/10.1130/0091-7613(1998)026<0991:TOLSOM>2.3.CO;2).
- WATTERS, T. R., Schultz, R. A. & Robinson, M. S. (2000). Displacement-length relations of thrust faults associated with lobate scarps on Mercury and Mars: Comparison with terrestrial faults. *Geophysical research letters*, **27** (22), 3659–3662, DOI: [10.1029/2000GL011554](https://doi.org/10.1029/2000GL011554).
- WATTERS, T. R., Cook, A. C. & Robinson, M. S. (2001). Large-scale lobate scarps in the southern hemisphere of Mercury. *Planetary and Space Science*, **49** (14), 1523–1530, DOI: [10.1016/S0032-0633\(01\)00090-3](https://doi.org/10.1016/S0032-0633(01)00090-3).
- WATTERS, T. R., Schultz, R. A., Robinson, M. S. & Cook, A. C. (2002). The mechanical and thermal structure of Mercury's early lithosphere. *Geophysical Research Letters*, **29** (11), 37–1, DOI: [10.1029/2001GL014308](https://doi.org/10.1029/2001GL014308).
- WATTERS, T. R., Robinson, M. S., Bina, C. R. & Spudis, P. D. (2004). Thrust faults and the global contraction of Mercury. *Geophysical Research Letters*, **31** (4), L04701, DOI: [10.1029/2003GL019171](https://doi.org/10.1029/2003GL019171).
- WATTERS, T. R., Solomon, S. C., Robinson, M. S., Head, J. W., André, S. L., Hauck II, S. A. & Murchie, S. L. (2009). The tectonics of Mercury: The view after MESSENGER's first flyby. *Earth and Planetary Science Letters*, **285** (3), 283–296, DOI: [10.1016/j.epsl.2009.01.025](https://doi.org/10.1016/j.epsl.2009.01.025).
- WHITTEN, J. L., Head, J. W., Denevi, B. W. & Solomon, S. C. (2014). Intercrater plains on Mercury: Insights into unit definition, characterization, and origin from MESSENGER datasets. *Icarus*, **241**, 97–113, DOI: [10.1016/j.icarus.2014.06.013](https://doi.org/10.1016/j.icarus.2014.06.013).
- WICHMAN, R. W. & SCHULTZ, P. H. (1989). Sequence and mechanisms of deformation around the Hellas and Isidis impact basins on Mars. *Journal of Geophysical Research: Solid Earth (1978–2012)*, **94** (B12), 17333–17357, DOI: [10.1029/JB094iB12p17333](https://doi.org/10.1029/JB094iB12p17333).
- WILHELMS, D. E., (1976). Mercurian volcanism questioned. *Icarus*, **28** (4), 551–558, DOI: [10.1016/0019-1035\(76\)90128-7](https://doi.org/10.1016/0019-1035(76)90128-7).
- WILHELMS, D. E., McCauley, J. F. & Trask, N. J. (1987). The geologic history of the Moon. *US Geological Survey Professional Paper*, 1348, bibcode: [1987ghm.book.....W](https://ui.adsabs.org/1987ghm.book.....W).
- WOOD, C. A. (1979). Crater degradation through lunar history. In: *Lunar and Planetary Science Conference*, **10**, 1373–1375, bibcode: [1979LPL....10.1373W](https://ui.adsabs.org/1979LPL....10.1373W).
- WOOD, C. A. & ANDERSON, L. (1978). New morphometric data for fresh lunar craters. In: *Lunar and Planetary Science Conference*, **9**, 3669–3689, bibcode: [1978LPSC....9.3669W](https://ui.adsabs.org/1978LPSC....9.3669W).

- WOOD, C. A., Head, J. W. & Cintala, M. J. (1977). Crater degradation on Mercury and the moon-Clues to surface evolution. In: *Lunar and Planetary Science Conference*, **8**, 3503–3520, bibcode: [1977LPSC....8.3503W](#).
- XIAO, Z., Strom, R. G., Chapman, C. R., Head, J. W., Klimczak, C., Ostrach, L. R., Helbert, J. & D’Incecco, P. (2014). Comparisons of fresh complex impact craters on Mercury and the Moon: Implications for controlling factors in impact excavation processes. *Icarus*, **228**, 260–275, DOI: [10.1016/j.icarus.2013.10.002](#).
- ZUBER, M. T., Smith, D. E., Phillips, R. J., Solomon, S. C., Neumann, G. A., Hauck II, S. A., Peale, S. J., Barnouin, O. S., Head, J. W., Johnson, C. L., Lemoine, F. G., Mazarico, E., Sun, X., Torrence, M. H., Freed, A. M., Klimczak, C., Margot, J. –L., Oberst, J., Perry, M. E., McNutt Jr., R. L., Balcerski, J. A., Michel, N., Talpe, M. J. & Yang, D. (2012). Topography of the northern hemisphere of Mercury from MESSENGER laser altimetry. *Science*, **336** (6078), 217–220, DOI: [10.1126/science.1218805](#).

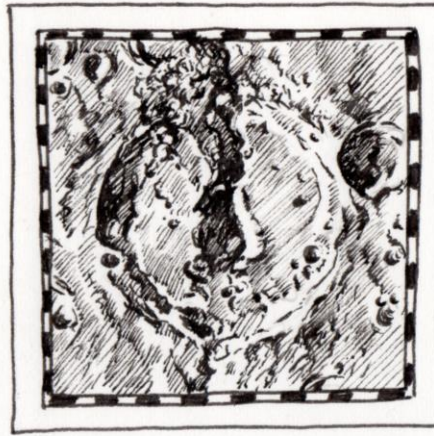
Acknowledgments

I am grateful to all the people that supported me during this research starting from my supervisors: Luigi Ferranti, who improved my knowledge in structural geology; Pasquale Palumbo, who introduced me to planetology and to the future ESA missions of BepiColombo and JUICE; Gaetano Di Achille, who introduced me to planetary geology. I wish to thank Matteo Massironi who provided an extra help in structural planetary geology and crater counting techniques. I am grateful to David A. Rothery who polished the English of the text and critically reviewed the thesis. I wish to thank my Open University friends and colleagues Rebecca J. Thomas, Emma Fegan (a.k.a. “The Mercury girls”), Susan J. Conway, Peter Fawdon and Matthew Balme and the other colleagues of DPS for sharing with me their knowledge and pleasant times. I am also grateful to my Italian geo-colleagues: Lorenza Giacomini, Cristian Carli, Valerio Vivaldi, Riccardo Pozzobon, Paolo Mancinelli, Laura Guzzetta, with whom I wish to continue our geological planetary research (possibly without the limits imposed by the Italian *precariato*). Many other people helped me during these years: Alessandra Rotundi, Vincenzo Della Corte, Roberto Sordini, Stavro Ivanovski, Mario Accolla, Michele Zusi, Ciprian Popa, Elena Mazzotta Epifani, Ernesto Zona. And I will never forget the early encouragement that Frans J. M. Rietmeijer gave me, before starting my PhD, during a brief, but intense period at the University of New Mexico, Albuquerque. *Dulcis in fundo*, I am very grateful to all my family that has always believed in me, Rita who drew a beautiful picture for the cover, and of course, Marco Ferrari, without whom I would have never began this exciting “journey to the stars”.

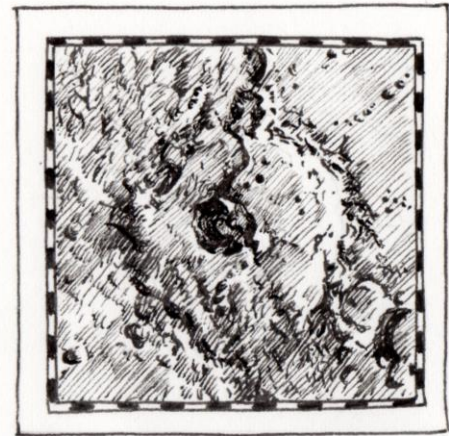
This research was supported by the Italian Space Agency (ASI) within the SIMBIOSYS project (ASI-INAF agreement no. I/022/10/0). I acknowledge the use of MESSENGER MDIS image mosaics processed by NASA/Johns Hopkins University Applied Physics Laboratory/Carnegie Institution of Washington. This research has made use of the USGS Integrated Software for Imagers and Spectrometers (ISIS). I thank Trent Hare and Kris Becker for the constant help provided in the USGS ISIS support forum.



50km



25km



50km

Artist impression of some faulted craters. From left to right: Duccio crater on Carnegie Rupes, Geddes crater on Antoniadi Dorsum and unnamed crater on Victoria Rupes. Ink on paper by Rita Petti.

